Dissertation
submitted to the

Combined Faculties for the Natural Sciences and for Mathematics
of the Ruperto-Carola University of Heidelberg, Germany

for the degree of
Doctor of Natural Sciences

Put forward by
Dipl.Phys. Jens Kühnle
born in Heidelberg/D

oral examination:
01.06.2011

Structure Formation and Self-Organization in the Early Secretory Pathway

Referees: Prof. Dr. Michael Hausmann
Prof. Dr. Matthias Weiß

Zusammenfassung

Im Rahmen dieser Dissertation werden diffusionsgetriebene Struktur und Selbstorganisationprozesse im frühen sekretorischen Pfad von biologischen Zellen untersucht. Dies umfasst Prozesse im Endoplasmatischen Retikulum (ER), dem Golgi Apparat (GA) und deren Transporteinheiten. Mesoskopische Simulationsmethoden werden angewandt um Phänomene auf unterschiedlichen Längenskalen zu untersuchen. Auf der Mikrometerskala werden Selbsorganisationeigenschaften des GA untersucht und dessen erstaunliche Eigenschaft sich nach vollständigem Abbau wieder zu regenerieren. Desweiteren besitzen unterschiedliche Organismen eine große Bandbreite an GA Phänotypen. Sowohl die dynamische Regeneration als auch die Diversität an Phänotypen können in einem einfachen Modell durch Unterschiede in der Fusions- und Transportmaschinerie erklärt werden. Auf der Nanometerskala wird die Bildung von Transportvesikeln durch COPI Hüllenproteine untersucht. Zuerst wird die von ARFGAP verursachte Ablösung der COPI Hülle untersucht. Insbesondere zeigt sich, dass eine krümmungsabhängige ARFGAP-induzierte Ablösung der COPI Hülle für die Vesikelbildung vorteilhaft sein könnte. Anschließend wird ein Reaktions-Diffusions Modell hergeleitet, das sich mit der Bildung von COPI Domänen beschäftigt. Im Wesentlichen können diese Domänen durch Lipid-Protein Wechselwirkungen entstehen, d.h. bestimmte Proteine bevorzugen spezielle Lipidumgebungen und verändern gleichzeitig ihr Lipidmilieu.

Abstract

In this thesis diffusion-driven structure formation and self-organization processes in the early secretory pathway of living cells are studied. In particular, this study is concerned with the endoplasmatic reticulum (ER), the Golgi apparatus (GA), and traffic intermediates in between. Mesoscopic simulation techniques are applied in order to study phenomena on different length scales. On the micron scale self-organization properties of the (GA) and its remarkable ability to rebuild after complete disassembly are investigated. Moreover, in different organisms a wide range of GA phenotypes can be found. On the basis of the presented model, the dynamical structure as well as various phenotypes can be explained as a result of changes in the fusion and transport machinery. On the nanometer level, formation of vesicles via COPI coat proteins is investigated. First, the dissociation process of the COPI coat induced by ARFGAP is studied. In particular, a curvature-sensitive detachment mechanism might be beneficial for vesicle formation. Second, a reaction-diffusion model is derived from existing biological data. It is shown how COPI domains can form efficiently via lipid-protein interactions, i.e. a preferential localization of proteins to specific lipid environments and a protein-mediated change of the lipid milieu.

Contents

Chapter 1

Introduction

Living organisms are organized into fundamental subunits on the micron scale, so-called cells. Biological cells can be considered as living matter as they are self-reproducing and self-sustained entities. They feature highly complex structures on many different length scales. But how does this complexity emerge? In modern cell biology it is still unclear how large cellular structures, such as organelles, are formed and maintained. Organelles are specialized enclosed subunits within a cell. What governs their shape and their size? Which are the responsible cues that localize them to specific places?

One solution to these questions is the formation of a structure due to inheritance, i.e. via copying a template structure. Since the discovery of the deoxyribonucleic acid (DNA) replication mechanism, templated inheritance has become a widespread concept in cell biology. A drawback of this approach is that it does not explain the origin of the template itself. A second powerful concept that is less commonly considered in biology is self-organization. In this case, global patterns arise from local and dynamic interactions of individual elements. The emerging properties of the whole system are neither the product of a central authority (a "mastermind"), nor can they be predicted by the individual properties of its elements.

Does this emergence of order contradict the second law of thermodynamics? Not necessarily, because many thermodynamic systems, e.g. biological cells, can acquire energy from their environment, and they employ it to decrease their entropy. Hence, they are open systems out of equilibrium. This can be illustrated for instance in lithotrophic organisms such as bacteria or algea that harvest sunlight. Due to ongoing chemical reactions they produce heat and thus emit light in the infrared spectrum. By absorbing fewer photons of higher energy and emitting more photons of lower energy they increase the entropy of their surrounding. This enables them to create highly ordered molecular structures from the gain in free energy.

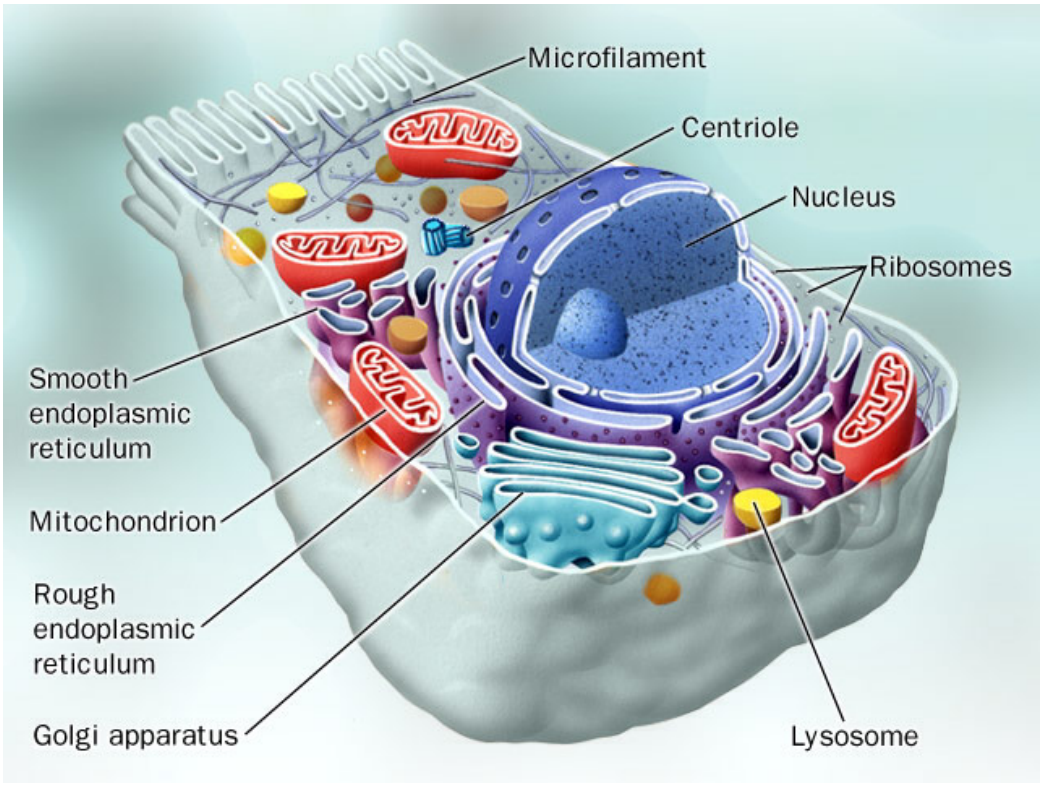

Figure 1.1: *Schematic of a typical eukaryotic cell. The plasma membrane separates the cellular interior from the environment. Internal membranes separate cellular subunits so-called organelles that exert specific functions. The nucleus stores genetic information in form of DNA while mitochondria are responsible for energy conversion. Other important organelles are endoplasmic reticulum and Golgi apparatus which are both involved in cellular transport. Image courtesy of chemistrypictures.org.*

Before discussing self-organization processes in biological cells, let us briefly look at the cellular architecture (cf. Fig. 1). Cells store their genetic information in form of the deoxyribonucleic acid (DNA) in their interior. Depending on whether the DNA is stored in a separate compartment or not, cells are either termed *eukaryotes* or *prokaryotes*, respectively. This separate compartment is termed *nucleus*. Bacteria are for instance prokaryotes, while cells of more complex organisms such as animal or plant cells and fungi belong to the class of eukaryotes. A typical eukaryotic cell is roughly $10 - 100\,\mu$m in size. In order to retain its own distinct chemical environment, each cell is enclosed by a shell-like structure – the plasma membrane.

Structural integrity and mechanical stability within eukaryotic cells is provided by a system of interconnected filaments called the *cytoskeleton*. Many other processes rely as well on the cystoskeleton. During cell division for instance, the cytoskeleton pulls the chromosomes apart [Alberts08]. In addition, by dynamically assembling parts of the cytoskeleton at the front and disassembling at the same time at the back, cells can move in a directed manner. Moreover, similar to train tracks, effective intracellular transport is achieved via molecular motors that walk along these filaments. In between the cytoskeleton the cell is filled with a viscoelastic medium [Guigas07], the *cytoplasm*. The part of the cytoplasm that is not occupied by additional membrane-bound compartments is called *cytosol*. It is a dense fluid consisting mainly of water, salts and organic molecules. Besides the nucleus, eukaryotic cells typically feature several more organelles, i.e. specialized cellular subunits that are enveloped by a lipid bilayer to exert specific functions. Important organelles are, for instance, *mitochondria*, which are mainly responsible for the cell's power supply, by producing adenosine triphosphate (ATP). ATP is the main source of cellular chemical energy and it is required for a wide range of different cellular reactions and processes. ATP is synthesized in an energetically unfavorable chemical reaction: a phosphate group is added to ADP (adenosine diphosphate) by the ATP synthase which is powered by a proton gradient across the mitochondrial membrane. In order to drive certain chemical reactions or to power molecular motors and pumps, energy can be obtained by converting ATP back to ADP. Guanosine triphosphate (GTP) is closely related to ATP and it represents another major source of energy. Similar to ATP, energy is released via hydrolysis of GTP to GDP (Guanosine diphosphate).

The *secretory pathway* is a major transport route within the cell and involves several transport steps from the synthesis of a protein to its secretion into the extracellular space. The starting point is the endoplasmic reticulum (ER) in which most proteins and lipids are synthesized. It consists of an extensive membrane network that is directly connected to the nuclear envelope, and it extends throughout the whole cell. From the ER, proteins are shipped towards the Golgi apparatus (GA). Lipids and proteins, such as proteoglycans, are processed here

in a series of modification steps. Ultimately, proteins will be delivered from the GA to their final destination, e.g. the plasma membrane in the case of secretory proteins, by means of membrane carriers [Hirschberg98].
In contrast to the aforementioned long-range transport via the cytoskeleton, many structure formation processes do not rely on directed transport, but are rather driven by diffusion. In his pioneering work, Turing predicted, when diffusion can support the formation of spatial patterns rather than establishing a homogeneous steady state [Turing52]. Since then, it has become more and more evident that many systems seem to rely on similar self-organization processes. Prominent examples are the formation of microtubular asters [Nédélec97] and their interaction [Nedelec02]. Another example is the division process of the rodshaped bacterium *Escherichia coli*. The bacterium needs to determine its middle and the time point for cleavage. Again, this system may be described via reaction-diffusion mechanisms [Howard01; Meinhardt01; Kruse02; Howard03].
Although biological membranes are not self-organized systems in a strict sense, they can be viewed as another important example of intracellular structure formation. Membranes consist mainly of small amphiphilic molecules called lipids. When dissolved in water, they try to shield their hydrophobic core while exposing their hydrophilic heads to water at the same time. This results typically in a bilayer structure. Moreover, depending on lipid geometry, type and mixture a multitude of different lipid structures and phases can emerge [Mouritsen04]. Since cellular organelles are constantly exchanging material with each other, they tend to equilibrate their composition. Again, a basic set of interacting molecular players seem to be sufficient that cellular compartments are able to retain their chemical identity in a self-organized manner [Heinrich05].
Microscopy has been an invaluable tool in shedding light on the fascinating intracellular structures and their functions. Unfortunately, a lot of remaining questions cannot be addressed by light microscopy, because even advanced methods like STED (stimulated emission depletion [Hell94]) are not capable of resolving structures that are smaller than roughly 40 nm. In contrast to that, electron microscopy allows for imaging on the nanometer scale, but it lacks any information about the dynamics of processes. Thus, computer simulations are a versatile tool to study dynamic processes in cells on different length scales. In this study, especially mesoscopic computer simulations, i.e. simulations on a coarse-grained level, have been employed to investigate structure formation processes. The advantage of mesoscopic simulations is that larger length and time scales become accessible by neglecting atomistic details on smaller length scales.
In the first part of this thesis some important general background information will be provided.
Initially, additional background information about lipid membranes will be provided in chapter 2. In chapter 3, we will look in more detail at the organelles

of the early secretory pathway, i.e. the Golgi apparatus and the ER. Moreover, different important means of transportation within and between these organelles will be discussed. After that, a more general introduction about diffusion and the formation of Turing patterns will be given in chapter 4.
In the second part of this thesis, structure formation processes within the secretory pathway will be investigated. In particular, the focus will shift from processes on the micron scale down to the nano scale.
On the largest length scale we will be concerned with self-organization properties of the Golgi apparatus (cf. chapter 5). From experiments a variety of different Golgi phenotypes are known. Moreover, it has been found that the GA shows a highly dynamic behavior as the GA rebuilds after complete disassembly e.g. after mitosis or after application and wash-out of the drug Brefeldin A [Sciaky97]. So far no coherent picture of all these phenotypes has been drawn. Here, a coarse-grained computational model is formulated that captures experimentally observed Golgi phenotypes as well as the dynamic morphogenesis of a Golgi apparatus. In particular, the model relates the experimentally observed Golgi phenotypes, the typical turnover times, and the size and number of cisternae to three basic, experimentally accessible quantities: the rates of material influx from the endoplasmic reticulum, and the anterograde and retrograde transport rates. Based on these results, molecular factors that alter phenotypes and dynamics are proposed.
In chapter 6 the focus shifts towards a smaller scale within the GA. Vesicle formation at the Golgi apparatus is driven by the COPI vesicle machinery. The large coatomer complex can bind to membranes and induces membrane curvature. Subsequent aggregation of coatomer leads to bud/vesicle formation. ARFGAP also binds to Golgi membranes and triggers the dissociation of coatomer from the membrane. Recently, it was observed that the stimulating effect of ARFGAP depends on the local curvature of the membrane [Bigay03]. A curvature-sensitive mechanism could be benefitial, because vesicles could easily shed their coats, an event that is required for fusion with the target compartment [Spang09]. However, it remained unclear, whether a coupling of coat dissociation to high values of curvature obstructs the formation of buds/vesicles. Here, a simple model is fomulated to probe the generic hypothesis that curvature-stimulated dissociation of coat molecules hinders the formation of vesicles. By using parameters for this one-dimensional model that are consistent with those that have been measured for the COPI machinery, indication is found that a curvature-sensitive detachment mechanism could even improve vesicle formation.
After focussing on the process of COPI disassembly we will concentrate on the formation of coatomer-covered patches in chapter 7. Few basic components of the COPI machinery, i.e. the proteins ARF-1, ARFGAP, and coatomer, seem to be sufficient to drive vesicle formation. However, in the last decades, the

importance of lipids in biological processes has become clear and lead to the emerging age of lipidomics [Mouritsen04]. Along these lines, it has become evident that lipids have to be incorporated into the existing framework of COPI coat formation [Roth99]. Although the basic components seem to be enough to generate a COPI vesicle, the full machinery is required in biological cells in order to regulate the efficiency [Roth99]. We develop here a simplified mathematical model on this biological basis. The concentrations of ARF1 and ARFGAP are simulated in a reaction-diffusion model. It is directly connected to the process of vesicle formation since ARF1 binds the large curvature-inducing coatomer complex to the membrane. The influence of several lipid species such as phosphatic acid (PA), diacylglycerol (DAG) and phosphatidylinositol 4,5-bisphosphate (PIP2) is considered implicitely, resulting in positive/negative feedback loops for ARF1 and ARFGAP concentrations. It is shown, that self-organized formation of spatial patterns are a generic phenomenon of this reaction-diffusion model. This means, vesicular carriers can be produced efficiently within these spatial domains. Moreover, the influence of subdiffusion, i.e. an increase of the mean squared displacement $\langle x^2 \rangle \propto t^\alpha$, $\alpha < 1$, is analyzed and it is shown that subdiffusion can be benefitial for structure formation.
Lipids are not only the building blocks of the above mentioned phenomena but also many of their properties such as diffusion or mechanical/geometrical characteristics affect structure formation processes. To gain a better understanding of lipid properties that can affect structure formation, single lipids are modeled on the nanometer scale with a simulation technique called dissipative particle dynamics (DPD) in chapter 8. As part of a larger study that is concerned with curvature-modulated sorting of lipids, the dependence of the membrane's bending stiffness on the concentration of rigid and floppy lipids is studied. The exact nature of this relation affects not only dynamics but also the equilibrium state of pattern formation. Lipid diffusion is another decisive factor for structure formation. Lipid diffusion in heterogeneous environments has been shown to be subdiffusive [Ratto03]. However, previous work on homogeneous artificial membranes reported normal lipid diffusion. A recent study [Harland10] suggested lipid subdiffusion within homogeneous artificial membranes challenging existing data. Here, their hypothesis is tested by means of DPD. In particular, we aim at reaching experimental accessible timescales. As a result, we report normal diffusion within the time scales of the simulation. This can be taken as indication that, for example, the interactions of the large fluorescent probe with the surrounding fluid can give rise to the measured subdiffusive behavior [Harland10].

Part I

Prerequisites

Chapter 2

Lipids and membranes

2.1 Structure of biological membranes

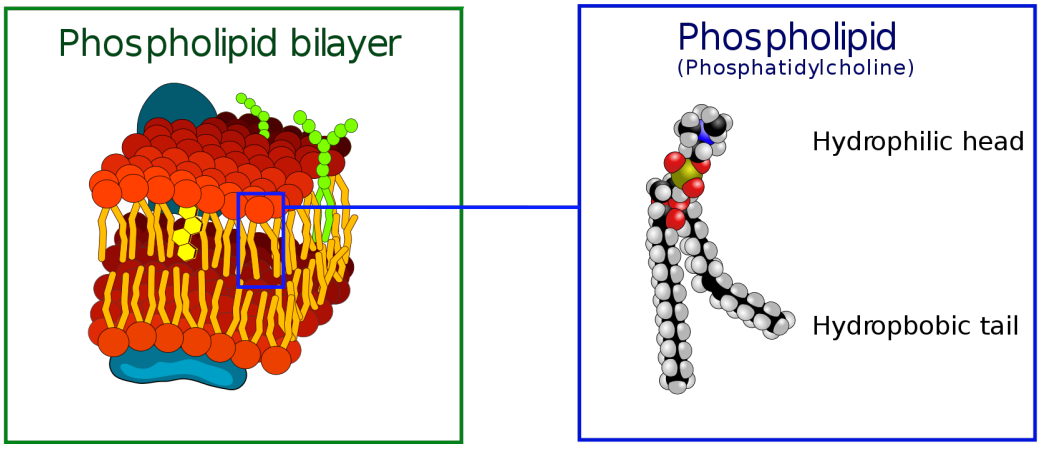

Figure 2.1: *Lipids are amphiphilic structures, i.e. they possess a polar part that is highly attracted to water, and a non-polar part that is repelled by water. Due to their unique structure, lipids can assemble into two-dimensional sheet-like structures with two opposing layers. In this arrangement lipids expose their hydrophilic heads to water while shielding their hydrophobic tails from it. (Image acquired from www.wikipedia.org as part of the public domain)*

Cellular membranes are highly abundant structures in eukaryotic cells and they are responsible for a variety of different tasks. The *plasma membrane* makes up the boundary of the cell and keeps the components of the cell together. Internal membranes enclose cellular organelles such as the endoplasmatic reticulum, the Golgi apparatus, and the mitochondria. Membranes provide specific chemical

environments to facilitate distinct chemical reactions. Different kinds of reactions, such as the synthesis of ATP, are also driven by concentration gradients across these membranes. Other membrane structures, e.g. vesicles, are involved in transport processes within the cell.

All of those cellular membranes possess a common architecture: Membranes are composed of amphiphilic molecules such as lipids and proteins which form a sheet-like structure with two opposing layers ('leaflets'). Due to their amphiphilic nature, these molecules try to expose their hydrophilic headgroups to the surrounding water while shielding at the same time their hydrophobic tails. This leads to various supramolecular assemblies such as lipid bilayers. This is shown in detail in Fig. 2.1 together with the chemical structure of one of the most abundant lipids - phosphatidylcholine.

Basically, hydrophobicity originates from entropic forces. Hydrophobic molecules disrupt the hydrogen-bond network of the surrounding water. Thus, the surrounding water molecules form a cage-like structure around this hydrophobic molecule with restricted degrees of freedom. Entropy can now be maximized if less hydrophobic surface area is exposed because less water molecules are confined to a specific orientation. This leads to clustering of the hydrophobic molecules ('oil drop in water') or special geometric arrangements such as lipid bilayers.

Essentially, lipid bilayers can be regarded as dynamic two-dimensional fluids, which allow for free motion within their plane with typical lipid diffusion coefficients of $D \approx 4\mu m^2/s$ [Korlach99]. Lipid bilayers are roughly 3-5 nm thick, and they serve as relatively impermeable barriers to most water-soluble molecules. Cellular membranes are crowded with all kinds of proteins. Some of those act as a point of anchorage to the cytoskeleton while other proteins, such as channels or pumps, are involved in selective transport across this barrier. Although being fluid, cellular membranes are highly heterogeneous structures [Engelman05]. Partly this heterogeneity arises from a high area occupancy of proteins and partly it stems from the huge variety of different lipids such as phospholipids, sphingolipids and sterols (e.g. cholesterol) that are incorporated within membranes. According to recent findings, different lipid species are likely to form microdomains on multiple length scales, which are also denoted as 'rafts' [Simons97]. Differences in membrane thickness might lead to preferential localization of proteins to specific domains. In addition, protein area occupancies as high as 50% [Alberts08] contribute to the highly heterogeneous ('mosaic') character of biomembranes (cf. Fig. 2.2).

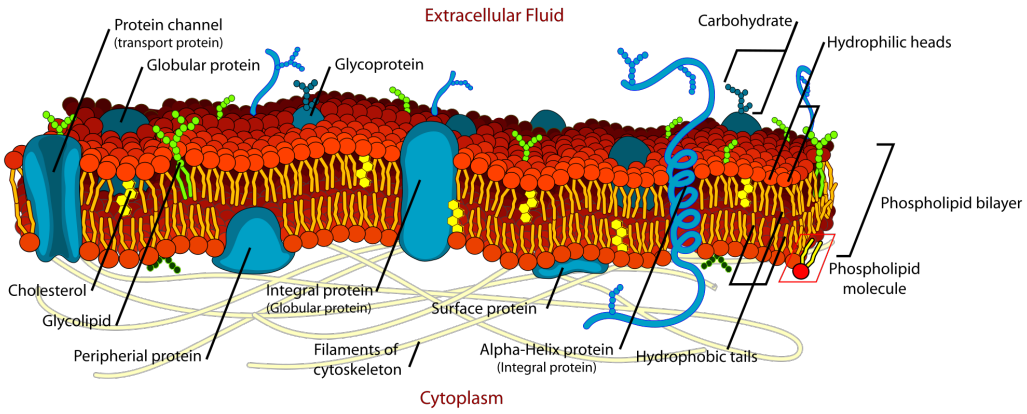

Figure 2.2: *Biomembranes are highly complex and heterogeneous structures. Partly this heterogeneity arises from a high area occupancy of proteins and partly it stems from the huge variety of different lipids that are incorporated within membranes. Some proteins attach cellular membranes to the cytoskeleton whereas other proteins tend to aggregate within microdomains of varying membrane thickness. (Image acquired from www.wikipedia.org as part of the public domain)*

2.2 Mathematical descriptions of membranes

If we neglect molecular details of membranes and zoom out, lipid membranes can be described as (infinitesimally) thin elastic sheets. The surface can be parameterized by a function $\mathbf{S}(\mathbf{r})$ in three-dimensional space.
In the Monge representation, $\mathbf{S}(\mathbf{r})$ is decribed in Cartesian coordinates and approximated as 'almost planar' surface that does not feature any kinds of 'overhanging' structures. Mathematically, $\mathbf{S}(\mathbf{r})$ is then represented by mapping each point of the x-y plane in a unique manner onto a heightfield $h(x, y)$:

$$\mathbf{S}(\mathbf{r}) = \begin{pmatrix} x \\ y \\ h(x,y) \end{pmatrix} \tag{2.1}$$

Each point within this surface can be locaclly described by its two radii of curvature R_1, R_2. From these radii, the mean curvature

$$H \equiv \frac{1}{2}\left(1/R_1 + 1/R_2\right) \tag{2.2}$$

as well as the Gaussian curvature

$$K \equiv 1/\left(R_1 R_2\right) \tag{2.3}$$

can be derived. Under the assumption of small curvatures (Monge gauge) the mean curvature can be expanded as:

$$H \approx \frac{1}{2}\Delta h(x, y) \tag{2.4}$$

The bending energy associated with a membrane configuration can be expanded in powers of the curvature giving rise to the Helfrich Hamiltonian [Helfrich73]

$$F_H = \int_A d^2x \left[\frac{\kappa}{2}(2H - C_0)^2 + \kappa_G K + \sigma\right] \tag{2.5}$$

Here, σ denotes a tension applied to the membrane and κ is the bending stiffness, whereas κ_G represents the Gaussian curvature modulus. The preferred curvature C_0 takes into account that the membrane could adopt non-zero curvatures in equilibrium. In the biological case, a preferred curvature may arise due to membrane-associated proteins that induce a conical perturbation in the bilayer. For simplicity, we assume in the following derivation $C_0 = 0$.
We will derive now the fluctuation spectrum of a flat membrane as described in [Seifert97]. Since the Gaussian curvature does not change for a given topology (as can be deduced from the Gauss-Bonnet theorem), it does not need to be considered here.
The Fourier transformation of

$$h(x, y) = \int \frac{d^2q}{(2\pi)^2} h(\mathbf{q}) \exp(i\mathbf{qx}) \tag{2.6}$$

in Eq. 2.5 allows for the evaluation of the Laplacian, yielding powers of the wave vector q:

$$F_H = A \int \frac{d^2q}{(2\pi)^2} \left[\sigma q^2 + \frac{\kappa}{2} q^4\right] h(\mathbf{q}) h^*(\mathbf{q}) \tag{2.7}$$

where * denotes the complex conjugate and A the surfaces area projected onto the x-y plane. When considering the equipartition theorem (each fluctuation mode carries an energy equivalent to $k_B T/2$), an expression of the membrane's fluctuation spectrum can be obtained for the thermodynamic equilibrium:

$$\langle |h_{\mathbf{q}}^2| \rangle = \frac{k_B T}{A\left(\kappa q^4 + \sigma q^2\right)} \tag{2.8}$$

This means that free membranes with zero surface tension ($\sigma = 0$) are expected to exhibit a characteristic fluctuation spectrum that decays with $1/q^4$. Moreover, this relation provides a means for an experimental determination of the membrane's bending stiffness κ.

2.3 Lipid structure formation

Depending on lipid geometry not only bilayers but also various other structures can self-assemble from lipids.
Here, the so-called shape factor $a \equiv \nu/(l_c a_0)$ decisively determines the large-scale structure of the lipid assembly with ν being the volume occupied by the hydrocarbon chain(s), the optimal headgroup area a_0, and the critical chain length l_c , respectively. In case of $a < 1$, i.e. the headgroup is larger than the lipid tail, typically micelles are formed. These are either cylindrical or spherical structures with lipid heads facing outwards and the hydrophobic tails pointing radially towards the center. The case $a > 1$ can either lead to inverted micelles or the inverted hexagonal phase – a sponge-like arrangement with water trapped inside a continous lipid phase. 'Cylindrical' lipids for which $a = 1$, give rise to lipid bilayers: two opposing monolayers sandwich their hydrophobic tails between two sheets of headgroups [Richter04].
Let us now look in more detail at the intrinsic structure of a lipid bilayer and the structure formation processes taking place inside. Different thermodynamic phases of lipid bilayers exist. Most prominent are the gel phase L_β and the liquid cristalline phase L_α (also termed fluid phase). In the gel phase L_β, lipids are in an ordered quasi-cristalline arrangement in contrast to the fluid phase L_α with highly entangled hydrocarbon chains. This affects also lipid mobility: lipid diffusion coefficents of the fluid phase ($\mathcal{O}(\mu\mathrm{m}^2/s)$) drop roughly two orders of magnitude upon transition to the gel phase.
The phase transition temperature T_{crit} depends critically on lipid type. In particular, it is affected by lipid length and the amount of double bonds within the lipid's hydrocarbon chain. When mixing lipids with differing phase transition temperatures, they can undergo phase separation [Veatch05]. Especially cholesterol plays a crucial role in phase separation processes in biological membranes. It increases the packing densitiy within the membrane while preventing at the same time a transition towards the gel phase. In addition, cholesterol seems to influence the membrane thickness [vanMeer02].
Other physical properties that affect phase separation behavior are the lipids' bending stiffness κ_{lipid} and their corresponding spontaneous curvature C_0. This can be observed for instance in lipid bilayers that are subject to geometrical constraints such as external curvature, e.g. mediated by curved proteins attaching to the membrane surface. Moreover, it is thought that lipid mixtures composed of stiffer and softer lipids prefer regions of lower/higher curvature, respectively [Yoon06; Mercker11]. Segregation of intrinsically curved lipids (i.e. $a \neq 1$) into regions of high curvature is another mechanism for domain formation on biological membranes [Huang06]. This sorting process can be further enhanced by the addition of proteins [Sorre09].

In general, mutual interactions of lipids and proteins are highly important for membrane organization and function (see [Jensen04] for an overview). Not only do lipids influence the function of certain proteins, but via mutual interaction lipids and proteins can trigger a segregation process. One such interaction is *hydrophobic mismatching*: If the hydrophobic core of a protein does not fit perfectly into the membrane, a thickness perturbation can emerge. Surrounding lipids try to adapt to it. Therefore, they are confined to a specific configuration with a lower entropy as compared to the unperturbed case. In order to minimize the perturbed area, proteins tend to cluster [Schmidt08] or segregate into specific lipid environments. Moreover, in chapter 7 the possibility of segregating lipids and proteins via reaction-diffusion mechanisms will be elucidated. Overall, it can be said that biomembranes give rise to a large number of fascinating structure formation and self-organization phenomena, which in turn are crucial to cellular function.

Chapter 3

The early secretory pathway

The secretory pathway is a major transport route within the cell. Due to the ongoing transport processes, structures within the secretory pathway have to be highly dynamic in order to adapt to changes e.g. during the cellular lifecycle or due to external stimuli. These requirements suggest that processes within the secretory pathway are regulated in a self-organized manner.
Before turning in detail to the individual transport steps of the secretory pathway, let us look at the pathway as a whole. This transport route starts in the ER where most membrane proteins are synthesized. From the ER, transport is mediated by membrane carriers towards the GA. Subsequently, cargo traverses the Golgi stack. From late Golgi elements, cargo is shipped via membrane vessels towards their final destination, e.g. the plasma membrane.

3.1 The endoplasmatic reticulum

The ER can be viewed as the starting point of the secretory pathway, because it is the central site for protein and lipid synthesis. Moreover, the ER is also crucial for the regulation of cellular calcium levels. This organelle is made up by interconnected membrane tubules and disk-like structures. Although the extensive ER network stretches throughout the whole cell, it possesses a single continuous internal space - the so-called ER lumen. It occupies roughly 10% of the whole cellular volume [Alberts08].
The ER consists of two functionally different parts, the rough and the smooth ER. In the rough ER specific protein complexes, called ribosomes, are attached to the membrane. Ribosomes manufacture proteins and the close neighborhood to the ER ensures a co- or posttranslational translocation of proteins into the ER that is an insertion parallel or subsequent to protein synthesis. In contrast, the smooth ER lacks ribosomes.

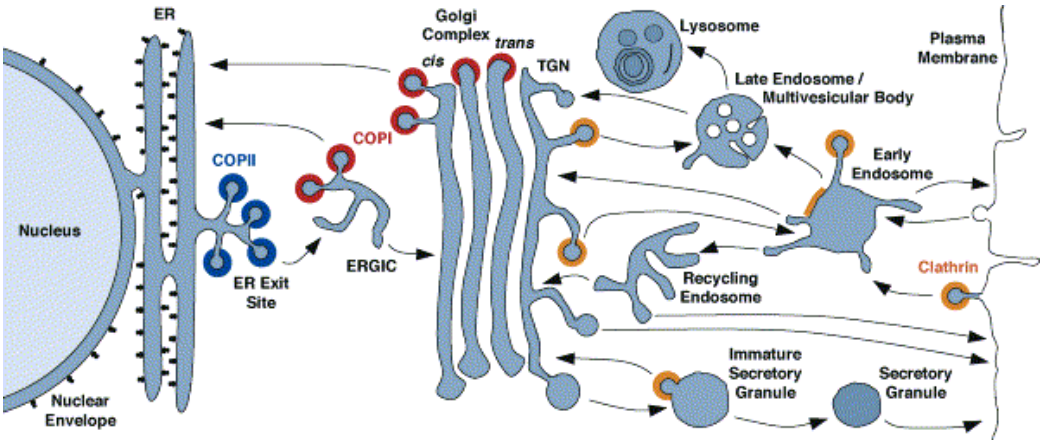

Figure 3.1: *Overview of the secretory pathway - a major intracelluar transport route. Intracellular transport steps are depicted by arrows and involved vesicle coats are color-coded: COPII (blue), COPI (red), and clathrin (orange). This transport route starts in the ER where most membrane proteins are synthesized. From the ER, proteins are shipped in a COPII dependend manner towards the GA. Subsequently, cargo traverses the Golgi stack. From late Golgi elements, cargo is shipped via membrane vessels towards the plasma membrane. Image reprinted with permission from [Bonifacino04].*

ER exit sites

However, the smooth ER features *ER exit sites* (ERES). These are specific sites from which transport vesicles/intermediates carrying newly synthesized proteins and lipids bud off. These transport intermediates then ship their cargo towards the GA [Gurkan06].

Typically, the size of such an exit site is roughly $0.5\mu m$ [Budnik09] and about 100 of these domains are scattered over the ER surface. In addition, a mechanism is required to ensure selective transport of proteins. It has been suggested that concentration of protein cargo could be provided by the interaction with the COPII coat [Tabata09]. Moreover, it has been found that ERES are dynamic entities that are diffusing [Heinzer08] and capable to fuse with each other while at the same time retaining a characteristic size [Bevis02]. In particular, the cell's cargo load seems to affect ERES size regulation in the sense that large amounts of cargo lead as well to larger ERES [Heinzer08; Farhan08]. Furthermore, it has been found that GA position correlates with ERES location [Budnik09]. Since ERES are directly connected to cellular transport, these findings suggest that GA position is determined by transport properties. Along these lines, Golgi structures associated to ERES are affected by the ERES fusion process and undergo

fusion themselves [Bevis02]. In contrast, dispersal of the Golgi during mitosis is accompanied by a loss of Sec13 from ERES [Hammond00].

3.2 Membrane carriers in the early secretory pathway

3.2.1 COPII vesicles

COPII protein complexes are involved in the formation of membrane transport carriers in the ER. More specifically, COPII coats are $10\mathrm{nm}$-sized [Matsuoka01] protein complexes that seem to cluster in ERES. Subsequently, they form a mesh that bends the ER membrane and induces curvature. Ultimately, that leads to the pinch-off of so-called COPII-coated vesicles with a diameter of approximately $60\,\mathrm{nm}$. After pinch-off, these COPII vesicles uncoat. Via fusion they form larger membrane transport vessels, so-called vesicular-tubular clusters (VTCs) [Xu04].
Different steps are involved in the assembly of a COPII protein complex. A protein called Sec12 acts as a guanine exchange factor for the small GTPase Sar1. Upon nucleotide exchange, Sar1 firmly attaches to the membrane by inserting a hydrophobic extension into the membrane [Bonifacino04]. Sar1 acts similar to a switch: when binding to GTP it is active while it is inactive after GTP has been hydrolyzed to GDP. First, Sec23/Sec24 is recruited by the active Sar1. Then, the Sec13/Sec31 subcomplex polymerizes onto Sec23/Sec24, hence crosslinking the pre-budding complexes. Together, Sar1, Sec13/Sec31 and Sec23/Sec24 form the COPII coat.
Paradoxically, Sec23/Sec24 stimulates the hydrolysis of Sar1-GTP to Sar1-GDP. That means, the COPII coat is intrinsically unstable, since hydrolysis of Sar1 leads to the disassembly of the COPII coat [Antonny01]. Moverover, specific binding domains have been found in Sec24 that could provide the selection of cargo proteins [Miller03]. PIP2 and phosphatic acid also have been implicated in the recruitment of Sec23/24, and they could support coat binding and cargo recognition [Aridor02].
Even though the exact role of Sec16 is not entirely clear, this protein is part of ERES and has been implicated in the stabilization and the large scale organization of the COPII coat [Hughes09].

3.2.2 COPI vesicles

Although the molecular players are different, the COPI complex mediates vesicle budding in similar ways to the COPII coat. Again, the membrane is bent by a polymerizing network of coat complexes to form 60 *nm* sized vesicles [Spang98].

However, COPI is involved at a later stage of cellular transport. COPI vesicles are not only an important tool for transport within the GA and retrograde from the GA towards the ER, but seem to be also active in VTCs [Stephens00].

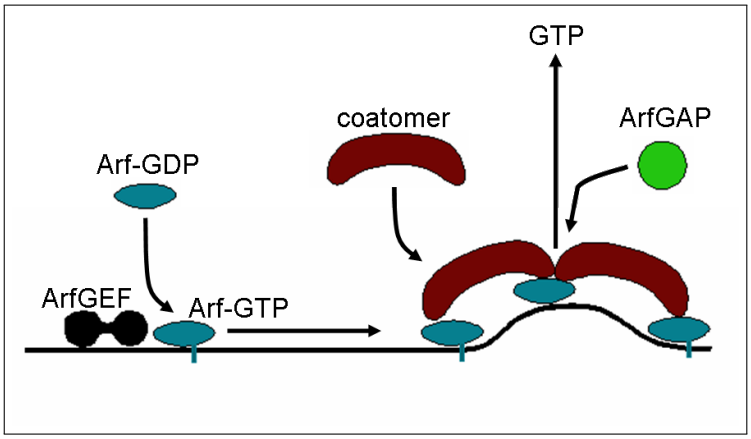

Figure 3.2: *Formation of the COPI coat. ArfGEF recruits cytosolic Arf to the membrane by exchanging GTP for GDP. Membrane-bound Arf-GTP recruits the large coatomer protein complex. Arf1 and coatomer drive together membrane curvature. ArfGAP stimulates GTP hydrolysis by Arf1, which in turn initiates the disassembly of the COPI complex.*

Assembly of the COPI coat is initiated by ArfGEF, a protein that exchanges GTP for GDP in the protein Arf1 (cf. 3.2). As a result of this process, Arf1 becomes firmly attached to membranes. Then, membrane-bound Arf1 is able to recruit the large coatomer complex that in turn drives membrane curvature. Upon GTP hydrolysis, Arf1 detaches from the membrane, and it is released back into the cytoplasm. The hydrolysis itself has been shown to be stimulated by the Arf GTPase-activating protein (ArfGAP)[Lee04]. Moreover, Arf1 hydrolysis destablizes the coat and leads to its detachment. Recently, it was observed that the hydrolysis-stimulating effect of ArfGAP depends on the local curvature of the membrane [Bigay03]. This mechanism would allow for a rapid shedding of the coat after vesicle production. In contrast, a curvature-sensitive coat detachment could hinder the production of vesicles in the first place.

As shown by in vitro experiments, Arf1-GTP and coatomer seem to be the main COPI components, and they represent the minimum machinery to form a COPI-coated vesicle [Spang98]. Despite these findings, lipids seem to play a role in COPI assembly as well. A recent study found that the COPI coat localizes to lipid membranes in a liquid disordered state, suggesting that COPI induces lipid sorting [Manneville08]. Moreover, it has been found that Arf1

binds preferentially to PIP2 and also interacts with PA and DAG [Roth99]. Lipid domains are thought to be involved in cargo selection of membrane proteins: Depending on the length of hydrophobic transmembrane core, proteins are thought to partition into lipid phases that match best this geometrical constraint [Schmidt10]. Soluble cargo that exhibit a specific sequence of amino acids, denoted as KDEL, can be captured by the KDEL receptor and shuttled back to the ER by COPI vesicles [Aridor02]. A well characterized retrieval signal for transmembrane proteins of the early secretory pathway is the cytoplasmic K(X)KXX-motif [Nilsson89; Jackson90; Cosson94]. The Arf1/coatomer complex is able to capture proteins by binding directly to this motif. Together with these recoginition mechanisms, cargo selection could be enhanced by Arf1 hydrolysis in terms of a kinetic proofreading mechanism [Weiss03c].

3.2.3 Vesicular tubular clusters (VTCs)

VTCs, also referred to as the ER-Golgi Intermediate Compartment (ERGIC), are large pleiomorphic membrane carriers that mediate transport towards the GA. These structures originate from fusion of COPII vesicles followed by a series of further homotypic fusion events [Xu04]. In addition, it has been shown that the SNARE syntaxin 5 is required for these fusion events [Xu04]. Alternatively, a scission event in the ER might also directly create these large transport carriers [Palmer04].
Subsequent transport of these entities from the ER to the Golgi apparatus is mediated by molecular motors such as dynein/dynactin that pull VTCs along microtubules [Murshid04]. En route towards the GA, retrograde cargo segregates within VTCs into COPI-coated structures [Stephens00]. In that respect VTCs change their composition ('mature') as components are retrieved to recycle back to the ER. Conversely, maturation could lead to VTC size regulation by exporting important factors of the fusion machinery such as syntaxin 5.

3.2.4 SNAREs and Tethers

COP vesicles as well as VTCs have to recognise and fuse with their target compartment. This is accomplished in a two step procedure by tethering complexes [Sztul09] and specialized triples of SNARE proteins [Parlati02].
The tethering step requires the presence of a small GTPase of the RAB family and either large heteromeric complexes like TRAPPI at the Golgi or the DSL complex at the ER, or long coiled-coil proteins such as p115 [Spang09] that is present in cis Golgi cisternae and VTCs. The long coiled-coil proteins are thought to act as 'tentacles' that grab vesicles with a particular Rab protein. Not only do these tethers mediate long-range attraction within up to 300 *nm*, but they also provide

an initial level of recognition to select the right acceptor compartment. In addition, some tethers such as GRASP65/55 and/or GM130 are required for stacking of different Golgi cisternae [Barr97; Shorter99; Linstedt99]. In this case, tethers provide only mechanical stability of the stack without leading to a subsequent fusion event. In essence, both processes can be regarded as the formation of temporary bonds between different membrane compartments. Therefore, in the simulations presented in Chapter 5 no destinction will be made between tethering that does or does not lead to the fusion of membrane compartments.
In order to trigger the fusion of membranes, close range ($< 12\,\mathrm{nm}$) recognition via SNARE proteins is required [Sztul09]. Specifically, it has been shown, that different SNAREs localize to different intracellular compartments. This observation suggests that a target compartment can be distinguished via its SNARE composition [Bennett93; Chen01]. Commonly, SNAREs are subdivided into two classes, v-SNAREs that are incorporated into transport vesicle, and t-SNARES that are located in the target compartment.
Structural and biochemical studies showed that the SNARE complex generated by the pairing of a cognate v- and t-SNARE is a very stable four-helix bundle. One α-helix is supplied by the monomeric v-SNARE, whereas the other three α-helices originate from the oligomeric t-SNARE [Bonifacino04]. Progressive zippering of this four-helical bundle of SNARE proteins forces the two lipid membranes into close opposition, destabilizes their surfaces, and causes the membranes to fuse.
After SNARE complex formation, the individual SNARE molecules are recycled in an energy consuming process. More precisely, α-SNAP binds along the edge of the SNARE complex and recruits NSF. NSF unravels the four-helices by applying rotational forces to the complex and thus dissociates the SNARE complex while consuming ATP.

3.3 The Golgi apparatus and its morphology

The Golgi apparatus (GA), the major hub for protein sorting and lipid metabolism in the secretory pathway [Alberts08], is a highly dynamic organelle. In interphase, the GA typically assumes the form of a stack of chemically distinct, flattened membrane discs, referred to as *cisternae*. The face of the GA receiving proteins from the ER is referred to as *cis*, whereas the middle and late part of the GA are called *medial* and *trans* cisternae, respectively.
In typical mammalian cells lateral connections between cisternae lead to the formation of a large juxtanuclear Golgi 'ribbon' [Lowe98]. Before mitosis, the Golgi stack/ribbon disintegrates at least in part, and it re-assembles with a remarkable precision after cytokinesis [Lowe98; Zaal99].
Within each cell type, the size and number of cisternae is roughly conserved

but between different species huge variations in morphology exist. Typical mammalian Golgi stacks consist of four to six cisternae [Alberts08], while some specific cell types can have up to sixty cisternae. Instead of having a Golgi ribbon, plant cells often feature dispersed individual Golgi stacks, that are associated with ER exit sites. A similar morphology appears after interfering with long-range transport in mammalian cells, e.g. after disassembly of microtubules via the drug nocodazole [Thyberg99].
Prominent exceptions to the stack morphology are the phenotypes found in the yeast *Saccharomyces cerevisiae* and in the fruit fly *Drosophila melanogaster*. While the former shows a distribution of individual cisternae dispersed in the cytoplasm [Preuss92], the latter shows (during certain stages of development) a collection of vesicles and tubules that are arranged like a bunch of grapes [Kondylis01].
Despite major advances in elucidating the molecular players that participate in the morphogenesis and biogenesis of the GA, the reason for the widely observed robust stack formation and alternative Golgi phenotypes has remained elusive. As will be shown in Chapter 5 the different phenotypes might be caused by alterations in the tethering and fusion machinery.

3.3.1 Intra-Golgi Transport

The current view of how the GA is established and maintained is intimately intertwined with general transport phenomena in the secretory pathway [Bonifacino04]. Currently, there is an ongoing debate about the exact nature of intra-Golgi transport. First, biogenesis and transport within the Golgi will be elucidated along the lines of the *cisternal maturation model*. Most of the current experimental data can be well reconciled with this model [Jackson09; Emr09]. In the subsequent section different perspectives will be provided and discussed.
VTCs arrive at the cis face of the GA [Scales97; Presley97] where they are thought to fuse with each other, hence forming a new cisterna (cf. Fig. 3.3, right). Due to a series of fusion events from initial COPII vesicles to large VTCs, an excess surface to volume ratio is being created, that might lead, among other causes, to the flattened cisterna shape [Rafelski08]. While new cisternae form constantly at the cis Golgi, older cisternae will be pushed through the stack and at some point older cisternae will disassemble at the trans side of the GA. Experiments show that this whole cisterna life cycle takes roughly 30 minutes [Hirschberg98]. This time period is also referred to as the *turnover time* of a stack.
Gradients of Golgi-resident proteins [Rabouille95] and SNAREs [Volchuk04] across the stack of cisternae allow for sequential modifications of cargo proteins and intra-Golgi vesicle transport. In order to maintain these gradients, retrograde COPI vesicles shuttle Golgi resident proteins to previous cisternae [Bonifacino04].

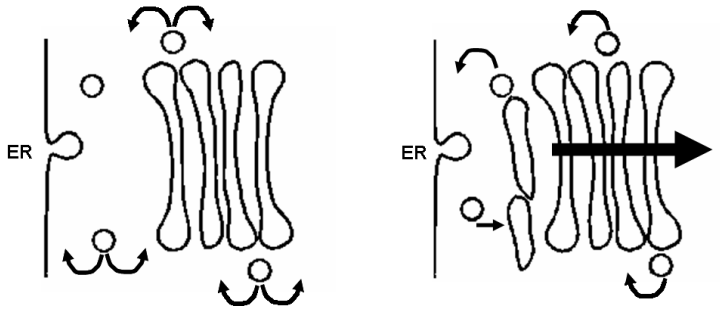

Figure 3.3: *Schematics of intra-Golgi transport models. Left) Vesicular transport model: Golgi cisternae are static entities and vesicles mediate anterograde and retrograde transport in between cisternae. Right) Cisternal maturation model: In a series of fusion events, COPII vesicles form larger membrane structures that build up new cisternae. Thus, cisternae will be pushed through the stack in time and will be disassembled at the back side of the GA. COPI vesicles mediate only retrograde transport.*

Exit of properly modified cargo proteins is provided by clathrin-coated vesicles [Kirchhausen00] and post-Golgi carriers that are not clathrin-coated [Glick09]. Depending on the type of cargo, theses carriers can be directed to endosomes or the plasma membrane [Luini08].
Integrity of the stack seems to be provided by so-called Golgi matrix proteins that tether adjacent cisternae to each other [Barr97; Seemann00]. Additionally channels and pumps seem to be responsible for the distinct intra-cisternal milieu [Maeda08] and could thus generate a pH gradient along the secretory pathway. Perturbation of the pH balance impairs glycosylation of cargo proteins and lipids [Kellokumpu02], and it can lead to missorting of Golgi resident proteins [Axelsson01].
Also gradients in lipid composition have been detected within the GA. Sphingomyelin and cholesterol concentrations increase from cis to trans Golgi concomitant with an increase of bilayer thickness along the secretory pathway [vanMeer98]. Morover, these gradients could switch proteins and lipids into a 'sorting state' [Weiss00]. Taken together, the mentioned changes in lipid and luminal composition can be regarded as some sort of maturation/aging of Golgi elements – a feature that will be part of the model presented in Chapter 5.

3.3.2 Alternative transport models

An alternative transport model, the *vesicular trafficking model*, was originally postulated in the mid 1970s [Palade75]. In this model, all larger membrane

compartments such as VTCs and Golgi cisternae are stable entities that are fixed in their position (cf. Fig. 3.3, left). Trafficking between these compartments is mediated by forward moving, coated vesicles. These vesicles are thought to carry only cargo while leaving Golgi residents behind.
However, when the predictions of this model were tested for COPI-dependent intra-Golgi trafficking steps, discrepancies that did not reflect experimental observations became obvious. For example, COPI vesicles were not found to be enriched in cargo but in Golgi resident proteins [Lanoix99; Lanoix01; Rabouille05; Martinez-Menárguez01].
Moreover, transport of large cargo proteins cannot be explained with the *vesicular trafficking model*. For instance, procollagen with a size of 300nm does not fit into conventional 60nm sized vesicles. Indeed, procollagen was shown to stay inside the cisternal space [Bonfanti98].
Furthermore, compelling evidence against the *vesicular trafficking model* comes from the yeast *Saccharomyces cerevisiae*. In this organism individual Golgi cisternae are dispersed throughout the cytoplasm and are therefore optically resolvable by fluorescence microscopy. By employing two types of fluorescent dyes, maturation of single cisternae could be directly visualized [Losev06; Matsuura-Tokita06].
Recently, the so-called *rapid-partitioning model* was proposed [Patterson08]. Cargo and Golgi residents are thought to be subject to rapid bidirectional transport, implying inter-cisternal connections across the Golgi stack. Sorting of lipids into domains occurs at each level of the Golgi and proteins associate with their preferred lipid environment. Two types of lipid environments are postulated. One could be enriched in glycerophospholipids (GPLs) and Golgi processing enzymes, whereas the other could consist of sphingolipids (SLs) toghether with a higher concentration of cargo. The latter domain is then thought to provide exit of the Golgi stack. Each of these domains is present within each cisternae of the Golgi stack, with increasing SL concentration from cis to trans. Therefore, export of cargo can occur at any level of the Golgi stack.
Although, recent electron tomography studies have revealed that nonequivalent cisternae of the Golgi stack could be connected [Marsh04; Trucco04]. These type of connections seem to be more prevalent when cells are experiencing high levels of Golgi traffic or when they face low temperatures [Martinez-Alonso05]. This indicates that intercisternal tubules are rather rare under standard physiological conditions. Since the rapid partitioning model postulates exit of secretory cargo proteins at all levels of the Golgi, findings of cargo waves that move across mammalian Golgi stacks [Trucco04] are at odds with this model. Moreover, exiting the Golgi at any given point of the stack could result in incompletely processed secretory cargo, that does not appear to happen under normal physiological conditions [Emr09]
Taken together, there seems to be currently an extensive experimental support

of the maturation model [Jackson09; Emr09]. Moreover, this model is appealing from a theoretical perspective, since it explains the dynamic and self-organizing properties of the GA.

3.3.3 Self-organizing GA morphology under external stimuli

The dynamic and self-organizing aspects of the Golgi complex can best be studied under the influence of mitosis or drugs that change the Golgi phenotype reversibly. For example, the depolymerization of microtubules via the drug nocodazole inhibits cellular long-range transport (cf. Fig. 3.4). That leads in mammalian cells to a breakdown of the Golgi ribbon. Subsequently, small dispersed but functional mini Golgi stacks appear in the vincinity of ERES [Cole96; Hammond00], thus resembling the distributed stack phenotype found in plant cells. Upon removal of the drug, the Golgi ribbon forms again within an hour [Ho89].

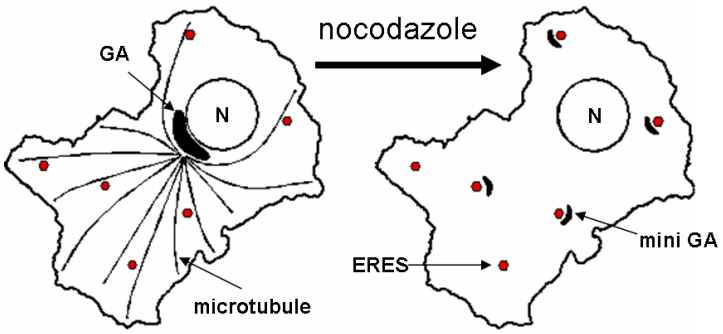

Figure 3.4: *Example of the dynamic properties of the GA ('N' denotes the cell nucleus). Upon microtubule depolymerization via the drug nocodazole, the Golgi ribbon breaks down into smaller functional subunits (mini Golgis) in the vincinity of ERES. The whole effect is reversible: after nocodazole washout the Golgi ribbon reemerges.*

The Golgi's dynamic reponse to changes in cargo flux can be seen by blocking the anterograde delivery of membranes and proteins, e.g. by prohibiting the emergence of COPII vesicles. This leads to the disassembly of the GA [Storrie98] by COPI-dependent and COPI-independent retrograde pathways [Girod99]. Hence, the GA can only exist if anterograde and retrograde transport are properly balanced.
One of the most important features of the GA is its capability to form de novo after cytokinesis. As has been indicated before, similar to cells' behaviour during

mitosis, the mammalian Golgi was thoroughly disrupted with a combination of the drugs brefeldin A (BFA) and H89. Upon removal of these drugs a functional Golgi reemerged suggesting that a new Golgi stack can arise by self-organization [Puri03].

Chapter 4

Diffusion and its role in structure formation

In this chapter, the major characteristics of diffusive motion will be reviewed. Subsequently, the influence of diffusion on pattern formation will be elucidated. To this end, requirements that are necessary for the emergence of spatial chemical patterns will be derived from a linear stability analysis of reaction-diffusion systems.

4.1 Brownian motion

Brownian motion describes the irregular movement of particles originating from random collisions with other particles. Thus, a particle's trajectory is well described by a so-called random walk. In a simple approximation, let us describe this motion by a hopping process of a particle in one dimension. The particle can jump a small distance ϵ with equal probability $p = 1/2$ to the left or to the right. If this jumping process is repeated a large number of times, n, the probability where the particle could be located, is well approximated by a Gaussian distribution as can be shown via the central limit theorem. The outcome of a Gaussian probability distribution is not restricted to this simple hopping model but applies to many common stochastic processes that are captured by the central limit theorem. The probability to find a particle, that was originally located at $x_0 = 0$ at location x after time t reads:

$$P(x,t) = \frac{1}{(4\pi D t)^{(d/2)}}\, e^{-\frac{x^2}{4Dt}} \tag{4.1}$$

Here, d denotes the embedding spatial dimension and D denotes the diffusion coefficient that is closely connected to the temperature of the system via the

fluctuation-dissipation theorem. Lateral diffusion of particles with radius R in a liquid of viscosity η at temperature T can be described via the Einstein-Stokes relation [Einstein05]:

$$D = \frac{k_B T}{6\pi\eta R} \quad . \tag{4.2}$$

Here, k_B represents Boltzmann's constant. This relation is valid in three dimensions. For two-dimensional systems, such as membranes, the situation turns out to be more complicated. The diffusion coefficient of a circular object embedded in a two-dimensional fluid diverges ('Stokes'-paradox'). To overcome this mathematical problem, the effect of the surrounding of the two-dimensional fluid has to be taken into account. Considering the viscosity of the surrounding fluid, η_c, the thickness of the two-dimensional sheet h, and its viscosity η_m a perturbation approach yields [Saffman75]:

$$D = \frac{k_B T}{4\pi\eta_m h}\left[\ln\left(\frac{\eta_m h}{\eta_c R}\right) - \gamma\right] \tag{4.3}$$

Here, the universal Euler-Mascheroni constant $\gamma \approx 0.5772...$ arises due to no-slip boundary conditions. The diffusion coefficient scales as $\propto \ln\left(\frac{1}{R}\right)$, i.e. diffusion coefficients decrease only weakly with particle radius in two dimensions.
For large radii, this approximation breaks down beyond a critical radius $R_c = \eta_m h/\eta_c$. An extended numerical analysis by Hughes et al [Hughes81] revealed an effective scaling:

$$D \propto \frac{1}{R}, \qquad R \ll R_c \tag{4.4}$$

When looking at how the diffusion coefficient influences transport behavior within a material, the mean squared displacement (MSD) $\langle x^2 \rangle$ is a useful measure. The MSD is the variance of the particle's probability distribution $P(x,t)$ (cf. Eq 4.1). For normal Brownian diffusion, the MSD grows linearly in time.

$$\langle x^2(t) \rangle \equiv \int_{-\infty}^{\infty} x^2 P(x,t) dx \tag{4.5}$$

$$\langle x^2 \rangle = 2dDt \tag{4.6}$$

In addition, diffusion of single particles can give rise to a macroscopic particle flux $\vec{j}$ as implied by Fick's first law. In this approximation, the particle flux depends linearly on concentration differences (Eq. 4.7). Respecting conservation (Eq. 4.8), one can derive Fick's second law, *the diffusion equation* (Eq. 4.9).

$$\vec{j} = -D\nabla C \tag{4.7}$$
$$\partial_t C = -\nabla \vec{j} \tag{4.8}$$
$$\partial_t C = D\Delta C \tag{4.9}$$

The diffusion equation reflects the temporal and spatial response of a system after a pertubation in its concentration C. A solution to this differential equation with initial condition $C(0,0) = \delta(x)$ yields a Gaussian propagator that agrees with Eq. 4.1.

$$C(x,t) = \frac{1}{(4\pi Dt)^{(d/2)}} e^{-\frac{x^2}{4Dt}} \tag{4.10}$$

From this propagator one can see that diffusion smears out an initial pertubation, leading to a uniform steady state. This result suggests that diffusion leads to the destruction of spatial patterns rather than to their emergence. Yet, this intuition is not entirely true as we will see in Sec. 4.4.

4.2 Anomalous diffusion

For Brownian motion the mean squared displacement grows linearly in time. In contrast, anomalous diffusion is defined by a nonlinear spreading of the MSD. Typically, a power law of the form $\langle x^2 \rangle \propto t^\alpha$ with $\alpha \neq 1$ is found. Anomalous diffusion plays an important role in a variety of systems ranging from human traveling behavior and the corresponding spreading of infectious deseases [Hufnagel04] to the scan path of the human eye [Brockmann99].
Anomalous diffusion can be divided into two classes, *subdiffusion*($\alpha < 1$) and *superdiffusion* ($\alpha > 1$). Subdiffusion is particularly important for cell biological processes: subdiffusive motion has been reported for the cytoplasm and nucleoplasm of mammalian cells [Wachsmuth00; Weiss04; Guigas08] as well as for bacteria and yeast [Tolić-Nørrelykke04; Golding06]. Moreover, transport within heterogeneous lipid membranes seems to be subdiffusive [Ratto03]. Most probably, subdiffusion is caused in living cells by macromolecular crowding [Weiss04; Banks05]. The emergence of subdiffusion can originate from three fundamentally different phenomena:

Obstructed diffusion Here, the particles are embedded in a special geometric environment in which diffusion is hindered by a maze of immobile obstacles. Depending on the size of the diffusing particle, the obstacle concentration, and

the size of the obstacles, diffusion can become anomalous. Typically, there exists a length scale beyond which the surrounding medium can be considered homogeneous. If this is the case, there exists a crossover time from anomalous diffusion to normal diffusion.
A prominent exception can be found in percolation systems at the critical point. Close to the percolation threshold, that is the critical density at which a randomly arranged medium loses its long-range connectivity, self-similarity arises on all length scales and the environment becomes fractal. Thus, particles can become trapped in a fractal hierarchy and consequently show subdiffusion on all length and time scales. The minimum anomaly coefficient predicted by percolation theory is $\alpha_P = 0.697$ and $\alpha_P = 0.526$ for two and for three dimensions, respectively [Bouchaud90].

Continuous time random walk (CTRW) Binding of particles can be another cause of subdiffusion. In this case, a tracer has to wait for a certain period of time before it can proceed its free random walk. Subdiffusion results if the waiting time distribution has no finite mean. This implies that a particle can be trapped for nearly an infinite period. A mathematical description of tracers due to immobilisation of traps is realized by the so called *continuous time random walk* (CTRW). One suitable waiting time distribution $w(t)$, that leads to subdiffusive behavior is:

$$w(t) \propto \quad (1-\beta)\, t^{\beta-2}, \qquad 0 < \beta < 1 \tag{4.11}$$

$$\alpha = \qquad 1-\beta \tag{4.12}$$

where the anomaly coefficient α is directly related to the power-law exponent of the waiting time distribution t. As a consequence, the CTRW has a distinct non-Gaussian propagator [Metzler00]. From a biological perspective, the immobilization period of a particle within a trap depends on the corresponding binding energy, and the two quantities are related via a Boltzmann factor $t_i \propto \exp(E_B/k_B T)$. After such a typical time the particle will return to a normal diffusive behavior unless there is an infinite hierarchy of traps with increasingly larger binding energies and corresponding longer waiting times. Moreover, it has to be added that the CTRW is non-ergodic: even for large sampling periods, the time average does not converge towards the ensemble average, due to the large fluctuations in waiting times [He08; Lubelski08].

Viscoelastic media Longterm correlations between diffusion steps, caused for example by a viscoelasic medium, can also give rise to subdiffusive behavior. The concept of viscoelasticity can be understood in terms of the Maxwell model: By

connecting a dashpot and an elastic spring in series and applying stress to the system, the system will first relax elastically and then creep slowly back to its original position.
According to Mandelbrot and van Ness, viscoelastic behavior can give rise to fractional Brownian motion (FBM) [Mandelbrot68]. Here, the calculus of independent Gaussian increments of Brownian motion is extended to statistically correlated increments [Goychuk09]. Due to this antipersistent random walk, subdiffusive behavior can emerge. From a physical perspective, the elastic component of the viscoelasic force opposes a particle's motion, thus trying to keep it in its current position.
In contrast to CTRW, ergodicity is presevered and the propagator for FBM looks reads [Sebastian95]:

$$P(r,t) \propto \frac{1}{t^{(2\alpha-1)/2}} \exp\left[-Cr^2/t^{(2\alpha-1)/2}\right] \tag{4.13}$$

Recent data favors FBM as the most likely cause for subdiffusion within cells [Pan09; Weber10] as experiments on crowded solution have ruled out CTRW as a cause for anomaly [Szymanski09].

4.3 Measuring diffusion in biological cells

Since the development of efficient fluorescent probes such as the green fluorescent protein (GFP), diffusion measurements in vivo are predominantly fluorescence based. In the following some common diffusion measurement techniques will be presented.

Single particle tracking microscopy (SPTM) In this method, individual fluorescent particles (i.e. fluorophores) are attached to relevant molecules. In the course of time the positional information of the fluorophore will be recorded, e.g. with a laser scanning microscope. The obtained particle trajectories can then be analyzed in terms of the MSD (cf. equation 4.5 in the case of normal diffusion). The advantage of this technique is that the individual behavior of particles can be revealed. Drawbacks of this method are that often only short trajectories can be obtained due to possible photobleaching of the fluorophore.

Fluorescence recovery after photobleaching (FRAP) In contrast to SPTM, FRAP measures the transport characteristics on an ensemble of fluorescent molecules [Axelrod76]. The typical setup of this method relies on a confocal laser scanning microscope. FRAP requires the illumination of a small area ranging

from $1 - 1000\mu m^2$ within a probe with high light intensity. Within this area, the illumination leads to irreversible chemical structural changes that cause the loss of the particles' fluorescent properties. Intact fluorophores from the surrounding reservoir diffuse into the region of interest and replenish the total fluorescent intensity. From the rate of the fluorecence recovery, transport coefficients such as diffusion coefficients can be determined. A highly attenuated illumination is employed to monitor this recovery process. This method is typically used for measurements on the micron and seconds to minutes scale.

Fluorescence correlation spectroscopoy (FCS) In FCS the correlation of fluorescence intensity fluctuations are analyzed [Magde72]. Typically, these intensity fluctuations originate from the thermal motion of particles and they are observed with a laser scanning microscope. When tracers leave or enter the focal volume, the fluorescence intensity changes. Fluorescent tracers within the focal volume L^3 possess typical residence times of the order $\tau \propto L^2/D$. Slow particles for instance will reside for a longer time within the focal volume yielding larger correlation times. Statistical analysis (autocorrelation of the fluctuations) yields the mean residence time. From the residence time and the dimension of the focal volume, the diffusion coefficient can be determined. The method features a high sensitivity because only a small number of molecules in a very tiny spot are observed. The analysis of FCS data requires small concentrations of fluorescencent probes to allow for the detection of individual molecule fluctuations. Compared to FRAP, FCS elucidates smaller time and length scales of the diffusion process.

Other methods Non fluorescent techniques for diffusion measurements involve magnetic resonance methods such as nuclear magnetic resonance (NMR) [Lepock83] and electron spin resonance (ESR) [Mastro84b; Mastro84a]. Here, probes with a specific spin label allow for the detection of rotational and translation diffusion coefficients.

4.4 Turing patterns as a means for cellular structure formation

Reaction–diffusion systems have attracted much interest as prototypical models for pattern formation. Moreover, it has been argued, that reaction-diffusion systems could be the basis for animal coats and embryogenesis [Murray04; Koch94]. At present, the concept of reaction-diffusion models is frequently applied on cellular length scales, e.g. in the context of bacterial cell division [Howard01; Kruse02].

All of these applications are based on Turing's groundbreaking manuscript in the year 1952 [Turing52]. Two interacting chemicals can form a stable inhomogeneous pattern if one substance diffuses much faster than the other and nonlinear reaction schemes are employed. Remarkably, under appropriate conditions diffusion creates concentration differences instead of smoothing them out. Two other essential processes play a role in spatial pattern formation, i.e. *local self-enhancement* and *long-range inhibition*.
One prominent example for a reaction-diffusion system is the Schnakenberg model [Schnakenberg79]. It is the simplest type of a tri-molecular reaction of two species, being supplied by different pools of molecules. The Schnakenberg model in its dimensionless form reads:

$$\begin{aligned} \partial_t u = &\quad a - u + u^2 v + D_1 \Delta u \\ \partial_t v = &\quad b - u^2 v + D_2 \Delta v \end{aligned} \tag{4.14}$$

where the rates a, $b > 0$ indicate the exchange of each individual species with its source pool, and D_1, D_2 denote the species' diffusion coefficients.
Another influential activator-inhibitor system was studied by Gierer and Meinhardt [Gierer72].

$$\begin{aligned} \partial_t u = &\quad a - bu + c\frac{u^2}{v(1+du^2)} + D_1 \Delta u \\ \partial_t v = &\quad e - fv + gu^2 + D_2 \Delta v \end{aligned} \tag{4.15}$$

Here, the term $\frac{u^2}{v}$ represents an autocatalytic reaction that is hampered at the same time by its inhibitor v; a and e are production terms, while b and f represent removal rates of the individual species. In addition, c, g are cross-reaction coefficients. A special feature of the system stems from the saturation constant d. Increasing d from 0 will slowly change the pattern from an intial dotlike arrangement towards a stripelike pattern [Koch94].
Pattern formation requires open thermodynamic systems. In that sense, the presented Schnakenberg model as well as the Gierer-Meinhardt model do neither exhibit particle nor engergy conservation. However, a variant of the Gierer-Meinhardt model was studied recently [Howard01] that showed pattern formation while preserving particle conservation.

4.5 General stability criteria

In this section, criteria for reaction-diffusion systems will be derived that reflect the stability of a chemical steady state. Let us assume we have a set of d

different particle species with concentrations $u_i(\mathbf{x}, t)$ for type $i \in \{1, .., d\}$ at position $\mathbf{x}$ and time t (vectors indicated by a bold font). Each species i is subject to diffusion with corresponding coefficient D_i. Chemical reactions that depend on local particle concentrations take place and are represented by functions $f_i(\mathbf{u})$ for each species i. In vector notation, this yields:

$$\mathbf{u}_t = \mathbf{f}(\mathbf{u}) + \mathbf{D}\,\Delta\mathbf{u} \tag{4.16}$$

Let us first determine steady state $\mathbf{u}_0$ of this system

$$\mathbf{u}_t \equiv 0 = \mathbf{f}(\mathbf{u}_0) \tag{4.17}$$

With this information, the whole problem can be linearized around each of its steady states $\mathbf{u}_0$. Let us now look at a slight perturbation of this state $\mathbf{u} = \mathbf{u_0} + \boldsymbol{\epsilon}$. Under conditions of perfect mixing, the steady state can assumed to be homogeneous. Hence, $\Delta\mathbf{u}_0 = 0$ and consequently $\mathbf{f}(\mathbf{u}_0) = 0$. From that, we can derive the system's dynamic response to the pertubation $\boldsymbol{\epsilon}$ to first order:

$$(\mathbf{u_0} + \boldsymbol{\epsilon})_t = \mathbf{f}(\mathbf{u_0} + \boldsymbol{\epsilon}) + \mathbf{D}\,\boldsymbol{\Delta}(\mathbf{u_0} + \boldsymbol{\epsilon}) \tag{4.18}$$

$$\boldsymbol{\epsilon}_t = \mathbf{f}(\mathbf{u_0} + \boldsymbol{\epsilon}) + \mathbf{D}\,\boldsymbol{\Delta}\boldsymbol{\epsilon} \tag{4.19}$$

$$\boldsymbol{\epsilon}_t \approx \mathbf{f}(\mathbf{u_0}) + \partial_{\epsilon_\mathbf{j}}\mathbf{f}(\mathbf{u_0})\,\boldsymbol{\epsilon} + \mathbf{D}\,\boldsymbol{\Delta}\boldsymbol{\epsilon} = \partial_{\epsilon_\mathbf{j}}\mathbf{f}(\mathbf{u_0})\,\boldsymbol{\epsilon} + \mathbf{D}\,\boldsymbol{\Delta}\boldsymbol{\epsilon} \tag{4.20}$$

The Jacobian matrix defines the stability matrix:

$$A \equiv \partial_{\epsilon_j}\mathbf{f}(\mathbf{u_0}) \text{ ,i.e.} \qquad \mathbf{A_{ij}} = \begin{pmatrix} \partial_{u_1} f_1 & \dots & \partial_{u_m} f_1 \\ \vdots & \ddots & \vdots \\ \partial_{u_1} f_n & \dots & \partial_{u_m} f_n \end{pmatrix}_{\mathbf{u_0}} \tag{4.21}$$

With this definition, we can test stability of the steady state in the absence of diffusion. To this end the stability matrix is diagonalized and the differential equation can be solved in the eigenbasis of A $\mathbf{w}$:

$$\partial_t \epsilon_i = A_{ij}\epsilon_j \tag{4.22}$$

$$\partial_t w_i = \lambda_i w_i \tag{4.23}$$

$$w_i = e^{\lambda_i t} \tag{4.24}$$

If the steady state is stable, a small pertubation decays in time and the system returns to its steady state. This implies that *all eigenvalues of the stability matrix have to fulfill*

$$\Re(\lambda_i) < 0 \qquad \forall i \in \{1, .., d\} \tag{4.25}$$

In case of two interacting substances ($d = 2$), equivalent conditions for negative eigenvalues are the requirements

$$\mathrm{Tr}\,(A) > 0 \qquad \text{and} \qquad \mathrm{Det}\,(A) > 0 \tag{4.26}$$

The conditions in Eq. 4.26 will be needed again in Section 4.7.

4.6 Diffusion-driven instability

Let us now include diffusion consider the full reaction-diffusion system, i.e. we do not neglect the term $D\,\Delta\boldsymbol{\epsilon}$ in Eq. 4.20 any more. By means of a spatial Fourier transformation, we can rewrite this equation in terms of wavenumbers, k. Evaluation of the Laplacian yields a factor $(ik)^2$:

$$\partial_t \tilde{\epsilon}_i = A_{ij}\tilde{\epsilon}_j + D_i(ik)^2\tilde{\epsilon}_i \tag{4.27}$$

$$\partial_t \tilde{\epsilon}_i = \underbrace{\left(A_{ij} - \delta_{ij}\, D_i k^2\right)}_{\equiv E_{ij}} \tilde{\epsilon}_j \tag{4.28}$$

with $\tilde{\epsilon}_i$ being the Fourier transform of the perturbation ϵ_i and δ_{ij} representing the Kronecker delta. The stability matrix is constant with respect to the spatial dimension $\mathbf{x}$ and thus contributes only as constant factor for the first term.
The extended stability matrix reads:

$$E_{ij} = \begin{pmatrix} \partial_{u_1} f_1 - D_1 k^2 & \dots & \partial_{u_m} f_1 \\ \vdots & \ddots & \vdots \\ \partial_{u_1} f_n & \dots & \partial_{u_m} f_n - D_n k^2 \end{pmatrix}_{\mathbf{u_0}} \tag{4.29}$$

Similar to the case without diffusive mixing, the stability matrix can be diagonalized and stability can be tested along the eigenvectors of E.
In order to obtain spatial patterns, some Eigenvalues $\lambda(k) > 0$ of the extended stability matrix E_{ij} have to be larger than zero for some wavenumbers $k^2 > 0$. At the same time, the steady state has to be robust when neglecting diffusion, i.e. $\lambda(k^2 = 0) < 0$. If these conditions are fulfilled, certain modes of the system will grow exponentially while the system as a whole remains stable – a pattern with a characteristic length scale determined by k will develop.
For an illustration how diffusion can lead to pattern formation let us look at a predator-prey example [Murray04]. Assume the predators reproduce in an

'autocatalytical' way and 'diffuse' slowly. Locally that can lead to high amounts of predators diminishing the amount of prey below the level of the steady state. That would result in a net flux of faster moving prey towards the regions with high amounts of predators thus sustaining this disbalance (cf. Fig. 4.1).

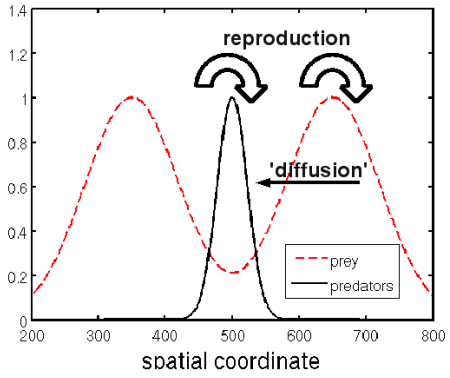

Figure 4.1: *Schematic illustration of the 'short-range activation and long-range inhibition' mechanism, which is involved in the formation of Turing patterns. Predators and prey reproduce. The prey spreads fast neighboring territories. Thus, there exist sufficient amounts of prey in the predator territory in order to supply the predators.*

4.7 Two-component system

In a system with two chemical components the conditions for pattern formation can be reduced to relationships between the required ratio of the species' diffusion coefficients, and the derivatives of the stability matrix (cf. equation 4.21). To this end, we determine the eigenvalues λ of E_{ij} in equation (4.29):

$$|E - \lambda I| = 0 \qquad . \tag{4.30}$$

$$\lambda^2 + \lambda[k^2 \underbrace{(D_1 + D_2)}_{>0} - \underbrace{(\partial_{u_1} f_1 + \partial_{u_2} f_2)}_{<0}] + h(k^2) = 0 \tag{4.31}$$

$$h(k^2) = D_1 D_2 k^4 - (D_2 \partial_{u_1} f_1 + D_1 \partial_{u_2} f_2) k^2 + \det(A) \tag{4.32}$$

For the stability of the steady state in the absence of any spatial effects, we required $\Re(\lambda(k^2 = 0)) < 0$ (Eq. 4.25). To be instable to perturbations, there

have to exist some wavenumbers $k \neq 0$ so that $\Re(\lambda(k^2)) > 0$. The coefficient after λ in equation 4.31 is positive, because on the one hand D_1, $D_2 > 0$. On the other hand, $\Re(\lambda(k^2 = 0)) < 0$ is required (cf. Eq. 4.26)

$$\mathrm{Tr}(A) \equiv \partial_{u_1} f_1 + \partial_{u_2} f_2 < 0 \qquad . \tag{4.33}$$

The only way that $\Re(\lambda(k^2))$ can be positive is if $h(k^2)$ is negative. Since we required for the determinant $|A| > 0$ in Eq. 4.26 the prefactor of k^2, $D_2\partial_{u_1} f_1 + D_1\partial_{u_2} f_2$ has to be positive. Hence, the ratio of the diffusion coefficients $D_2/D_1 \neq 1$, either the inhibitor has to diffuse faster than the activator or vice versa.
Eq. 4.33 is necessary but not sufficient. In addition, the minimum $h_{\min}$ has to be negative:

$$\frac{\partial}{\partial k^2} h(k^2) = 2D_1 D_2 k^2 - (D_1 a_{22} + D_2 a_{11}) = 0 \tag{4.34}$$

$$k^2_{\min} = \frac{D_1 a_{22} + D_2 a_{11}}{2D_1 D_2} \tag{4.35}$$

$$h_{\min} = |A| - \frac{(D_1 a_{22} + D_2 a_{11})^2}{4D_1 D_2} \tag{4.36}$$

where a_{ij} denote the coefficients of the stability matrix (4.21). Finally, the relation $h(k^2) < 0$ for some k^2 reads as

$$(D_2\partial_{u_1} f_1 + D_1\partial_{u_2} f_2)^2 > 4D_1 D_2 \det(A) \qquad . \tag{4.37}$$

All in all, we have derived four conditions in a system with two chemical components:

$$\begin{aligned} \partial_{u_1} f_1 + \partial_{u_2} f_2 &< 0 \\ \partial_{u_1} f_1 \partial_{u_2} f_2 - \partial_{u_2} f_1 \partial_{u_1} f_2 &> 0 \\ D_2\partial_{u_1} f_1 + D_1\partial_{u_2} f_2 &> 0 \\ (D_2\partial_{u_1} f_1 + D_1\partial_{u_2} f_2)^2 &> 4D_1 D_2 \det(A) \end{aligned} \tag{4.38}$$

The first two equations are equivalent to the requirement to obtain a stable steady state, whereas the latter two specify the conditions for spatial pattern formation.

Part II

Results & Discussion

Chapter 5

Self-organized morphogenesis of the Golgi complex

A hallmark of eukaryotic cells is their compartmentalization by membrane-engulfed organelles [Alberts08]. Understanding how these organelles form, self-organize, and maintain their identity while rapidly exchanging most of their protein contents is a major challenge.

In spite of all these detailed insights on the molecular level it has remained unclear how proteins and lipids act in concert to achieve the highly dynamic formation of a GA with its different phenotypes. In particular, it has remained elusive so far why/how a GA forms *de novo* (e.g. after mitosis), and how the GA dynamically attains and maintains its stack structure or the alternative phenotypes in yeast and flies.

Zooming out from the molecular and biochemical details, a computational model for the morphogensis of the GA is introduced that is capable of reproducing the experimentally observed Golgi phenotypes with physiological dynamics. While previous modeling approaches have addressed generic aspects of protein sorting in a given stack of cisternae [Glick97; Weiss00; Heinrich05], the focus is on the formation of the spatial structure itself. The model for the morphogenesis of a Golgi apparatus considers aspects of protein sorting only in minor detail whereas a fundamental understanding of under which conditions a stack of cisternae can form *de novo* and stay stable under stationary flux is provided. Major control parameters are the influx and outflux rates of membranes and proteins, and the parameter regimes are highlighted in which, for example, a stack structure can form. Based on these data, predictions are derived which process is responsible for the emergence of phenotypes.

5.1 Model definition

5.1.1 Philosophy of the model

Before giving details of the model for the morphogensis of a Golgi apparatus, its gross structure and main features will be sketched out. The length and time scales involved in Golgi morphogenesis (from molecular diffusion on the scale of 1μs and 10nm to shape changes on the scale of 15min and 100μm) clearly dictate that a detailed model, e.g. in the spirit of molecular dynamics, is computationally not feasible. Therefore, a coarse-graining has to be done that neglects detailed phenomena on fine scales while still allowing the simulation of the large scale events. This also requires that molecular players like COPI proteins, lipids, and accessory regulators cannot be modeled explicitely but rather enter the model only in terms of effective rates for certain events. Similar approaches are used when formulating mean-field models for biological phenomena, e.g. in the context of timing cell division [Pomerening03]. Dealing with membranes, i.e. two-dimensional objects embedded in three-dimensional space, a mean-field approach can be very demanding since the local geometry of membranes (curvature etc.) and topological changes (e.g. budding and fission) have to be considered. Simulations of discrete units, i.e. a particle-based approach, lends itself in this situation as the more appropriate tool for modeling. Following this rationale, the model for Golgi morphogenesis is based on discrete particles that have roughly the size of larger transport intermediates, e.g. VTCs. These particles enter a cubic simulation box at a window that mimics an ER exit site (ERES). Thus, the focus lies on the formation of a small Golgi compartment that is driven by diffusive transport of particles rather than motion that is driven by molecular motors. The simulation box hence resembles a scenario that occurs, for example, in the yeast *Pichia pastoris* or in mammalian cells with disrupted microtubules [Storrie98].

Particles are injected into the simulation box at the ERES region with rate J_{in}. Within the simulation box particles can diffuse, reversibly tether to, and irreversibly fuse with each other to form larger structures. Tethering (via Hookean bonds) imitates the action of Golgi matrix proteins while fusion accounts for the action of SNAREs. After fusion, larger structures behave similar to a fluid drop with a high surface-to-volume ratio, i.e. particles are mobile within the drop but try to assume a flat overall structure, hence assuming a pancake-like shape that is typical for cisternae.

To couple these mechanical degrees of freedom to some rudimentary implementation of the cisternal protein chemistry, each particle carries two 'protein pools' A, B. Species A shall represent, for example, the pool of SNAREs that mediate fusion events in the early cis Golgi. Proteins of species A are lost from particles

with rate r_A to model protein recycling. Protein species B (lost with rate r_B) may represent an anterograde cargo protein that leaves the Golgi apparatus after having been processed. Hence, both species measure the age (or degree of maturation) of particles and emerging cisternae. While species A reflects the fusion competence to newly arriving transport intermediates from the ER, species B determines how far the glycosylation processes have advanced.
As a basic readout, the number, size, and orientation of particle structures, e.g. cisternae was monitored. The balances between tethering and fusion, cisternal maturation (ageing) and material influx are found to be the dominant determinants of the phase space area in which stable stack formation is observed. All parameters of the simulation are listed in the appendix Tab. 9.1.

5.1.2 Setup of the model

To allow for an efficient computer simulation that captures the relevant length and time scales inherent to the self-assembly of a Golgi stack, not a full Golgi ribbon, but single Golgi stacks were simulated. These are naturally observed, for example, in the yeast *Pichia pastoris* or in mammalian cells after microtubules have been disrupted. As basic building blocks for the simulations spherical particles with radius $r_0 = 100$ nm were chosen. Structures of this size, so-called vesicular-tubular clusters (VTCs), have been observed as major transport intermediates between ER and the GA in living cells [Scales97; Presley97].

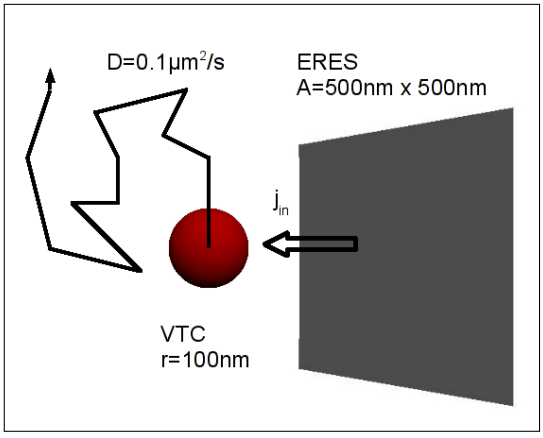

Figure 5.1: *Basic features of the model. Membrane carriers (VTC) were injected from a square ERES region into the simulation box according to a flux J_{in}. They could then explore the simulation box by diffusion. Upon collision with other VTCs, they could either fuse or form temporary bonds ('tethers').*

All simulation were performed using a cubic simulation box (4 μm edge length) with reflecting boundary conditions. New particles entered the volume from a square ERES region (500×500 nm^2) on one of the faces of the cube according to a flux J_{in} (cf. Fig. 5.1). New particles were assigned a random position inside the ERES region and could then explore the simulation box by diffusion.
Particle movement was implemented as Brownian dynamics, i.e. for each particle i the position vector was updated according to $\mathbf{x}_i(t + \Delta t) = \mathbf{x}_i(t) + \boldsymbol{\xi} + \Delta t \mathbf{F}_i/\gamma$. The components of the random vector $\boldsymbol{\xi}$ are independent, have zero mean and variance $2D\Delta t$ to allow for diffusion with a low diffusion coefficient $D = 0.1$ μm^2/s in the dense cytoplasm. The time increment was chosen as $\Delta t = 0.5$ ms. The term $\mathbf{F}_i$ denotes the sum of all conservative forces acting on particle i while $\gamma = k_B T/D$ is the friction associated with the diffusion coefficient.
To respect excluded-volume interactions, all particles were subject to a soft-repulsive potential that is commonly assumed in dissipative particle dynamics [Shillcock08]. Denoting by r_{ij} the center-to-center distance between two particles j and i, and by $\mathbf{e}_{ij}$ the unit vector pointing from j to i, the force on i is given by

$$\mathbf{F}^{\text{rep}}_{i,j} = k_{\text{rep}} \mathbf{e}_{ij} \begin{cases} 1 & r_{ij} \in [0, r_0] \\ 2 - r_{ij}/r_0 & r_{ij} \in (r_0, 2r_0] \\ 0 & r_{ij} > 2r_0 \end{cases} . \tag{5.1}$$

Here, the repulsion parameter k_{rep} sets the maximum force.
Whenever two particles i and j were separated by a distance $r_{ij} \leq r_c = 340$ nm, they were able to form a temporary bond, hence mimicking tethering via Golgi matrix proteins. Each particle was allowed to form up to three tether bonds, with the restriction of not pointing to the same aggregate. The forces of these bonds were chosen similar to Eq. 5.1 with a maximum force given by k_{tet}:

$$\mathbf{F}^{\text{tet}}_{ij} = -k_{\text{tet}} \mathbf{e}_{ij} \begin{cases} 0 & r_{ij} \in [0, 2r_0] \\ r_{ij}/r_0 - 2 & r_{ij} \in (2r_0, 3r_0) \\ 1 & r_{ij} \geq 3r_0 \end{cases} . \tag{5.2}$$

Formation and disruption of tethers occured stochastically with rates $r_{\text{on}} = 10/\text{s}$ and $r_{\text{off}} = 0.5/\text{s}$, i.e. the kinetics was assumed to be similar to the turnover time of COPI/II proteins on biomembranes [Elsner03; Forster06]. Tethers were also allowed to break instantly if the distance between tethered particles was larger than $r_c = 340$ nm.
Particles were allowed to fuse to build larger aggregates. If two particles (not being part of a common aggregate already) were tethered and had a distance $r_{ij} \leq 2r_0$, they were assumed to fuse to a larger aggregate with a probability that depended on their protein contents (see below for details). To allow for the

fluidity of larger fusion aggregates, each particle i within an aggregate determined all companion particles j within a radius r_c. Each of these m_i companion particles contributed a density-dependent interaction force of the form

$$\mathbf{F}_{ij}^{\text{fluid}} = \frac{2F_0}{M(r_c - 2r_0)} \begin{cases} 2r_0 - r_{ij} & r_{ij} \in [2r_0, r_0 + r_c/2] \\ r_c - r_{ij} & r_{ij} \in (r_0 + r_c/2, r_c) \\ 0 & \text{else} \end{cases} \tag{5.3}$$

to maintain the aggregate ($M = \min\{m_i, m_j\}$, $F_0 = 17\mu\text{N/m}$). Density-dependent forces deriving from a potential of the form Eq. 5.3 are commonly used to prevent a complete collapse of aggregating units [Pagonabarraga01].
Since Golgi cisternae are flat membrane structures that behave mechanically as a fluid drop, an additional force was introduced to flatten out aggregates. To this end, every particle was assigned an internal variable which was modelled as a spin $\mathbf{s}$, so that any pair of particles i, j within r_c within an aggregate could interact via dipole-dipole potentials

$$U_i^{\perp} = \alpha_{\perp} \sum_j \left((\mathbf{e}_{ij}\mathbf{s}_i)^2 + (\mathbf{e}_{ij}\mathbf{s}_j)^2 \right) \tag{5.4}$$

$$U_i^{\parallel} = -\alpha_{\parallel} \sum_j \mathbf{s}_i \mathbf{s}_j \tag{5.5}$$

Here, $\alpha_{\perp}$ and $\alpha_{\parallel}$ represent bending stiffnesses. The forces acting on particle i and thus its displacement are derived from the gradient of the potential. In each timestep, all dipole moments were equilibrated via a Monte Carlo algorithm. To this end, each spin orientation was randomly varied and the step was accepted according to the Metropolis criterion using $U_i^{\text{tot}} = U_i^{\perp} + U_i^{\parallel}$. Hence, all spins aimed at being parallel in the same plane, yet thermally induced deformations like bending modes were still allowed.
Since every particle in the system, being part of an aggregate or not, may be viewed as a transport intermediate, each particle was assumed to carry two protein species (A, B) as molecular cargo. Species A may reflect, for example, cognate SNAREs that mediate fusion of VTCs with early Golgi cisternae, while species B may reflect secretory cargo that has been posttranslationally modified. Hence, both protein species determine the age of a particle or an aggregate of particles that may be identified with a cisterna of the GA. Upon entering the simulation box, new particles were assigned an initial protein concentrations $M_A(t = 0) = 100$ and $M_B(t = 0) = 0$.
Each particle (being free or part of an aggregate) lost $\Delta M_A = 25$ proteins of species A with probability P_A within each time step. These proteins were lost from the system, i.e. they were put back into the infinite pool of particles that

equipped new particles before entering the system. The loss rate of an aggregate of size n was hence depending on the size of an aggregate as $r_A = nP_A/\Delta t$. Within an aggregate of size n, all particles $i = 1, \ldots, n$ were assigned the same fraction of proteins, $c_i(A) = N_A/n$. This value determined the fusion probability for two particles i and j belonging to different aggregates as

$$P_{ij}^{\text{fuse}} = r_{\text{fuse}}\,\Delta t\,\frac{c_i(A)\,c_j(A)}{c_0^2} \tag{5.6}$$

where r_{fuse} denotes the optimal rate with which fusion events were allowed. All pairs of particles that fulfilled the necessary conditions of being tethered were allowed to fuse (see above) were tested with the above probability within each time step.
Protein species B accumulated in each particle with rate r_B following a similar scheme to the loss of species A, i.e. each particle gained $\Delta M_B = 25$ proteins of species B per time step according to the probability associated with rate r_B. Above a threshold $c_{\text{max}} = 100$ an aggregate of size n (i.e. a cisterna) was allowed to send off particles (i.e. transport vesicles) towards the plasma membrane with probability

$$P^{\text{fiss}} = n\,r_{\text{fiss}}\Delta t \tag{5.7}$$

where $r_{\text{fiss}} = 1/\text{s}$ denotes the maximum budding/fission frequency. The latter is necessary to ensure that a whole cisternae only gradually disolves after reaching c_{max}.

5.1.3 Quantitative analysis of phenotypes

In order to avoid counting single particles as cisternae, all aggregates larger than 60% of the largest aggregate were counted as cisternae. The median of the number of cisternae was monitored starting after 20min (or $2.4 \cdot 10^6$ time steps), i.e. after the typical stack turnover time found in experiments [Hirschberg98], up to the end of the simulation. The monitored fluctuations in the median, i.e. the variance around the mean, were used to determine error bars. The same approach was used to determine the size of cisternae.
To obtain a quantitative measure for successful formation of a cisternal stack, an order parameter S was defined. To this end, for each aggregate a reference particle i with spin $\mathbf{s}_i$ was selected randomly and all remaining spins $\mathbf{s}_j$ ($j \neq i$) of the aggregate for which the scalar product $\mathbf{s}_i \cdot \mathbf{s}_j$ was negative were inverted ('re-orientation'). From this set of spins, the average spin $\mathbf{s}_k^c$ of each aggregate k was calculated. The set of average spins of all aggregates was then flipped as described for the individual spins within one aggregate.

Subsequently, for each pair of aggregates (i, j) all normalized connection vectors between the constituting particles of the aggregates were calculated. The orientation of these connection vectors was always from the younger (lower amount of protein species B) to the older aggregate (higher amount of protein species B). The mean of the connection vectors derived from this set were weighted with the inverse variance of the principal components ($= \mathbf{e}^{c}_{i,j}$), hence highlighting the co-planarity of the two aggregates. The order parameter was then defined as

$$S = \frac{\left| \sum_{i,j} n_i n_j \mathbf{e}^{c}_{i,j} \cdot \mathbf{s}^{c}_{i} \right|}{\sum_{i,j} n_i n_j} \tag{5.8}$$

with the aggregate sizes n_i, n_j. For proper stack formation, i.e. co-planar aggregates (cf. Fig. 5.3), hence $S \to 1$ is observed, while scattered aggregates yielded values for S near to zero.

5.2 Cisternae size and amount in the protein exchange limiting case

In this section analytic expressions for cisternae size, amount of cisternae and stack turnovertime are derived for a special case. To this end,spatial arrangements are disregarded and it is assumed, that all newly incoming VTCs fuse to the same aggregate as long as this aggregate has enough fusion proteins of species A. Otherwise, new VTCs will form another cluster.
Let $\tau_f^{(1)}$ denote the time, in which a single VTC is in generale able to fuse with other VTCs. Each VTC is assumed to carry an amount of proteins corresponding to m vesicle budding events before beeing depleted. This situation can be described via a *negative binomial distribution*. Here, the 'amount of successes' is fixed, in contrast to a *binomial distribution* with fixed amount of 'experiments'. The probability of a single vesicle fusion/budding event is given by p and the probability of having the mth event in the $m + s$ th step equals

$$f\left(m, s; p\right) = \binom{m+s-1}{s} p^m \left(1-p\right)^s \tag{5.9}$$

This provides the mean number of total steps for the complete depletion of fusion SNAREs and thus $\tau_f^{(1)}$ is then given by

$$\tau_f^{(1)} = \Delta t \, m \frac{1-p_A}{p_A} \approx m \frac{1}{r_A} \qquad (p_A \ll 1) \tag{5.10}$$

where Δt denotes the time step and p_A, r_A are respectively the loss probability and rate for species A.
If new VTCs enter the box with a mean rate J_{in}, then the mean time λ until the next one enters is given by $\lambda = \frac{1}{J_{\text{in}}}$. According to the assumption if $\tau_{\text{f}}^{(1)} \geq \lambda$, the new VTC is able to fuse with the old one and thus forming a dimer with a prolonged time $\tau_{\text{f}}^{(2)}$, during which fusion is possible. This can be generalized for the lifetime of arbitrary cluster sizes:

$$\tau_{\text{f}}^{(2)} = \frac{1}{2}\left(\tau_{\text{f}}^{(1)} + \tau_{\text{f}}^{(1)} + \lambda\right) \tag{5.11}$$

$$\tau_{\text{f}}^{(n)} = \frac{1}{n}\left(n\tau_{\text{f}}^{(1)} + \sum_{j=1}^{n-1} j\lambda\right) \tag{5.12}$$

$$\tau_{\text{f}}^{(n)} = \frac{1}{n}\left(n\tau_{\text{f}}^{(1)} + \frac{n}{2}(n-1)\,\lambda\right) \tag{5.13}$$

$$\tau_{\text{f}}^{(n)} = \tau_{\text{f}}^{(1)} + \frac{n-1}{2}\lambda \tag{5.14}$$

The expected cisterna size in number of VTCs n_s is determined by setting the lifetime $\tau_{\text{f}}^{(n)}$ equal to the time needed to add n VTCs to the system (first VTC is already there). Therefore,

$$\tau_{\text{f}}^{(1)} + \frac{n_s - 1}{2}\lambda = (n_s - 1)\;\lambda \tag{5.15}$$

$$n_s = \frac{2\tau_{\text{f}}^{(1)}}{\lambda} + 1 = 2\tau_{\text{f}}^{(1)}\,J_{\text{in}} + 1 \tag{5.16}$$

$$n_s \approx 2\,m\,\frac{J_{\text{in}}}{r_A} + 1 \qquad (p_A \ll 1) \tag{5.17}$$

Similarly, the turnover time of the stack (Eq. 5.20) and the expected number of cisternae (Eq. 5.22) can now be calculated. The time after which either a single VTC $\tau_{\text{rm}}^{(1)}$ or a cluster of size n $\tau_{\text{rm}}^{(n)}$ is removed from the system, can be determined exactly the same way as for species A:

$$\tau_{\text{rm}}^{(1)} = \Delta t\, m\frac{1-p_B}{p_B} \approx m\frac{1}{r_B} \qquad (p_B \ll 1) \tag{5.18}$$

$$\tau_{\text{rm}}^{(n)} = \frac{1}{n}\left(n\,\tau_{\text{rm}}^{(1)} + \sum_{j=1}^{n-1} j\,\lambda\right) \tag{5.19}$$

$$\tau_{\text{rm}}^{(n_s)} = \tau_{\text{rm}}^{(1)} + \tau_{\text{f}}^{(1)} \approx m\left(\frac{1}{r_A} + \frac{1}{r_B}\right) \tag{5.20}$$

where p_B and r_B denote the probability for an import event of species B and the corresponding rate respectively. The lifetime of a cluster with expected size n_s is thus given by Eq. 5.20. The lifetime $\tau_{\mathrm{rm}}^{(n_s)}$ is equal to turnover of the stack, since within the lifetime of the cluster the whole material of stack is replaced once. Now, the expected amount of cisternae n_c can be calculated:

$$\langle n_{\mathrm{tot}} \rangle = \tau_{\mathrm{rm}}^{(n_s)} J_{\mathrm{in}} \tag{5.21}$$

$$\langle n_{\mathrm{c}} \rangle = \frac{\langle n_{\mathrm{tot}} \rangle}{n_s} = \frac{\tau_{\mathrm{rm}}^{(1)} + \tau_{\mathrm{f}}^{(1)}}{2\tau_{\mathrm{f}}^{(1)} + \lambda} \approx \frac{\tau_{\mathrm{rm}}^{(1)} + \tau_{\mathrm{f}}^{(1)}}{2\tau_{\mathrm{f}}^{(1)}} = \frac{r_A}{2r_B} + \frac{1}{2},\ \lambda \ll \tau_{\mathrm{f}}^{(1)} \tag{5.22}$$

In equilibrium, the average total amount of VTCs in the simulation box $\langle n_{\mathrm{tot}} \rangle$ is constant, and it can be calculated by considering how many VTCs are produced within the turnover time (Eq. 5.21).
Since the total amount of VTCs in the system and the average cisternae size are known, the total amount of cisternae (5.22) can be calculated in a straightforward manner.

5.3 Results

First the simulation setup was tested whether it was capable of showing a *de novo* formation and dynamic maintenance of Golgi stacks without a pre-existing template. Starting from an empty simulation box into which new particles ('VTCs') were injected from an ERES-like area on one face of the simulation box, frequently the formation of a dynamically maintained stack structure was observed (Fig. 5.2). The first cisternal assemblies emerged within 2-3 minutes and a preliminary stack structure was formed within 10-15 minutes. This stack subsequently became stable as a dynamic steady-state structure while individual cisternae still underwent a maturation process, i.e. cisternae showed an aging process according to a change in protein contents (species A, B; cf. above).
To avoid uncertainties if an aggregate should be counted as a proper stack or not, an order parameter S was defined that yields an unbiased way to determine if a stack has emerged (Eq. 5.8). Basically, S quantified whether adjacent clusters of particles (putative cisternae) did form parallel, concentric sheet-like structures that are ordered according to increasing age. The classification via the order parameter S agreed well with a classification by eye. For $S \geq 0.75$, a proper stack structure was observed (Fig. 5.3) while smaller values were associated with a distorted or even lacking stack structure.
Having observed the possibility for a *de novo* generation of a stack structure, the important question arises as to within which parameter regime a robust stack

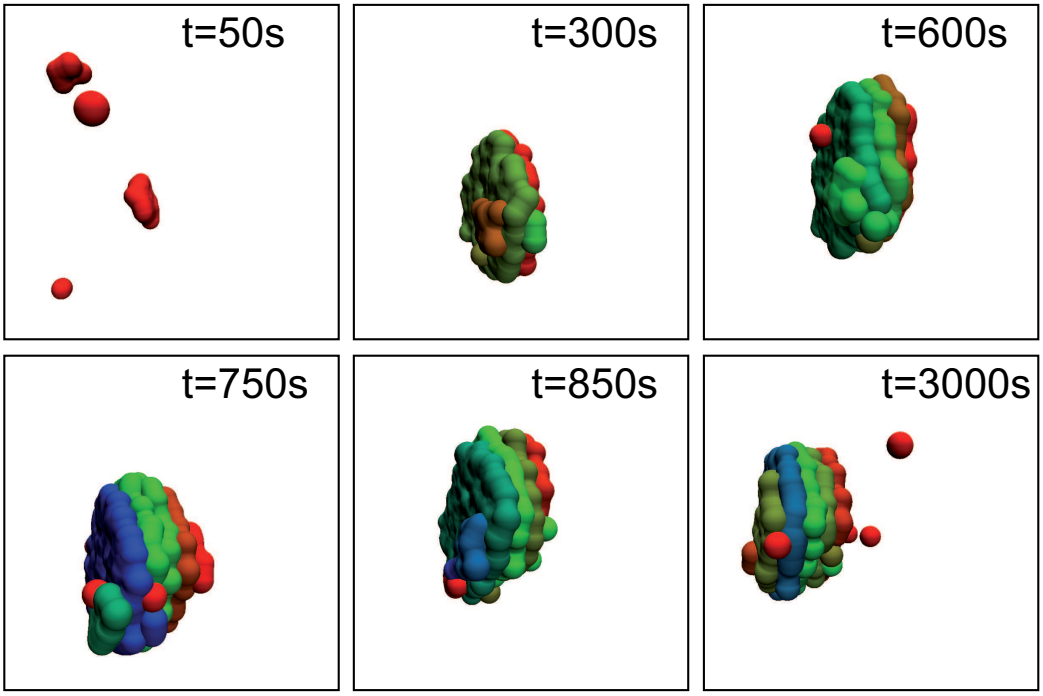

Figure 5.2: *Representative snapshots of a time series showing the* de novo *formation of a Golgi stack (parameters:* $J_{in} = 0.6/s$, $r_A = 0.04/s$, *and* $r_B = 0.005/s$*). Starting from an initially empty simulation box, a steady-state stack developed after about 700s that was dynamically maintained until the end of the simulation (*$t = 3000s$*). The maturation state of a cisterna, i.e. its age as measured by the amount of protein species A, is color-coded. Red and green color denote young (*cis *) and intermediate (*medial *) cisternae, while blue color represents old (*trans *) cisternae that are about to disassemble.*

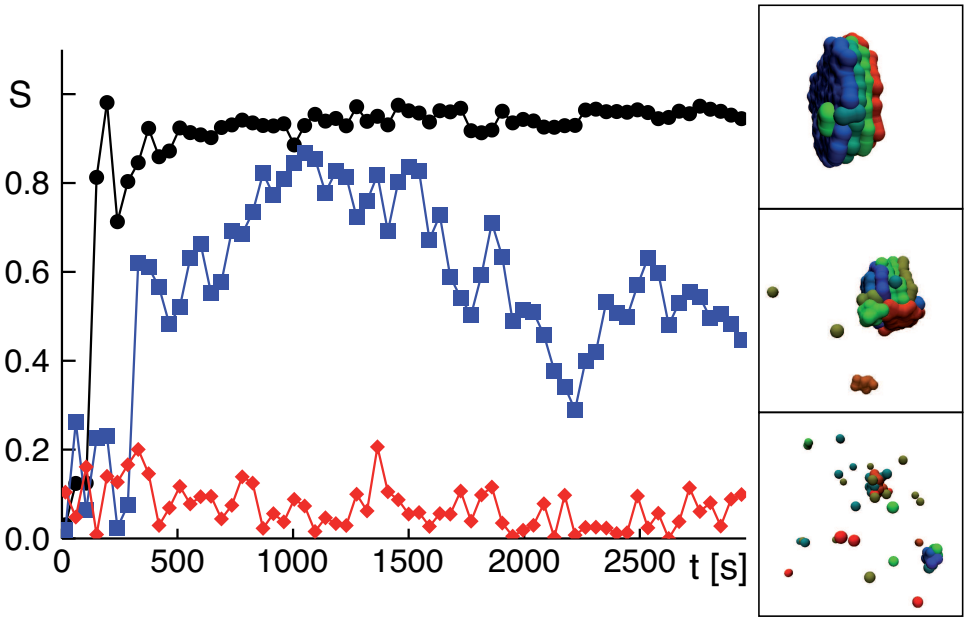

Figure 5.3: *Temporal evolution of the order parameter S for three representative parameter settings, $J_{in} = 0.8/s$ (dots), $0.5/s$ (squares) and $0.1/s$ (diamonds); in all cases $r_A = 0.04/s$, $r_B = 0.005/s$. Snapshots of the final configuration are shown on the right. For $S \geq 0.75$ proper stacks were observed, while lower values indicated a more or less compromised stack structure.*

formation is observed. Before addressing this point it was briefly examined which factors determine the amount and size of cisternae.
Owing to the maturation process, i.e. the loss of 'fusion SNAREs' with rate r_A (cf. Methods), the youngest compartment (*cis* cisterna) looses its fusion competence for incoming particles within a time $T_A \sim 1/r_A$. The amount of particles that enter the simulations box during this period, and hence are able to join and build up the youngest cisterna, therefore scales as $\sim T_A J_{in}$. Here, J_{in} is the number of new particles ('VTCs') that enter the simulation box from the 'ERES region' within one second. Following this simple scaling argument (cf. Sec.5.2 for a more rigorous calculation), the total number of particles per cisterna should grow linearly with J_{in}/r_A. Indeed, the simulation results for varying J_{in} and r_A (relying only on simulations for which $S \geq 0.75$) agree very well with these prediction (Fig. 5.4a). Concerning the prefactor, the theoretical prediction in fact slightly overestimates the cisternal size since not all particles fuse to one and the same cisterna during the period T_A.
To estimate the number of cisternae, let us recall that glycosylated cargo molecules are gained with rate r_B (cf. above). While $T_A \sim 1/r_A$ determines the period after which the youngest cisterna stops growing, $T_B \sim 1/r_B$ provides a time scale on which this youngest cisterna will eventually disassemble. Hence, the ratio of these times, i.e. r_A/r_B, provides a measure for how often a cisterna disassembles while a new one is being built up. Based on this consideration (cf. Sec.5.2 for a more rigorous calculation), the number of cisternae is predicted to scale with r_A/r_B. To test this prediction, the median amount cisternae of several simulations with varying r_A and r_B was plotted (keeping $S \geq 0.75$) as a function of r_A/r_B. In agreement with these prediction, a linear growth of the number of cisternae with r_A/r_B was observed (Fig. 5.4b). Only for very large r_A/r_B a significant deviation of the numerical data from the theoretical prediction was detected due to an incomplete equilibration of the system during the simulation time.
By definition, the rate r_B with which glycosylated cargo proteins were gained also determined the turnover time of the stack, i.e. during which period all material in the stack will be replaced by material coming from the ERES. Indeed, the numerically determined turnover time showed a linear dependence on $1/r_B$ (Fig. 5.4c) in the physiologically relevant range (10-25min has been estimated experimentally for a complete turnover of a Golgi stack [Hirschberg98]). Similar to these theoretical prediction for the cisternal size, the prefactor of the linear scaling deviated slightly from the numerically obtained data due to the simplicity of the argument.
In summary, the size of cisternae is determined by J_{in}/r_A while the number of cisternae is given by r_A/r_B; the stack turnover time is approximately given by $1/r_B$. With these insights, it was now possible to explore the range of parameters

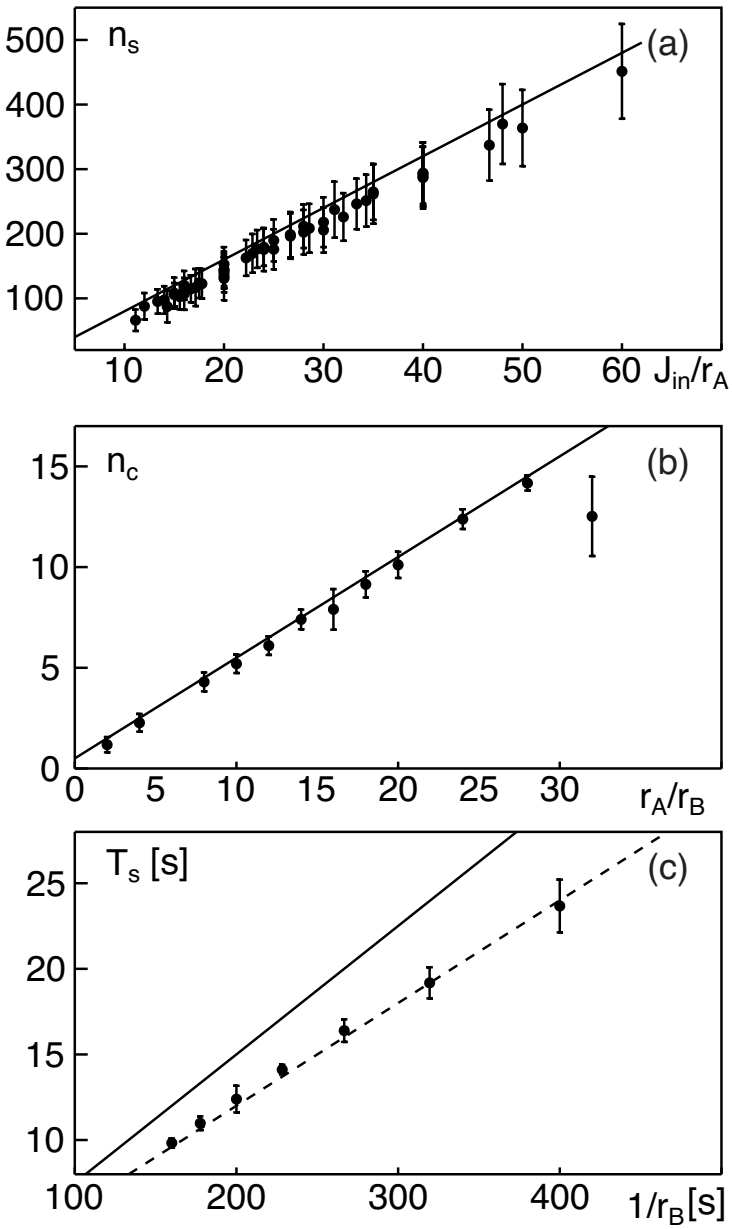

Figure 5.4: *(a) The size of a cisterna (measured as the number n_s of participating particles) grows linearly with J_{in}/r_A as predicted. Numerical data are shown as symbols with error bars being derived from the standard deviation of n_s within each simulation. The solid line corresponds to the theoretical prediction (see main text and Supplement). (b) The amount of cisternae n_c increases linearly with r_A/r_B as predicted theoretically. Numerical data (symbols) were determined in the time interval 20-50min, error bars denote the standard deviation of n_c within each simulation. The solid line corresponds to the theoretically predicted linear relationship (see main text and Supplement). (c) The turnover time T_s of the stack grows linearly with the inverse aging rate r_B (symbols and dashed line). Deviations from the theoretical prediction (full line) most likely are due to the simplicity of the argument.*

in which stack formation is possible.

To explore the range of parameters in which stack formation is possible, J_{in}, r_A, and r_B were varied while keeping the ratio r_a/r_B fixed. With the chosen ratio, one could expect on average 4-5 cisternae if a stack was able to form (as determined via the order parameter S). As a result, the formation of regular stacks (defined via $S \geq 0.75$) was found to occur for a wide range of parameters, i.e. it is a very robust phenomenon (Fig. 5.5). In particular, the key ingredient for stack formation at a given ratio r_A/r_B is the influx of new material from ERES, J_{in}. Reducing the rate r_B at which cargo is finished (the parameter that also determines the turnover time) at a given J_{in} stabilized stack formation since the period during which cisternae could build up and organize themselves was long enough so that even a low material influx could sustain proper stack formation.

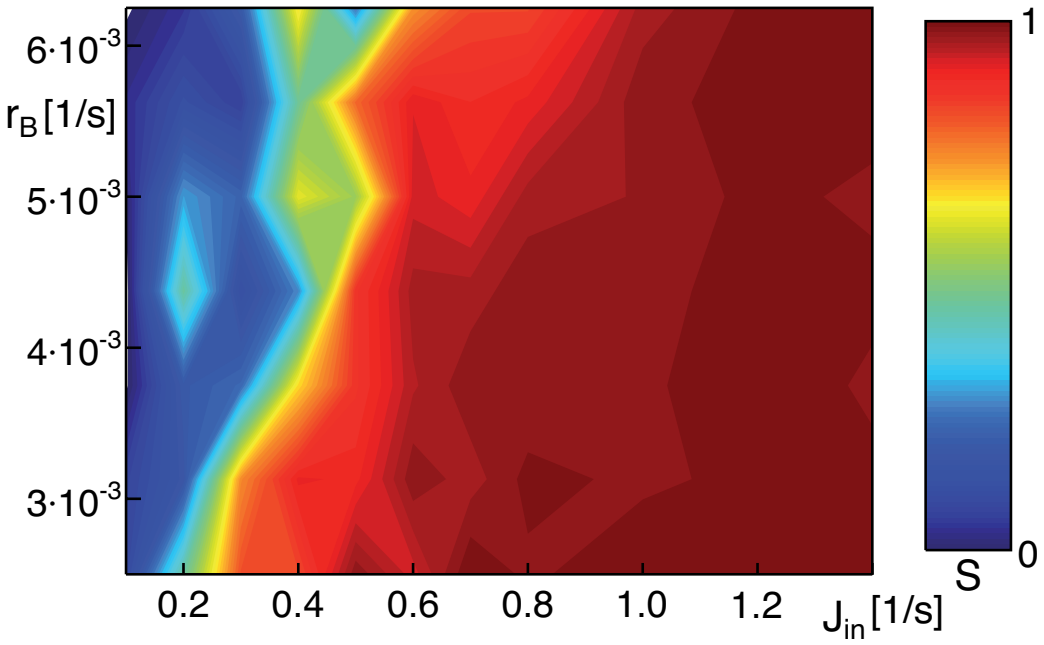

Figure 5.5: *Map of the order parameter S as function of influx rate J_{in} and aging rates r_A, r_B. While the individual parameters were varied, the ratio $r_A/r_B = 8$ was kept constant to have on average 4-5 cisternae. Proper stacks, defined via $S \geq 0.75$ were found for a broad set of parameters.*

Based on our above results, the question emerged how the number and spatial arrangement of ERES regions influences the formation of Golgi stacks. As a first step, the area of the ERES region was decreased from a $500 \times 500\text{nm}^2$ to a $250 \times 250\text{nm}^2$ window. Moreover, J_{in} was varied while keeping $r_A = 0.04/\text{s}$ and

$r_B = 0.005/\text{s}$ fixed. Again stable stacks emerged yet they formed already for $J_{in} \geq 0.4/\text{s}$ as compared to the slightly higher threshold $J_{in} \approx 0.6/\text{s}$ for a larger ERES (Fig. 5.6a). This result highlights that the influx rate, i.e. the rate at which COPII vesicles are produced, is the dominant parameter while a smaller width of an ERES region may only help to focus the influx of material towards an emerging structure.

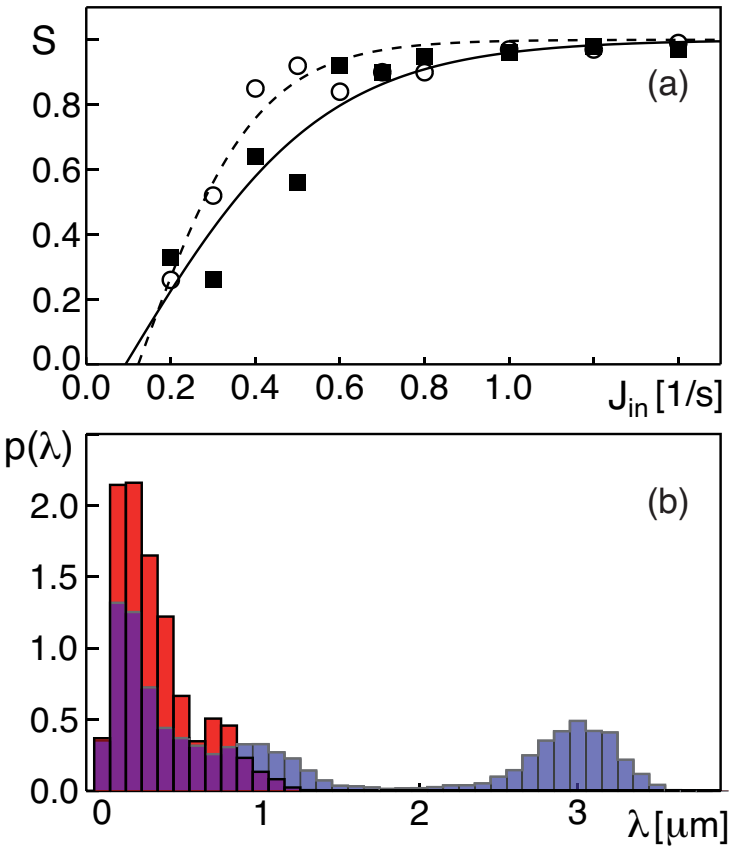

Figure 5.6: *(a) The average order parameter S increased slightly more rapidly as a function of the flux J_{in} when the ERES area was decreased from* $500 \times 500nm^2$ *(full symbols, solid line) to* $250 \times 250nm^2$ *(open symbols, dashed line). (b) Lateral distance distribution of VTC-clusters with two ERES regions per simulation box that are either* $1.2\mu m$ *(red) or* $3\mu m$ *(blue-transparent) separated.*

Under which conditions can two neighboring ERES give rise to two distinct stacks? To address this question, simulations with $r_A = 0.04/\text{s}$, $r_B = 0.005/\text{s}$, $J_{in} = 1.2/\text{s}$ and two ERES (each having an area of $500 \times 500\text{nm}^2$) at one face of the simulation box were performed. The distance between ERES was varied

in the physiological range of $1.2 - 3.5\mu m$. As a result, it was observed that two distinct stacks could only emerge if the ERES separation was at least 2μm. The emergence of two stacks (initially quantified by inspection of the simulation snapshots) can be visualized by the distance distribution of emerging cisternae, $p(\lambda)$. When only a single stack formed, $p(\lambda)$ showed a single peak below $0.5\mu m$ since all cisternae are in close proximity (Fig. 5.6b). When a second stack emerged, $p(\lambda)$ showed a second peak, indicating the emergence of another length scale in the simulations that is associated with the center-to-center distance of the two stacks (Fig. 5.6b). Indeed, the observation that ERES-dense regions give rise to a larger single stack, while well-separated ERES build up 'their' individual stack is supported by observation in nocodazole-treated cells that exhibit mini-Golgis near to ERES [Storrie98].

5.4 Discussion

Summarizing the results, it was shown that the *de novo* formation of Golgi stack structures can be understood in a minimal self-assembly model. This model relies on the balance of anterograde and retrograde flux, and on the rate with which the chemical identity is altered ('aging', 'maturation').
For the chosen parameters, the time scales for a *de novo* formation of a stack structure and its steady-state turnover compare favorably to experimentally accessible data: In steady state, the typical turnover of a Golgi stack takes 10-25min. [Hirschberg98] while the *de novo* formation of a GA takes about 30min. [Puri03]. Provided that a sufficiently high anterograde flux of membrane carriers is given, i.e. if J_{in} is high, the presented model indeed confirms the formation/turnover of a stack structure within these physiological time scales. Reducing J_{in}, i.e. reducing the secretory flux, the size of cisternae is predicted to shrink and ultimately a disorganization of the stack is observed. This observation matches nicely the experimental reports that introducing a dominant negative mutant of the Sar1 GTPase, i.e. hampering cargo export at the level of the ERES, leads to a decrease of cisternae size with subsequent dissassembly [Osterrieder10].
The model also highlighted that a change of the exit site area, which acts as the source for an anterograde flux, has only minor effects on the structure formation. Changing the proximity of ERES, however, had a significant effect since the inter-ERES distance determined if all anterograde material accumulated in a single stack structure or gave rise to more than one stack. Owing to the simulation setup, the entry window of new material (the 'ERES') may alternatively be interpreted as the terminal end of a bundle of microtubules. The simulation box hence would represent a juxtanuclear volume element towards which VTC-like

entities are transported along cytoskeletal tracks while within the simulation box motors and the cytoskeleton are neglected. In fact, including the intimate interactions of cisternae, motors, and microtubules would require a massive extension of model parameters. These aspects are beyond the scope of this study, but are the subject of ongoing and future work.

Since the loss rate of early SNAREs, r_A, and the rate of maturation r_B as well as the influx of membrane carriers J_{in} crucially determine the appearance of a stack structure, it is necessary to discuss these rates (and how to change them) in a detailed biological context.

The anterograde secretory flux that is summarized in J_{in} lies at the very heart of any Golgi structure formation and a lack of material flux abolishes the formation or maintenance of any Golgi structure. The flux J_{in} essentially quantifies the amount and contents of vesicles that emerge at ERES. Hence, the value of J_{in} can be modulated by changing the cargo load (cf. [Farhan08] for an experimental realization). Indeed, poisoning export at ER exit sites by massively overexpressing a hydrolysis-incapable Sar1 mutant (Sar1T39N) leads to the disappearance of the Golgi apparatus [Storrie98; Girod99; Osterrieder10]. More differential effects, i.e. partial destruction or shape perturbation of the Golgi, may be obtained by tuning the degree of Sar1T39N expression, by (partially) downregulating COPII components via RNAi and/or by inhibiting protein synthesis via cycloheximide (all of which decreases J_{in}). Using time-lapse microscopy or fluorescence recovery after photobleaching (FRAP) on cells with disrupted microtubules (to ensure the local formation of Golgi structures) may be used to determine J_{in}, while electron microscopy and tomography may be used to determine the geometrical properties of a stack. Controlled overexpression of secretory cargo on the other hand may help to increase J_{in}. The latter approach also may be used to change the size and distance distribution of ERES [Farhan08], i.e. the model predictions concerning the influence of ERES distances on (local) stack formation can be tested.

Changing the rates r_A and r_B is somewhat less straightforward. Since r_A is associated with retrograde transport of SNAREs, mediated by COPI proteins, the most direct approach to manipulate r_A is an interference with COPI proteins. Perhaps the most feasible way to experimentally modulate the parameter r_A is by modifying the action of ARFGAPs that stimulate GTP hydrolysis as these are crucial for vesicle formation and protein sorting. Another possibility could be the overexpression of inhibitory SNAREs [Varlamov03], that affect retrograde transport by interfering with the fusion machinery.

By construction, the maturation rate r_B describes the internal ageing of cisternae and consequently the cisternal decomposition time during which carriers are exported, e.g to the plasma membrane. Owing to this very definition, different molecular processes that progress in parallel are lumped into r_B, e.g. the sequential glycosylation of cargo proteins, the formation of clathrin-dependent carriers,

or the change in pH and lipid thickness of individual cisternae. Given this multitude of contributing factors, the most straightforward way to alter the value of r_B may be an interference with clathrin-mediated transport, the dominant path for post-Golgi trafficking. Also, downregulating Golgi resident enzymes, i.e. slowing down the glycosylation processes, may be a way to reduce r_B.
A basic mechanism that was employed in the simulations was the formation of temporary bonds ('tethers') between different membrane aggregates. On the molecular level, tethering of cisternae during different stages of maturation may be provided by Golgi matrix proteins like GRASP65/55 and/or GM130 [Barr97; Shorter99]. Tethering VTCs to cisternae, however, rather may invoke golgins [Drin08]. As a result of our simulations it was observed that modifying the formation of tethers dramatically alters the phenotype. Allowing tether formation prior to fusion (an event that most likely relies on SNAREs but does not have to involve Golgi matrix proteins), but disallowing tether formation after fusion resulted in a phenotype that resembles that of the yeast *S. cerevisiae* (Fig. 5.7a): Clusters of different age floated independently within the simulation box with a fair number of single VTCs in between. This observation suggests that the different yeast phenotypes observed in *S. cerevisiae* and *P. Pastoris* are due to differences in golgins and/or Golgi matrix proteins.
A completely different structure emerged when the loss rate r_A was massively enhanced. This would mean, for example, that SNAREs are rapidly backtransported to the ER, hence abolishing the fusion competence of the Golgi *cis* compartment with new incoming VTCs. For this case simulations gave rise to grape-like structures consisting of a large amount of very small stacks (Fig. 5.7b). Still, the structure retained a maturation order as evidenced by the radial age distribution of the aggregate (Fig. 5.7c). This phenotype is reminiscent of observations made for early stages in the embryogenesis of *Drosphila melanogaster* [Kondylis01; Kondylis09], hence suggesting that the rate r_A, at which new cisternae lose their fusion competence with newly arriving VTCs, is here much faster than in many other eukaryotes. Different molecular mechanisms could be responsible for this, e.g. an enhanced retrograde transport of fusion SNAREs or an increased expression of inhibitory SNAREs that might hamper fusion events.
In the presented model a scenario in which Golgi stacks are subject to maturation was tacitly assumed since several lines of evidence support this view [Losev06; Matsuura-Tokita06]. The exact nature of intra-Golgi transport, however, is still under debate and a variety of mechanisms has been proposed (see, e.g., [Jackson09] for a recent review). By construction the model, does not allow one to directly test the validity of the maturation model. However, an experimental falsification of the above predictions on the emerging Golgi phenotypes when altering the fundamental rate constants (r_A, r_B, and J_{in}) could provide strong evidence that maturation may not be the dominant means of intra-Golgi

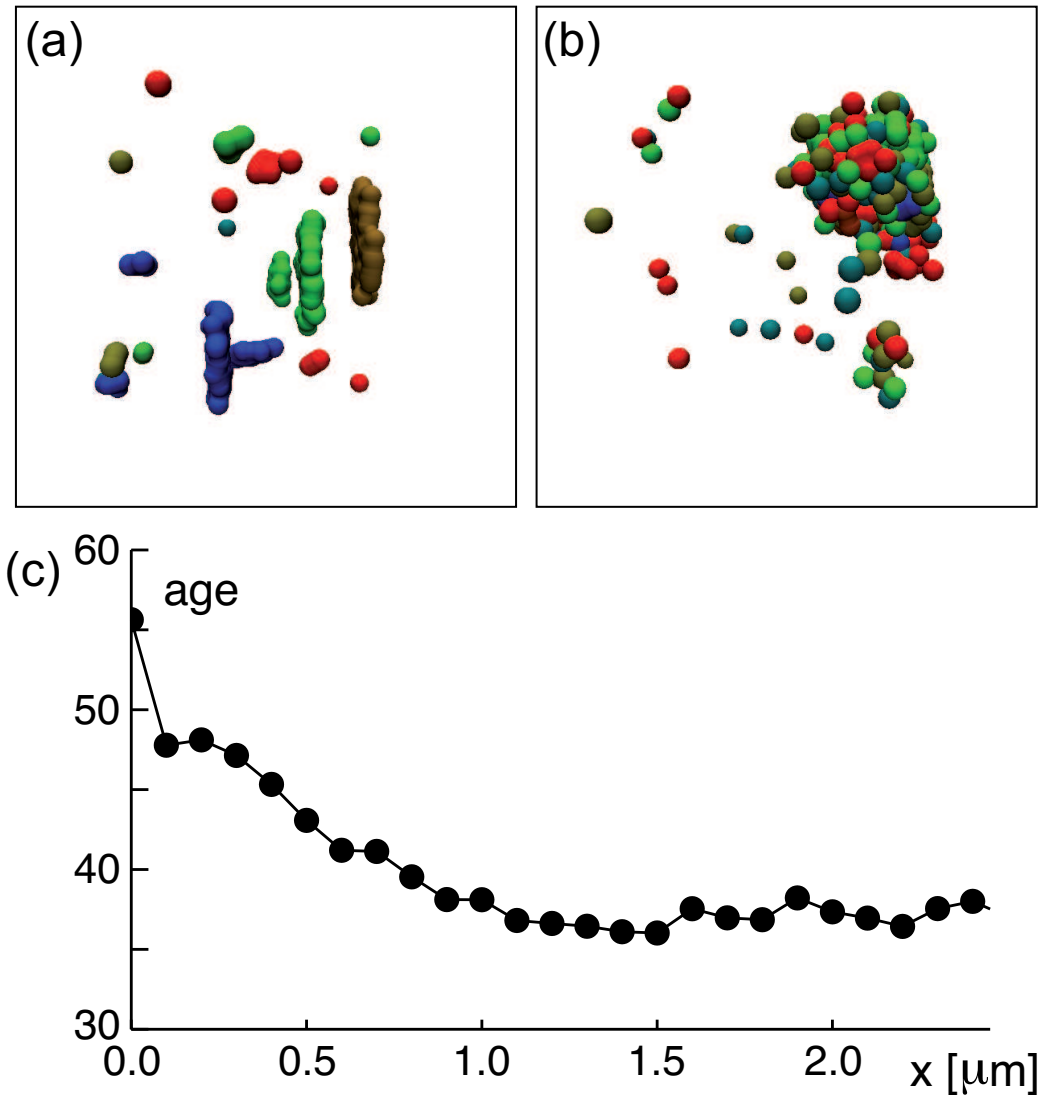

Figure 5.7: *(a) Inhibiting tether formation resulted in a phenotype of single, free-floating cisternae reminiscent of observations in* Saccharomyces cerevisiae*. (b) An enhanced loss rate of SNAREs ($r_A = 0.32/s$) while keeping $J_{in} = 0.6/s$ and $r_B = 0.005/s$ fixed leads to grape-like structures of small VTC-clusters, reminiscent of observations in* Drosophila melanogaster*. (c) The maturation stage of the grape-like structure depends on the radial distance x from the center of mass of the structure. A maturation age of 100 corresponds to a unit that is marked for immideate disassembly, whereas a zero value indicates a freshly injected VTC.*

transport.
Taken together, the large variety of different GA morphologies found in nature is captured by this self-organization model (cf. Fig. 5.8) which reduces the emergence of phenotypes to basically three important parameters that summarize the action of individual classes of proteins. Clearly, future work will be needed to unify the morphology approach taken here with previously published, more explicit descriptions of protein sorting and selection [Heinrich05]. Such an elaborate model ultimately should be able to reproduce the steady state distributions of Golgi residents across a self-assembling Golgi apparatus [Nilsson93; Rabouille95; Whitehouse97; Cosson05].

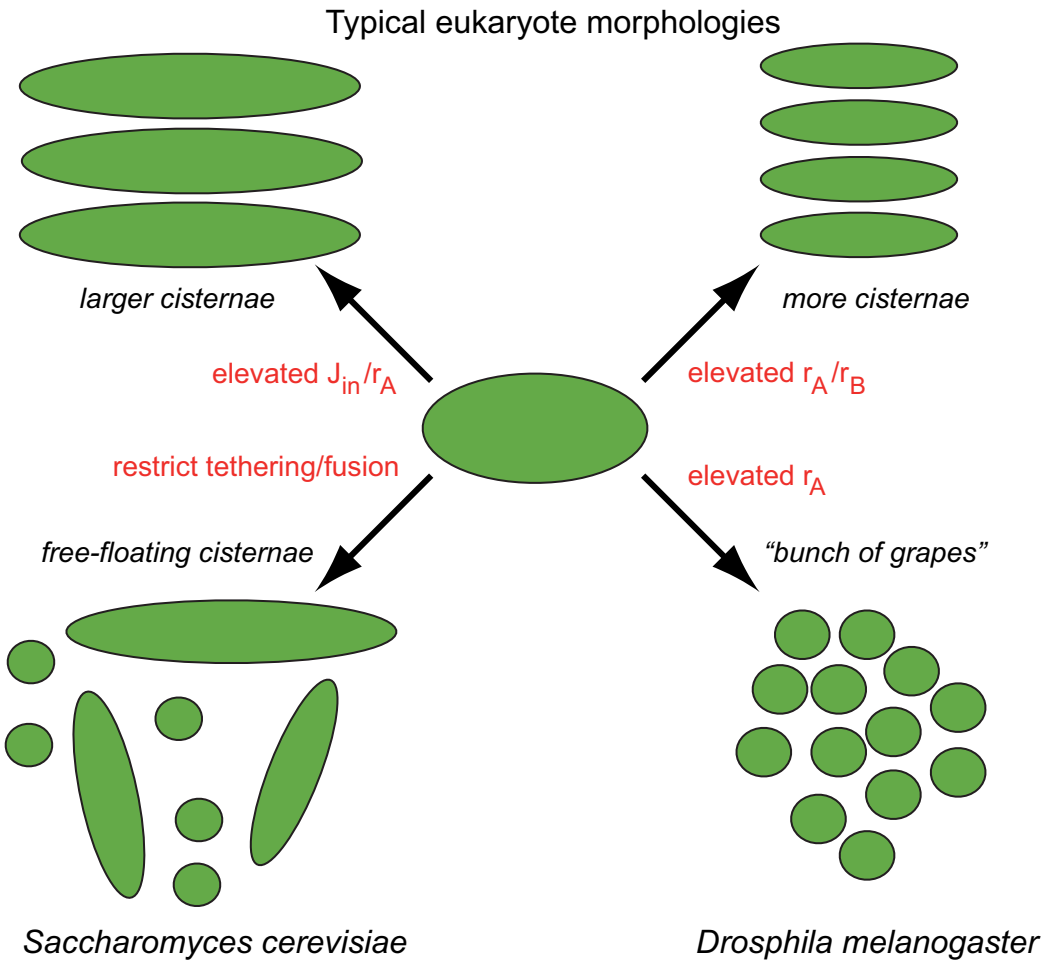

Figure 5.8: *Morphology diagram showing the correspondence of the predicted structure of the self-assembled Golgi stacks with their biological phenotypes as a function of the model's key parameters. Parameter J_{in} is the export rate of transport intermediates from ERES regions; r_A is the retrograde loss rate of protein species A (e.g. representing SNAREs of the Golgi-ER interface); r_B is the rate at which protein species B (e.g. cargo proteins that are modified in the Golgi) reaches its functional form. The tether rate determines the speed at which bonds form between VTCs and growing cisternae. See text for details.*

Chapter 6

COPI Hydrolysis - a curvature mediated process?

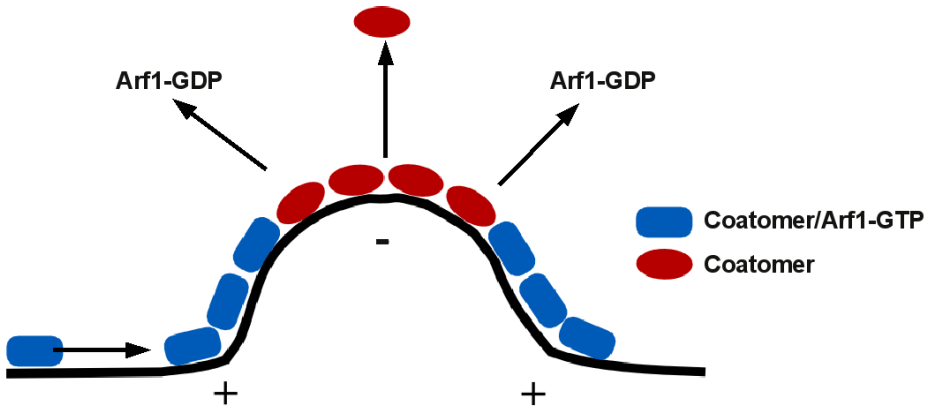

Figure 6.1: *Schematics of a curvature-sensitive ArfGAP induced GTP hydrolysis by Arf1 during COPI vesicle formation. Arf1-GTP/coatomer complexes (blue rectangles) diffuse on the membrane and polymerize. In regions of positive curvature hydrolysis is impeded, while in regions of negative curvature hydrolysis is enhanced, leading to Arf1 detachment. Negative curvature leads therefore as well to faster detachment of coatomer (red ellipses). Since the Arf1/coatomer complex induces curvature while curvature leads at the same time to a faster detachment, the process is intrinsically unstable.*

As we have have seen in Sec. 3.2.2, vesicle formation at the Golgi apparatus is driven by the COPI vesicle machinery, i.e. the proteins Arf1, ArfGAP, and coatomer [Spang98]. Upon nucleotide exchange from GDP to GTP, soluble Arf1 proteins firmly associate with Golgi membranes and subsequently bind the large

coatomer complex that drives membrane curvature, and therefore bud/vesicle formation. ArfGAP also binds to Golgi membranes and stimulates the hydrolysis of GTP by Arf1 [Cukierman95], therefore triggering the dissociation of Arf1 and coatomer from the membrane . Recently, it was observed that the stimulating effect of ArfGAP depends on the local curvature of the membrane [Bigay03; Bigay05; Ambroggio10]. Since the Arf1/coatomer complex induces curvature while curvature-sensitive coat detachment leads at the same time to a faster detachment, the process is intrinsically unstable.
Here, a simple model was formulated to probe the generic hypothesis whether a curvature-modulated dissociation could indeed provide an efficient mechanism for bud/vesicle formation despite its intrinsic instability. Specifically, a one-dimensional model was employed with parameters that are consistent with those that have been measured for the COPI machinery. Strikingly, it was found that curvature-modulated coat detachment facilitated vesicle formation at least as efficiently as stochastic coat detachment with a constant average rate. Taken together with the biological benefit of a faster shedding of vesicle coats, these findings suggest that a curvature-sensitive mechanism is indeed advantageous for the cell.

6.1 Setting up the model

To probe the hypothesis that curvature-modulated coat dissociation may fine-tune the formation of buds and vesicles, a simplified yet generic model was formulated: a one-dimensional chain of $2 \times N$ nodes was constructed, arranged as two parallel coupled bead-spring models (6.2a). Each node was connected to its two neighboring nodes within the same string. Additionally the nodes were connected to nodes in the opposing string (see below for details). The model hence is reminiscent to the cross-section of a lipid bilayer, i.e. two mirror symmetric monolayers. Due to this similarity, the two strings of the chain will be denoted as 'leaflets' in the following. Unless stated otherwise, the chain had the topology of a closed circle, which could mimic the closed envelope of a Golgi compartment, for example.
To denote whether a curvature-inducing coat molecule was bound, each node could adopt two states, termed 'coated' and 'uncoated'. If a node was coated, a spontaneous curvature was locally implemented by imposing an 'area difference' between the leaflets. This was achieved by introducing different equilibrium distances between springs in upper and lower leaflet.
Coupling of a node i to its neighbors j (as described above) was implemented via Hookean springs

$$\mathbf{F}^{\text{std}}_{i,j} = -k_{i,j}\mathbf{e}_{ij}(r_{ij} - \ell_{i,j}) \tag{6.1}$$

with $k_{i,j}$ being the spring constant, ℓ the relaxation distance, and $\mathbf{e}_{ij} = \mathbf{r}_{ij}/r_{ij}$ denoting the unit vector pointing from j to i. In addition, a bending potential was imposed

$$U_{\text{bend}} = k_{\text{bend}}(1 - \cos\theta) \tag{6.2}$$

for each node and leaflet. Here, the angle at each node i is defined via the scalar poduct $\mathbf{r}_{i,i-1} \cdot \mathbf{r}_{i,i+1} = r_{i,i-1} r_{i,i+1} \cos\theta$. with $i \pm 1$ denoting the neighboring nodes within the same leaflet.

Coat molecules were assumed to attach to and dissociate from the chain. Coats were allowed to adsorb to a free node i_0 of the upper/outer leaflet with rate $\gamma_{\text{on}} = 0.1/\text{s}$ if at least one of the node's next neighbors i_1 within the leaflet also was uncoated. Coat adsorption hence blocked two nodes $(i_0\,, i_1)$ in the upper/outer leaflet. In addition, the opposing nodes j_0 and j_1 in the lower/inner leaflet were also invoked. Uncoated nodes were assumed to have a relaxation distance $\ell = 2r_0$ to their three adjacent neighbors with a spring constant $k_{i,j} = k_0$. Coat adsorption altered the spring constant to $k_{i,j} = 2k_0$ and also changed the distances to $\ell_{i_0,i_1} = 2.2r_0$ and $\ell_{j_0,j_1} = 1.8r_0$. Thus, in the spirit of the famous area-difference model for lipid bilayers a spontanous curvature was imposed [Miao94] by assigning different widths to the pairs of nodes in the upper/outer and lower/inner leaflet. To increase the stability of this difference, also the diagonals $i_0\,, j_1$ and $i_1\,, j_0$ were connected with a relaxation length $\ell = \sqrt{8}\, r_0$ (spring constant $k_{i,j} = 2k_0$). Coat dissociation (hence restoring all relaxation distances and spring constants to $2r_0$ and k_0 respectively) occured either with a constant rate $\Gamma_{\text{off}} = \Gamma_0$ or according to the local curvature c, $\Gamma_{\text{off}} = \Gamma_1\, c$. In turn, the curvature c of the chain $(x(t), y(t))$ was determined via [Bronstein83]:

$$c = \frac{x'y'' - y'x''}{x'^2 + y'^2} \tag{6.3}$$

The motion of coat molecules on the chain was implemented via a hopping model. A coat (i.e. the state of four invoked nodes) was allowed to hop diffusively to an uncoated next-nearest neighbor node along the chain contour with diffusion coefficient D_0. To account for the movement of coat patches (i.e. a cluster of coated nodes), the diffusion coefficient was scaled with the total length of the cluster, $D(n) = D_0/n$. In one dimension the hydrolysis of a coat subunit in the middle of a larger cluster leads to the splitting of the cluster. However, in two dimensions coat subunits of larger clusters are thought to rearrange and adapt their structure. In oder to account for this effect coated nodes with a distance $d \leq 4r_0$ were given an increased probability of 90% of hopping towards each other while the probability of hopping in the opposite direction was set to 10%. When two clusters came into direct contact, they were assumed to fuse to a single cluster that moved as a single entity.

Given that coat proteins have a size of 10 nm [Matsuoka01; Lederkremer01] set the intrinsic length scale to $r_0 = 2.5\,nm$. The equations of motion for each node i in a two-dimensional space were given by the Langevin equation,

$$\mathbf{x}_i(t + \Delta t) = \mathbf{x}_i(t) + \boldsymbol{\xi} + \Delta t \mathbf{F}_i/\gamma_v \quad . \tag{6.4}$$

Here, the components of the random vector $\boldsymbol{\xi}$ have zero mean and variance $2D\Delta t$ with $\Delta t = 7.5 \cdot 10^{-5}\tau$ being the time increment. τ represents the selfdiffusion time of a node, i.e. $D \equiv 1\, r_0^2/\tau$. γ_v specifies the viscosity of the surrounding fluid. In the appendix in Tab. 9.2 force coefficients are given in terms of system's viscosity as required for Eq.6.4.
By assuming a typical diffusion coefficient for membrane proteins of $D_0 = 1\mu m^2/s$, the time scale for coat dynamics was fixed to $\Delta T = 25\,\mu s$. One step time step of coat dynamics (binding, unbinding and hopping) was followed by $500\Delta t$ to equilibrate to the new chain configuration.

6.2 Results

First, a linear chain with periodic boundary conditions was implemented to determine the bending stiffness. Here, the adsorption of coat molecules was not taken into account, i.e. all nodes were 'uncoated'. The chain's persistence length in the tensionless state can easily be determined by fitting Eq. 2.8. Hence, the chain was equilibrated to a tensionless state with a barostat [Venturoli99]. This type of barostat adjusts the box size by allowing for fluctuations of the simulation box with probabilies that are in accordance with the canonical ensemble. Analysis of the chain's fluctuation spectrum yielded a persistence length of $\sim 7\mu$m for the above mentioned parameters. Thus, the found persistence length is consistent with the length scales that are relevant when considering the dynamics of living cells.
Next, it was tested whether budding events are possible on a ring-like chain with coat adsorption according to the scenario outlined above. Two stochastic regulation mechanisms of coat dissociation were considered, i.e. one with constant average dissociation rate, $\Gamma_{\mathrm{off}} = \Gamma_0$, and one with a detachment rate that depended linearly on curvature, $\Gamma_{\mathrm{off}} = \Gamma_1 c$. When starting from an initial circular configuration, both mechanisms supported the formation of larger buds for sufficiently small detachment rates (cf. Fig. 6.2b-e for an example).
Subsequently, the range of dissociation rates (Γ_0 and Γ_1) was screened for the occurence of budding events while leaving the on-rate γ_{on} constant. In order to compare the fundamentally different detachment mechanisms one needs to find a corresponding metric because the rates Γ_0 and Γ_1 cannot directly be linked. However, both mechanisms alter the coat detachment flux from the membrane.

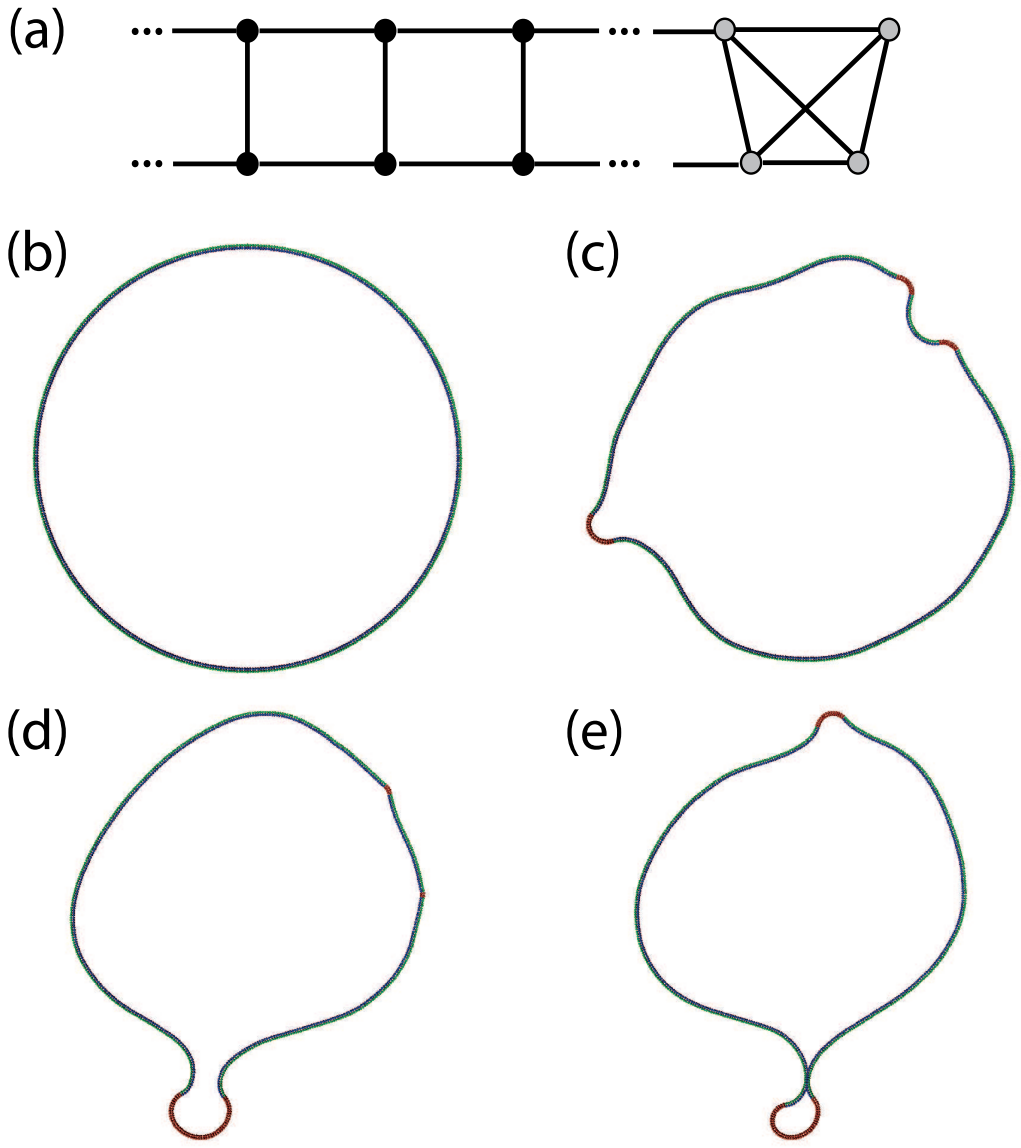

Figure 6.2: *(a) Setup of the model. Two 'leaflets' of nodes, connected with harmonic springs form a chain into which spontaneous curvature can be introduced by altering the relaxation distances in the two leaflets (see main text for details). (b-e) Successive snapshots of a budding event of a closed chain.*

Again, a change in the desorption flux alters the amount of coat that is adsorbed to the membrane which can also be easily determined in experiments. Thus, the surface corverage $\Omega = n_{coat}/N$ provides a feasible measure of comparison.
Specifically, the bud formation probability $\mathcal{P}$ was monitored as a function of Ω. In particular, multiple simluations (from 4 in the regions of high/low Ω up to 15 simulations in the intermediate Ω regime) were performed for a period of $10^8 \Delta t = 5s$ for each parameter set. In each simulation the following quantities were determined: (i) the fraction $\mathcal{P}_{\mathrm{bud}}$ of simulations that showed at least one bud, and (ii) the average time until a bud with 'Omega'-shape had emerged.

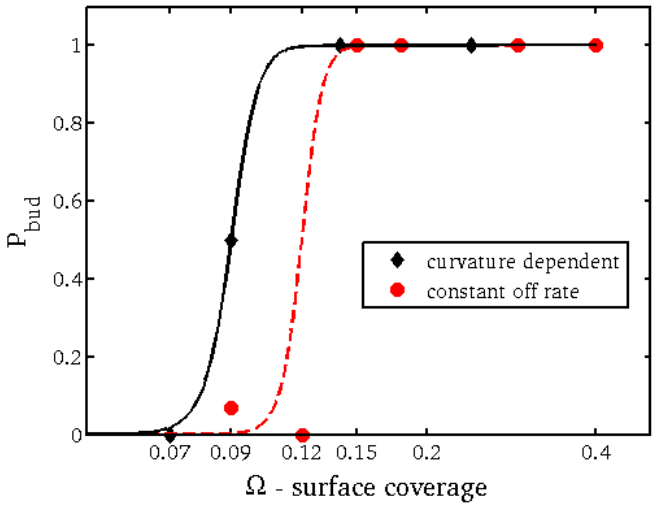

Figure 6.3: *Probability to form a bud P_{bud} within the time course of the simulations (10^8 time steps corresponding to 5s). The probablility for bud formation sharply decreases in the range of $\Omega \approx 0.1$. Please note the semilogarithmic scale.*

For fairly high surface coverages, $\Omega > 0.2$, budding events were observed in all simulations irrespective of a curvature-modulation of the coat dissociation (cf. Fig. 6.3). For very low coverages ($\Omega < 0.05$), no bud formation was found. Both limiting cases are well anticipated. In the intermediate regime, however, modulation of the dissociation rate has a fairly strong effect.
Both models show budding for high surface coverage ($\Omega \geq 0.15$). Then again, in both cases the probability for bud formation drops rapidly for small Ω. In contrast, in the intermediate regime a curvature-sensitive detachment rate proved here to be more efficient in forming buds as compared to a constant detachment rate. However, it should be noted that Ω was subject to comparably large fluctuations.

When considering the sudden drop of both bud formation distributions the current statistics is not sufficient to draw a final conclusion on that matter.

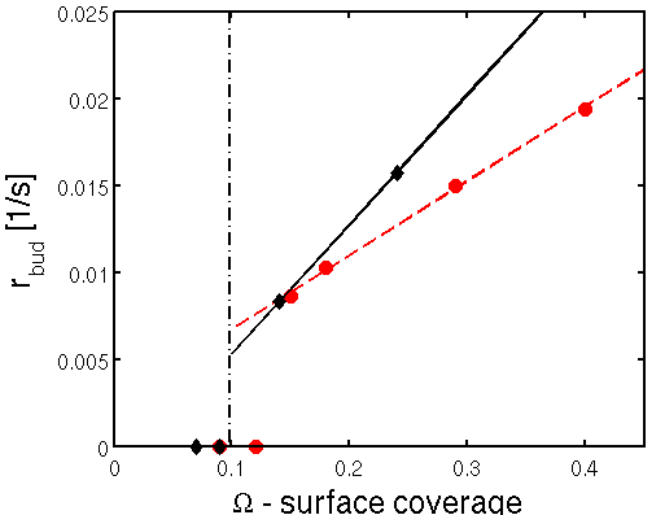

Figure 6.4: *Average budding rate r_{bud} as a function of surface coverage Ω for a constant and a curvature-dependent dissociation rate (circles and diamonds, respectively).*

Above the critical threshold of budformation (i.e. $\mathcal{P}_{\mathrm{bud}} = \infty$), the average budding rate r_{bud} was determined as a function of surface coverage (cf. Fig. 6.4). The budding rates increased together with the surface coverage that is the more coat was attached to the membrane the faster vesicles were produced. Moreover, indication was found that the curvature sensitive mechanism seemed to facilitate more efficient bud formation as compared to an insensitive detachment. In order to elucidate where these difference might originate from, the cluster size distribution (see 6.5) was analyzed for $\Omega = 0.09$ – the point where the bud formation likelihoods differed the most. Snapshots of 15 different simulations after an equilibration time of $t = 10^7\, dt$ were taken. The bin width of the histogram was chosen to be 5 nodes of a cluster's contour length. Finally, the histogram was normalized. In the case of constant detachment rate, clusters of sizes $n \geq 30$ were significantly less likely to form as compared to the curvature-sensitive case.
In order to answer the question of why larger clusters are able to form in the curvature-sensitive case, the lifetimes of the monomeric subunits of each cluster (cf. Fig 6.6) were examined. Specifically, the cumulative lifetime distribution of monomeric subunits were plotted, in other words how likely it is that a coat

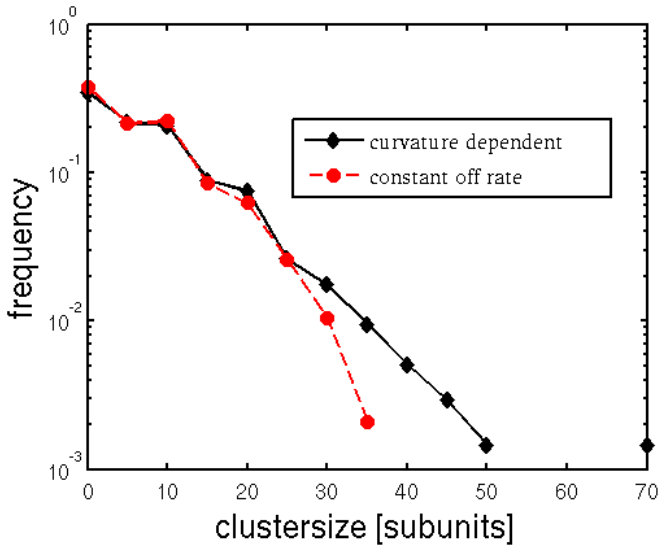

Figure 6.5: *Normalized cluster size distribution measured in coat subunits for a curvature-sensitive and a constant detachment mechanism.*

particle has already detached after a times τ. Detachment after short periods ($\tau \leq 10^6 \Delta t = 50\,ms$) proved to be less likely in the curvature-sensitive case. This resulted in a slight increase of the average lifetime as compared to the case of a constant off-rate. This behavior might be understood by the following consideration. Small clusters hardly give rise to a perturbation in curvature. Consequently, in the curvature-modulated case these clusters will have a small detachment probability. In contrast, in the case with constant detachment rate even small clusters are subject to coat turnover.

6.3 Discussion

Although the formation of coated vesicles has already been investigated by theoretical studies [Foret08], the impacts of a curvature-moulated regulation were not theoretically studied. Since a curvature-sensitive detachment rate introduces intrinsic instability to the budding process, a one-dimensional model based on biological data was formulated to assess whether such a process was feasible in a cellular environment. For comparison, the simplest possible mechanism of detachment is a Poisson process with a constant average detachment rate (similar to radioactive decay) was used. Strikingly, bud formation was not hampered by curvature-sensitivity, but was at least as efficient as the constant detachment mechanism. However, whether a curvature-modulated mechanism performs in-

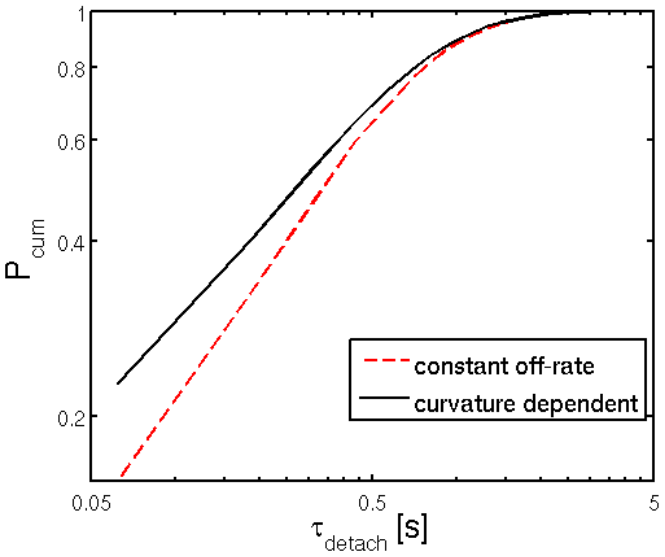

Figure 6.6: *Normalized cumulative lifetime distribution of monomors for constant (blue,solid) and curvature-dependent (dashed,red) off-rate. The coat-surface coverage is* $\Omega = 0.09$*. In the constant case, a higher fraction of coats detached after a very short period (*$< 50\,ms$*), whereas the curvature dependent case showed a higher fraction with intermediate binding times. Comparing the mean monomer lifetimes reveals a slight difference between the two cases:* $\tau_{\mathbf{c-dep}} = (536.5 +/- 9.5)\,ms$ *as opposed to* $\tau_{\mathbf{const}} = (488.5 +/- 9.5)\,ms$*.*

deed better cannot be conclusively decided on the basis of the currently available data.

Still, implications of the underlying mechanism could be elucidated. In the curvature-modulated case small clusters cause only small perturbations in membrane curvature and remain for an extended period on the membrane compared to the constant case. Again, this mechanism helps to form large clusters/buds despite the inherent instability of a curvature-sensitive detachment.

Yet, the presented model was reduced in dimensionality and does not fully reflect the situation of a two-dimensional membrane. In the two-dimensional case, it would be expected that the formation of large clusters is even more favorable. This is because the radius and thus the curvature of a cluster of given size N scales with $\sqrt{N}$. Therefore, the detachment rate of the curvature-modulated case will also scale with $\sqrt{N}$ as compared to a detachment rate of a Poisson process that scales with N. Still, a full two-dimensional representation of the model could provide a better insight into the dynamics of the system. A continuum approach

based on the Helfrich Hamiltonian (cf. Eq. 2.5) could serve as a possible means to address this matter in future work.
Thus far, it was only looked at a linear increase of the curvature-sensitive detachment rate. However, a recent study [Ambroggio10] proposed not only a curvature-sensitive detachment rate but also a threshold of $R \approx 35\mathrm{nm}$ for the recruitment of ArfGAP. This would restrict hydrolysis and thus coat detachment to highly curved regions and lead to an additional stabilization of a growing vesicle bud. Therefore, it would be of interest to include this aspect in further extending the present model.
From a biological point of view, a fast shedding of the COPI coat directly after vesicle production is required to expose v-SNARE proteins to the cytoplasm which are in turn necessary for subsequent vesicle fusion with its target membrane [Spang09]. Therefore, the vesicle coat must be at least partially shed in order to ensure efficient cargo transport. Taken together with the biological benefit of a faster shedding of vesicle coats, these findings suggest how curvature-sensitive detachment mechanisms, despite being intrinsically unstable, can indeed be advantageous for the cell.

Chapter 7

Lipid-induced COPI clustering

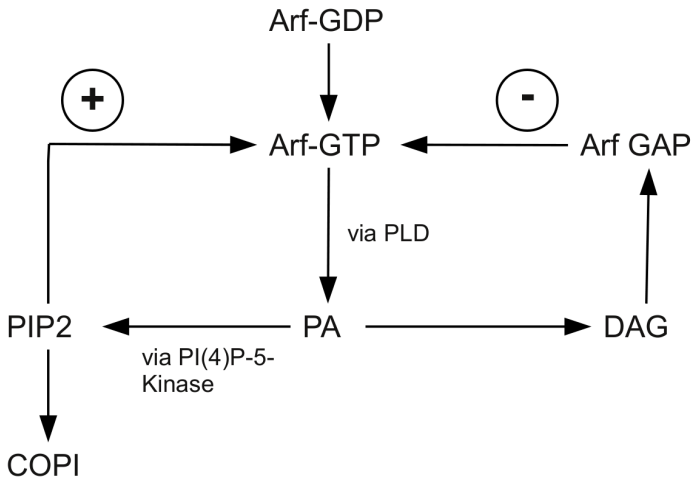

Figure 7.1: *COPI coat components feedback cycle according to Roth et al [Roth99]. Arf1 stimulates PLD to produce phosphatic acid (PA). In turn, PI(4)P-5-kinase produces PIP2 that enhances recruitment of Arf1. However, diacylglycerol (DAG) can be derived from PA and is thought to stimulate ArfGAP binding. Ultimately, ArfGAP induces hydrolysis of Arf1 leading to Arf1 dissociation from the membrane.*

In chapter 6 different detachment mechanisms of the COPI coat were discussed. Here, the focus lies on the attachment and clustering process of COPI, i.e. the initial stages of COPI vesicle formation. The COPI coat formation described in Sec. 3.2.2 accounts only for the minimal set of reaction partners necessary for COPI coat formation, i.e. Arf1-GTP, coatomer and ArfGAP. A recent

study [Manneville08] however showed that COPI coat assembly occurs on liquid-disordered lipid domains within Golgi membranes, hence emphasizing the role of specific lipids in COPI coat formation.
Lipids such as phosphatic acid (PA), diacylglycerol (DAG) and PIP2 seem to play a vital role in COPI vesicle formation [Roth99], cf. Fig. 7.1. While the basic protein components seem to be enough to generate a COPI vesicle, a multi-step procedure that includes lipids is required in biological cells in order to increase budding efficiency [Roth99].
It is not clear why and how vesicle formation should be enhaced in the model proposed by Roth et al [Roth99]. The positive feedback loop in Fig. 7.1 is not sufficient to explain that, because the Arf1 concentration is limited by a negative feedback. One solution to this dilemma could be provided by Turing patterns [Turing52] cf. Chap. 4.
Here, a mathematical model for the formation of COPI domains based on lipid and protein interactions is presented and investigated by the means of computer simulations. Furthermore, the ability to generate spatial COPI patterns is studied for different diffusion scenarios within biological membranes.

7.1 Setting up the model

In this section, a mathmatical model is formulated based on the proposed biological dependencies (cf. Fig. 7.1). An overview of the definitions of lipid/protein concentrations and important gain/loss rates is given in Fig. 7.2.
Depending on Arf1 concentration u PA (x) is produced with an a priori unknown production rate $f(u)$. Similarly, stimulation of the PIP2 production is determined by a function $g(x)$. Arf1 is stimulated again by PIP2 with an unknown rate $p(y)$ that depends on PIP2 concentration y. However, PA can be converted to DAG, giving rise to a linear rate $\Gamma_1 \cdot x$. ArfGAP is recruited to the membrane with an unknown rate $h(z)$ that depends on DAG concentration z. ArfGAP leads to Arf1 dissociation which is reflected by rate $q(v)$ that depends on ArfGAP concentration v.
Neglecting diffusion, a general description of the reaction scheme reads:

$$\partial_t \begin{pmatrix} u \\ x \\ y \\ z \\ v \end{pmatrix} = \begin{pmatrix} p(y) - q(v)u \\ f(u) - \Gamma_1 x \\ g(x) - \Gamma_2 y \\ \Gamma_1 x - \Gamma_3 z \\ h(z) - \Gamma_4 v \end{pmatrix} \tag{7.1}$$

All components are subject to linear degradation except for Arf1 whose dissociation has been shown to depend on ArfGAP. The aforementioned rates

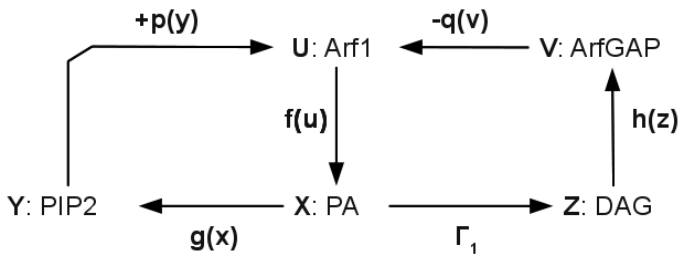

Figure 7.2: *Definition of lipid/protein concentrations and important gain/loss rates. Depending on Arf1 concentration u PA (x) is produced with an apriori unknown production rate $f(u)$. Similarly, stimulation of the PIP2 production is determined by a function $g(x)$. Arf1 is stimulated again by PIP2 with an unknown rate $p(y)$ that depends on PIP2 concentration y. However, PA can be converted to DAG, giving rise to a linear rate $\Gamma_1 \cdot x$. ArfGAP is recruited to the membrane with an unknown rate $h(z)$ that depends on DAG concentration z. ArfGAP leads to Arf1 dissociation which is reflected by rate $q(v)$ that depends on ArfGAP concentration v.*

$$p(y),\ q(v),\ f(u),\ g(x),\ h(z)$$

are not known a priori. Thus, their biological meaning will be discussed in the following to obtain respective mathematical expressions.
Arf-proteins exhibit a so-called pleckstrin homology domain that is known to bind PIP2 ([Martin01]). Moreover, it has been shown that Arf1 binding to membranes depends strongly on PIP2 concentration ([Randazzo97]). PIP2 in turn, seems to accumulate in microdomains [Laux00]. Formation of such a microdomain with subsequent Arf binding requires now that several PIP2 molecules act in concert. Thus, the simplest description of the Arf1 recruitment rate by PIP2 $p(y)$ that is in accordance with these biological requirements is a bimolecular reaction (with rate coefficient c_2) together with a basal attachment rate c_0. Due to the assumption of cooperativity, the linear y-term of the Taylor expansion is neglected:

$$p(y) = \sum_{i=0}^{n} c_i y^i \approx c_0 + c_2 y^2 \tag{7.2}$$

Hydrolysis of GTP by Arf-1 leads to Arf1 unbinding from the membrane. It is reasonable to assume that hydrolysis is mediated in a monomolecular reaction, leading to a linear detachment term in equation 7.1.

$$q(v) = \mu_0 + \mu_1 v \tag{7.3}$$

Here, μ_0, μ_1 are coefficients leading to a linear and an ArfGAP dependend dissociation rate of Arf1.
Arf stimulates phospholipase D (PLD) activity [Brown93] and the hydrolysis of phospholipids by PLD produces phosphatidic acid (PA). Thus, the production of PA might significantly influence lipid composition and surface charge of the membrane [Ktistakis95]. Assuming that the hydrolysis of other phospholipids by PLD is the rate-limiting step, one PLD produces one PA lipid per unit time. This results in a linear relationship between Arf and PA (denoted by x in equation 7.1) with coefficients k_0, k_1.

$$f(u) = k_0 + k_1 u \tag{7.4}$$

In addition, PA can be transformed into diacylglycerol (DAG) via the PA-hydrolase (PAH). Arguing along the same lines as for the production of PA, this leads to a linear loss term for PA, that is equivalent to a linear gain in DAG: $\Gamma_1 x$ (cf. Eq. 7.1). DAG derived from PC has been shown to promote recruitment of the Arf GTPase activating protein (ArfGAP) in vitro [Antonny97]. Similar to the attraction of Arf to the membrane, the assumption of a cooperative DAG lipid action can be made resulting in its simplest form in a quadratic dependency of ArfGAP (denoted as v in equation 7.1) on DAG with coefficents λ_0, λ_2. Due to the assumption of cooperative binding, the linear term of the Taylor expansion can be neglected:

$$h(z) = \sum_{i=0}^{n} \lambda_i z^i \approx \lambda_0 + \lambda_2 z^2 \tag{7.5}$$

Again, a simple linear loss term of ArfGAP is included describing the detachment process from the membrane, which completes the negative feedback cycle.
Continuing the positive feedback loop: PA activates the phosphatidylinositol-4-phosphate kinase [Moritz92], that phosphorylates phosphatidylinositol (PI) and subsequently produces PIP2. Stimulation behavior of the PIP kinase by PA is roughly linear up to a saturation limit [Moritz92]. Hence:

$$g(x) = \sum_{i=0}^{n} \phi_i x^i \approx \phi_0 + \phi_1 x \tag{7.6}$$

with coefficients ϕ_0, ϕ_2. An additional simple loss term accounts for the degradation of PIP2 molecules (cf. 7.1, PIP2 concentration is labelled as y).

Reduction of dimensionality of the system Analytical solutions cannot be obtained easily for this five-dimensional system due to the large parameter space.

Thus, a more manageable description is necessary. To this end, the reaction rates of individual steps will be analyzed to symplify the equation system.
The mean time τ_d to capture an immobile target of radius a in two dimensions with a particle that moves with diffusion coefficient D and which started in a distance b from the target reads [Hardt79]:

$$\tau_d = (b^2/2D)\ln(b/a) \tag{7.7}$$

A single lipid occupies typicaly a surface area of $0.5\,\mathrm{nm} \times 0.5\,\mathrm{nm}$ [Alberts08]. Let us assume for the lipid species under consideration an area fraction of 1%. This yields one lipid of interest in a membrane patch of $5\,\mathrm{nm} \times 5\,\mathrm{nm}$, in other words the typical distance between a lipid and its target enzyme is $b \approx 5\,\mathrm{nm}$. A common value for the radius of a membrane protein is $a \approx 2.5\,\mathrm{nm}$. Hence, the mean time for a lipid to get to a specific enzyme is $\tau_d \approx 8.7 \cdot 10^{-6}\mathrm{s}$. Comparing τ_d to a characteristic reaction time of $\tau_r \approx 10^{-3}\mathrm{s}$ [Alberts08] shows that lipid diffusion can be neglected as compared to lipid reaction rates.
In turn, Arf1 and ArfGAP dynamics can be considered as slow compared to the reaction rate of lipids on the membrane τ_r. Specifically, Arf1 exchange between cytosol and membrane is of the order of seconds as can be deduced from fluorescence recovery after photobleaching (FRAP) measurements [Elsner03]. ArfGAP binding and unbinding has the same kinetics [Elsner03]. Therefore, the formation and degradation of lipids (PA, PIP2, DAG) is fast compared to Arf1 and ArfGAP turnover. Lipid concentration will rapidly adapt to a changes in Arf1/ArfGAP concentration. Hence, a quasi steady state on the time scale of Arf1 dynamics emerges.
Thus, the lipid concentrations for PA, DAG and PIP2 can be approximated by steady state values and do not have to be regarded explicitely. The steady state concentration of PA, x_s, expressed as a function of Arf1 reads as $x_s = 1/\Gamma_1(k_0 + k_1 u)$. Using this relation in the PIP2 dynamics (cf. Eq. 7.1 line 3) leads to

$$\begin{aligned} \Gamma_2 y_s &= \phi_0 + \phi_1 \frac{k_0 + K - 1u}{\Gamma 1} \\ y_s &= \underbrace{\frac{\phi_0}{\Gamma_2} + \frac{\phi_1 k_0}{\Gamma_1 \Gamma_2}}_{\mathrm{const} \equiv \alpha} + \underbrace{\frac{\phi_1 k_1}{\Gamma_1 \Gamma_2}}_{\mathrm{const} \equiv \beta} u \end{aligned} \tag{7.8}$$

and finally to an expression for Arf1 sorted according to powers of u and v:

$$\partial_t u = c_0 + c_2(\alpha + \beta u)^2 - (\mu_0 - \mu_1 v)u \tag{7.9}$$

$$\partial_t u = \underbrace{c_0 + c_2\alpha^2}_{\gamma_0} + \underbrace{(2\alpha\beta - \mu_0)}_{\gamma_1} u + \underbrace{c_2\beta^2}_{\gamma_3} u^2 - \underbrace{\mu_1}_{\gamma_4} vu \quad . \tag{7.10}$$

Employing the same approach for the DAG z (cf. Eq. 7.1 line 4) and Arf-GAP dynamics v (cf. Eq. 7.1 line 5) results in

$$\begin{aligned}
\Gamma_3 z_s &= \Gamma_1 x_s \\
z_s &= \frac{k_0 + k_1 u}{\Gamma 3} \\
\partial_t v &= \lambda_0 + \lambda_1 \left(\frac{k_0 + k_1 u}{\Gamma 3} \right)^2 \\
\partial_t v &= \underbrace{\lambda_0 + \frac{\lambda_1 k_0^2}{\Gamma_3^2}}_{\gamma_4} + \underbrace{\frac{2\lambda_1 k_0 k_1}{\Gamma_3}}_{\gamma_5} u + \underbrace{\frac{\lambda_1 k_1^2}{\Gamma_3^2}}_{\gamma_6} u^2 - \underbrace{\Gamma_4}_{\gamma_7} v
\end{aligned} \tag{7.11}$$

In summary, this reduces the dynamics to two equations with constant coefficients γ_i as defined above.

$$\partial_t u = \gamma_0 + \gamma_1 u + \gamma_2 u^2 - \gamma_3 v u + D_1 \Delta u \tag{7.12}$$

$$\partial_t v = \gamma_4 + \gamma_5 u + \gamma_6 u^2 - \gamma 7 v + D_2 \Delta v \tag{7.13}$$

In general, γ_1 could also adopt negative values, all other coefficients γ_i positive. This system's stability matrix as defined in equation 4.21 reads

$$A = \begin{pmatrix} \gamma_1 + 2\gamma_2 u - \gamma_3 v & -\gamma_3 u \\ \\ \gamma_5 + 2\gamma_6 u & -\gamma_7 \end{pmatrix} \tag{7.14}$$

Since the experimental values of the parameters γ_i, D_i are not known, all observables/quantities were defined in units of the system's characteristic length (r_0) and time scale τ. Because of that not the absolute parameter values, but rather the general behavior of the model are of interest. Hence, the parameter space was explored in order to determine the generic features of the model.

7.2 Parameter space exploration

An automated search routine was developed in order to explore the eight-dimensional parameter space for possible parameter sets, that allow for the formation of spatial patterns. The requirements for such a set were defined by Eq. 4.38 in Chap. 4. An additional requirement for spatial patterns were positive steady state values as these represent chemical concentrations.
Moreover, it is unreasonable to assume diffusion coefficients of membrane proteins that differ much more than one order of magnitude. This behavior can be

understood from the Saffman-Delbrück equation (cf. Eq. 4.3), because diffusion coefficients depend only logarithmic on the radius of membrane proteins. Hence, only parameter sets with a ratio of diffusion coefficients $D_1/D_2 \leq 10$ were considered.

A logarithmically spaced grid was constructed in order to scan a large part of the model's parameter space for possible pattern formation (cf. Tab. 7.2). From the derivation in the previous section it is clear that γ_1 can, in principle, be negative. Thus, γ_1 was allowed to adopt also negative values while other parameters were chosen to be positive. The whole parameter space consisted of 81310472 grid points. A total fraction of 0.493378 % met the requirements for possible spatial pattern formation. This means that the model's Turing space is not a singular point but rather represents a macroscopic volume in parameter space. This analysis suggests that pattern formation in the presented model is a fairly generic phenomenon.

In order to obtain spatial patterns, nonlinear reactions between chemicals must take place. The model indeed possesses two linear terms with corresponding coefficients γ_1 and γ_5. Hence, it was investigated to which extent γ_1 and γ_5 are essential for this model's pattern formation capabilities. To this end, the grid defined above was employed with the restriction $\gamma_1 = \gamma_5 = 0$. This time the total amount of grid points was 531440. In this simplified model an even larger percentage of 1.04414 % of all grid points met the aforementioned criteria for pattern formation.

Although the linear attachement terms γ_1 and γ_5 could be of use for fine-tuning the model, they are not essential for the pattern formation process itself. In general, a reduction of free parameters leads to more generic models. Hence, the model was further simplified by neglecting linear concentration dependent attachment terms ($\gamma_1 = \gamma_5 = 0$) in the following simulations.

Grid A	
$\gamma_0 \in$	$[0.01, 0.1, 0.2, 0.5, 1, 2, 3, 5, 8]$
$\gamma_1 \in$	$[-8, -5, -3, -2, -1, -0.5, -0.2, -0.1, 0, 0.1, 0.2, 0.5, 1, 2, 3, 5, 8]$
$\gamma_2 ... \gamma_7 \in$	$[0, 0.1, 0.2, 0.5, 1, 2, 3, 5, 8]$

Table 7.1: *A logarithmic parameter search grid was employed to test the model's capability to generate spatial domains. Whether a specific set of parameters was able to give rise to spatial patterns was examined via a linear stability analysis.*

7.3 Numerical methods

Numerical results described in this chapter were obtained with standard integration schemes for the partial differential equations. Time integration for a differential equation defined by $\partial_t \mathbf{u} = \mathbf{f}(\mathbf{t}, \mathbf{u})$ was achieved via a fourth order Runge-Kutta scheme:

$$\begin{aligned}
\mathbf{u}(t+\Delta t) &= \mathbf{u}(t) + \frac{1}{6}\Delta t(k_1 + 2k_2 + 2k_3 + k_4) && (7.15)\\
k_1 &= f(t, \mathbf{u}) && (7.16)\\
k_2 &= f(t + \Delta t/2, \mathbf{u}(t) + \Delta t\, k_1/2) && (7.17)\\
k_3 &= f(t + \Delta t/2, \mathbf{u}(t) + \Delta t\, k_2/2) && (7.18)\\
k_4 &= f(t + \Delta t, \mathbf{u}(t) + \Delta t\, k_3) && (7.19)
\end{aligned}$$

Here, unless stated otherwise a time step of $\Delta t = 10^{-4}\tau$ was used. In space, a discretization with a bin width $\delta x = 0.2 r_0$ of the system's natural length scale was chosen. On the basis of a finite differences scheme, the Laplacian operator took the following form in one or two dimensions respectively [Bronstein83] (second order accuracy):

$$\begin{aligned}
\Delta u(x_i, t) = &\ 1/\delta x^2 \left[u(x_{i+1}, t) + u(x_{i-1}, t) - 2u(x_i, t)\right] + \mathcal{O}(\delta x^2) && (7.20)\\
\Delta u(x_{i,j}, t) = &\ 1/\delta x^2 [u(x_{i+1,j}, t) + u(x_{i,j+1}, t) + u(x_{i-1,j}, t)\\
&+ u(x_{i,j-1}, t) - 4u(x_{i,j}, t)] + \mathcal{O}(\delta x^2) && (7.21)
\end{aligned}$$

If not stated otherwise, simulations with 200 lattice sites were performed, resulting in a total system size of $L = 40 r_0$. Periodic boundary conditions were employed. Initially, the system was fluctuating ($\pm 5\%$) around a mean concentration of $u(x_{i,j}, t = 0) \equiv u_0 = 0.1$ (cf. Fig 7.3).
For the following analysis different parameter sets according to table 7.3 were employed.

	D_{crit}	u_0	v_0	γ_0	γ_1	γ_2	γ_3	γ_4	γ_5	γ_6	γ_7
set A	5.72	2.67	2.70	0.1	0	1	1	1	0	1	3
set B	6.31	0.34	0.35	0.01	0	3	3	0	0	3	1

Table 7.2: *Generic parameter sets that were employed to study structure formation processes of the presented model.*

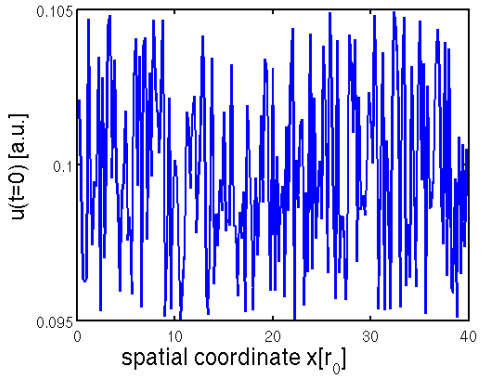

Figure 7.3: *Initial $u_0(x)$, $v_0(x)$ concentrations had a mean value of* 0.1. *A value considerably smaller than the corresponding steady state concentrations (c.f Tab. 7.3). This mean value was perturbed by random spatial fluctuations of* $\pm 5\%$.

7.4 Formation of COPI patterns

The system was initialized with fluctuations ($\pm 5\%$) around mean u, v concentrations that were small compared to the corresponding steady state values (cf. Fig 7.3). Here, u, v denote Arf1 and ArfGAP concentration respectively. In addition, parameter set A was chosen together with diffusion coefficients D_1, $D_2 = 1\, r_0^2/\tau$. From the inital state, Arf concentration (u) increased rapidly as can be seen in Fig. 7.4.
Close to the steady state $u_0 = 2.67$, the system oscillated in time with decreasing amplitude until the steady state was reached after $t \approx 30\tau$. All initial spatial perturbations decayed, resulting in a spatial homogenous pattern.
However, using the same conditions with a diffusion coefficient of ArfGAP (v) $D_2 = 8\, r_0^2/\tau$, a dramatic change in the system's response was detected (cf. Fig. 7.5). During equilibration, the system first approached the homogeneous steady state, u_0. However, before all initial spatial perturbations were smoothed out, spatial inhomogeneities built up with a characteristic wavelength $\lambda \approx 8r_0$. The strength of the spatial inhomogeneities increased in the sense that the pattern's amplitude grew (cf. also Fig. 7.6). At $t = 40\tau$ the system reached a spatially inhomogeneous equilibrium state.
Fig. 7.6 illustrates the temporal dynamics of the absolute values within minimum, maximum and spatially homogeneous u for the simulations above.
A linear stability analysis of this model predicts that above a critical diffusion coefficient $D_2 = 5.72\, r_0^2/\tau$ pattern formation is supported (cf. Tab. 7.3). Although this mathematical approach is an indicator for pattern formation, it does

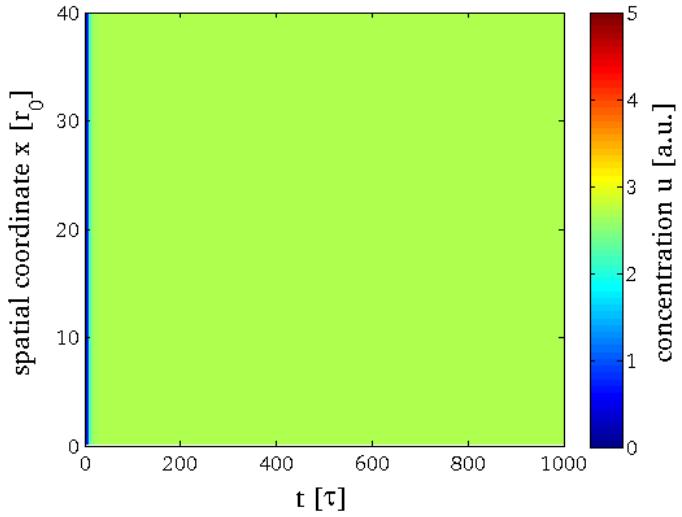

Figure 7.4: *Spatial homogeneous steady state of Arf1. From a random initial configuration, the system approaches a uniform steady state. The concentration of u (color-coded) along its spatial dimension was monitored in time. The numerical simulation was performed with parameter set A and diffusion coefficients* $D_1 = 1r_0^2/\tau$ *and* $D_2 = 1r_0^2/\tau$. *See also Fig.7.6 for a logarithmic representation of the data.*

not necessarily lead to stable spatial patterns.

The numerical simulations shown here confirm that within the simplified model of Arf1/ArfGAP dynamics stable spatial patterns can emerge. However, the emergence of spatial patterns depended crucially on the diffusion coefficients of Arf1 and ArfGAP. Moreover, pattern formation proved to be a robust phenomenon: despite initial concentration far from the steady state concentrations (cf. Fig. 7.3) patterns could emerge.

If patterns do form, how do the relative distribution of Arf1 (u) and ArfGAP (v) look like? As can be seen in Fig. 7.7, the equilibrium concentrations for Arf1 and ArfGAP after $10^4\tau$ showed a colocalization of their peaks. This behavior can be understood when considering that an increase of Arf1 leads to an increase of ArfGAP. Due to the large high diffusion coefficient D_2, ArfGAP spreads fast to neighboring regions. Hence, only a part of the recruited ArfGAP leads to Arf1 detachment. Since Arf1 recruitment is autocatalytic, the increased Arf1 concentration can be maintained.

Similar to [Weiss03a], the maximum absolute value of the Fourier transform of the spatial pattern ξ was defined for modes with $k > 0$. The leading mode ξ

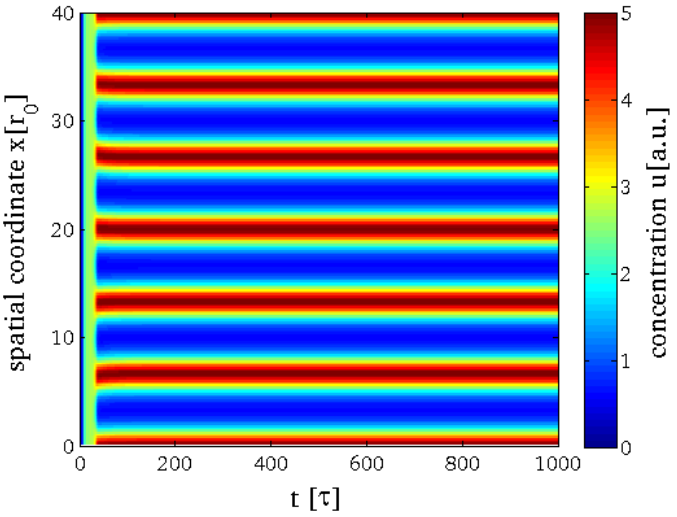

Figure 7.5: *From a random initial configuration close to 0, a spatial concentration pattern evolves in time. The numerical simulation was performed with parameter set A and diffusion coefficients* $D_1 = 1\, r_0^2/\tau$ *and* $D_2 = 8\, r_0^2/\tau$. *See also Fig.7.6 for a logarithmic representation.*

was measured as a function of time for parameter settings that showed pattern formation (parameter set A, $D_2 = 8\, r_0^2/\tau$) and numerical simulations that resulted in spatially uniform distributions (parameter set A, $D_2 = 1\, r_0^2/\tau$). As a result, ξ showed a significant increase at $t = 30\tau$ that coincided with the emergence of spatial patterns (cf. Fig 7.6). In the spatially uniform case ($D_2 = 1\, r_0^2/\tau$) no significant change of ξ could be observed on this scale. Hence, ξ is a useful observable for monitoring the onset of pattern formation.

In the following, ξ was employed to study the influence of diffusion on the pattern formation process. Specifically, the diffusion coefficient of the ArfGAP, D_2, was varied, while the diffusion coefficient of Arf1 was kept constant ($D_1 = 1\, r_0^2/\tau$). For each simulation, ξ was extracted from the corresponding equilibrium configuration (cf. Fig. 7.9). From the linear stability analysis, the critical ratio of diffusion coefficients is predicted to be $D_2/D_1 = 5.72$ (cf. Tab. 7.3). Below this threshold, indeed no signs of pattern formation were observed ($\xi \equiv 0$). Note that already for $D_2 = 5.8\, r_0^2/\tau$, signs of pattern formation were detected ($\xi > 0$) although these are not visible on the scale of Fig. 7.9. A further increase of D_2 lead to a sudden increase of ξ confirming the previously calculated bifurcation point. Patterns became even more pronounced as D_2 increased further, while the pattern's characteristic wave length did not change.

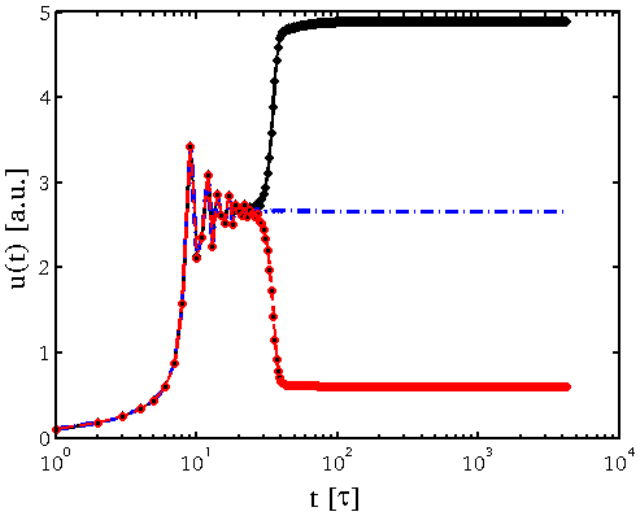

Figure 7.6: *Diffusion-dependent bifurcation of Arf1 concentration. Arf concentration was monitored for a fixed position $x = 0$ in the spatially homogeneous case (dashdots, $D_2 = 1\, r_0^2/\tau$), and for fixed positions ($x = 0, 3.2 r_0$) that corresponded to minimum/maximum concentrations in the pattern forming case ($D_2 = 8\, r_0^2/\tau$). A similar behavior towards the steady state concentration could be observed. At $t \approx 20\tau$ the system showed a diffusion-dependent bifurcation.*

For $D_2 \geq 9\, r_0^2/\tau$, spatial patterns did still form but temporal oscillations of the pattern emerged. To rule out the influence of periodic boundaries, system sizes were increased up to $L = 200$ without noticable effect. These types of pulses are likely not present in biological cells as will be shown in Sec. 7.5 by considering the limited amounts of proteins in the cytosol.

Pattern formation in two dimensions Analyzing structure formation in one dimension is computationally efficient and general principles can be understood in this simplified environment. However, the biological situation to be studied corresponds to a two-dimensional membrane surface. Keeping this in mind, open questions remain to be answered: Does pattern formation work similarly in two dimensions? What do the resulting structures look like?

With conditions that had previously shown pattern formation in one dimension (Parameter set A and $D_1 = 1\, r_0^2/\tau$, $D_2 = 8\, r_0^2/\tau$) simulations were now conducted in two dimensions. As can be seen in the snapshot of Fig. 7.10, a periodic pattern emerged with a characteristic length of roughly $l \approx 7 r_0$. Unlike

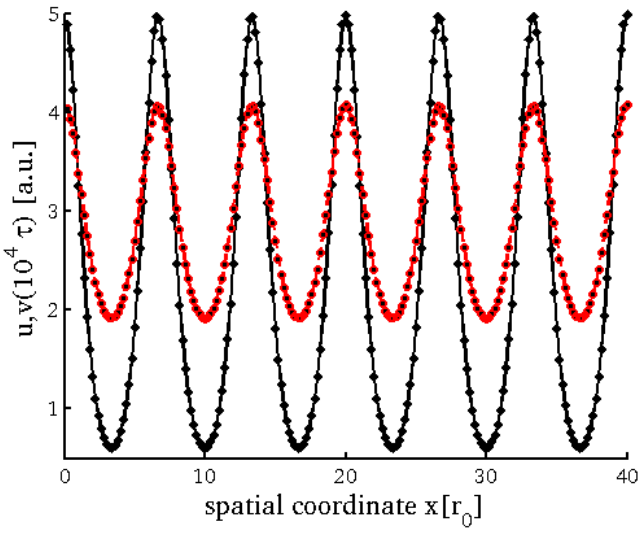

Figure 7.7: *Spatial localization of u (Arf1, solid black) and v (ArfGAP, red dashed) in equilibrium at $t = 10^4\tau$ with $D_1 = 1$ and $D_2 = 8$. Arf1 and ArfGAP showed a spatial colocalization of their peaks. This behavior can be understood when considering that an increase of Arf1 leads to an increase of ArfGAP. Due to the large high diffusion coefficient D_2, ArfGAP spreads fast to neighboring regions. Hence, only a part of the recruited ArfGAP leads to Arf1 detachment. Since Arf1 recruitment is autocatalytic, the increased Arf1 concentration can be maintained.*

other models resulting in stripelike arrangements [Koch94; Reichenbach07], the model showed circular domains. Hence, the model fulfilled the biological requirement to generate circular Arf1-domains since those are required for COPI vesicle production.

Robustness of the integration scheme Next, the model's stability concerning the spatial grid was tested. Test parameter set A was employed together with diffusion coefficents $D_1 = 1\, r_0^2/\tau$ and $D_2 = 8\, r_0^2/\tau$. The system size was fixed to $L = 40 r_0$, and the grid spacing Δx was varied. In Fig. 7.11(a) the observable ξ was utilized to monitor the impact of the grid resolution on pattern formation. When chosing smaller values for Δx (as compared to the standard parameter $\Delta x = 0.2 r_0$) no major changes were observed in the pattern formation process. Similarly, the influence of the system size was tested with parameter set A and diffusion coefficents $D_1 = 1\, r_0^2/\tau$ and $D_2 = 8\, r_0^2/\tau$. Grid size was again set to $\Delta x = 0.2 r_0$. Again ξ was employed to monitor the system's response (c.f Fig.

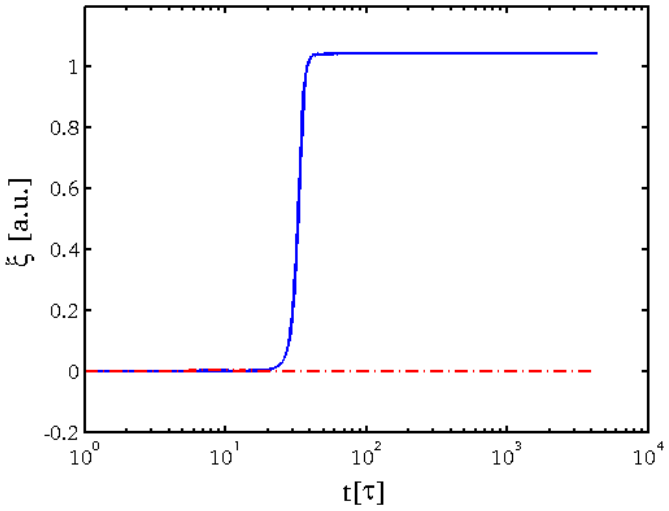

Figure 7.8: *The leading mode ξ as observable for spatial pattern formation. The maximum absolute value of the Fourier transform of the spatial pattern, ξ, was determined for numerical simulations with parameter set A, $D_2 = 1$ (red dashdots) and $D_2 = 8$ (solid blue line), respectively. The leading mode ξ was measured as a function of time t for modes with $k > 0$. ξ increases significantly at $t = 30\tau$ - the same time patterns start to develop (cf. Fig 7.6). In the spatially uniform case ($D_2 = 1$) no significant change of ξ can be observed on this scale.*

7.11(b)). Unless the system size approached the wave length of the dominant mode $L \approx 7r_0$, no major impact on the bifurcation behavior was observed. Although pattern formation was still possible when the system size approached the pattern wavelength, the dynamics of the bifurcation was dramatically slowed down together with a reduction of amplitude of the resulting pattern. Thus, equilibrium values of ξ were determined at $t = 10^3\tau$ for the slowly evolving systems.
Summarizing, it can be said that system size did not significantly influence the model's response if the chosen system size was larger than the wave length associated with the pattern formation process.

7.5 Influence of the cytosol

Although this generic model yielded already insights into possible COPI clustering processes on membranes, it corresponds rather to a crude approximation.

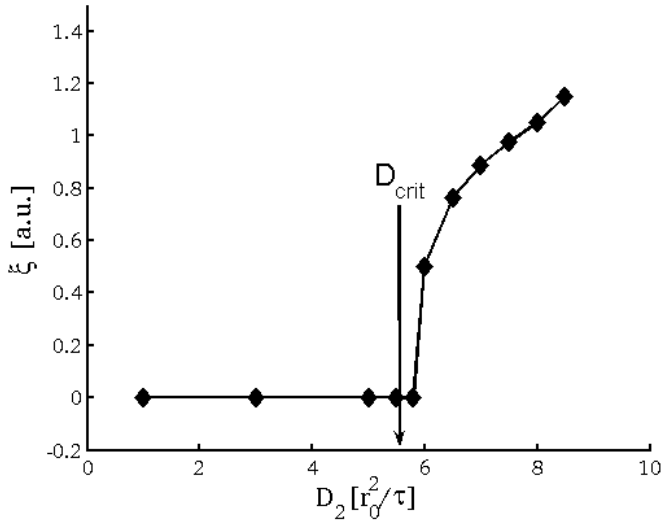

Figure 7.9: *The leading mode ξ, a measure for spatial pattern formation, was monitored for numerical simulations with varying diffusion coefficient D_2. No traces of pattern formation were observed below the theoretically predicted bifurcation point $D_c = 5.72$. Above D_c, stable spatial patterns with increasing amplitude were observed.*

Under physiological conditions more factors have to be taken into account. New proteins that bind to the membrane are recruited from the cytosol. So far, it was assumed, that the cytosol was well mixed and held unlimited amounts of proteins. Taking that as a starting point the model could be expanded in a straight-forward manner. Cytosolic concentrations of Arf1, ArfGAP were explicitely simulated (denoted as u_{cyto}, v_{cyto} respectively). The cytosol was described as a two-dimensional layer above the membrane with initial large reservoir sizes of $u_{\mathrm{cyto}}(0) = 10\, u_0$ and $v_{\mathrm{cyto}}(0) = 10\, v_0$, compared to the steady state concentrations on the membrane u_0, v_0. Protein diffusion in the cytoplasm is typically faster $\mathcal{O}(10\mu m^2/s)$ than on membranes $\mathcal{O}(1\mu m^2/s)$ crowding induced subdiffusion in the cytoplasm could significantly slow down D_{cyto}.

When considering mass conservation the total amount of Arf1 and ArfGAP has to remain constant. Therefore, in the existing set of equations all gain/loss terms on the membrane had to be balanced by loss/gain terms in the cytosol:

$$\partial_t u_{\mathrm{cyto}} = -\gamma_0' u_{\mathrm{cyto}} - \gamma_2' u_{\mathrm{cyto}}\, u^2 + \gamma_3\, vu + D_{\mathrm{cyto}} \Delta u_{\mathrm{cyto}} \tag{7.22}$$

$$\partial_t v_{\mathrm{cyto}} = -\gamma_4' v_{\mathrm{cyto}} - \gamma_6' v_{\mathrm{cyto}} u^2 + \gamma_7 v + D_{\mathrm{cyto}} \Delta v_{\mathrm{cyto}} \tag{7.23}$$

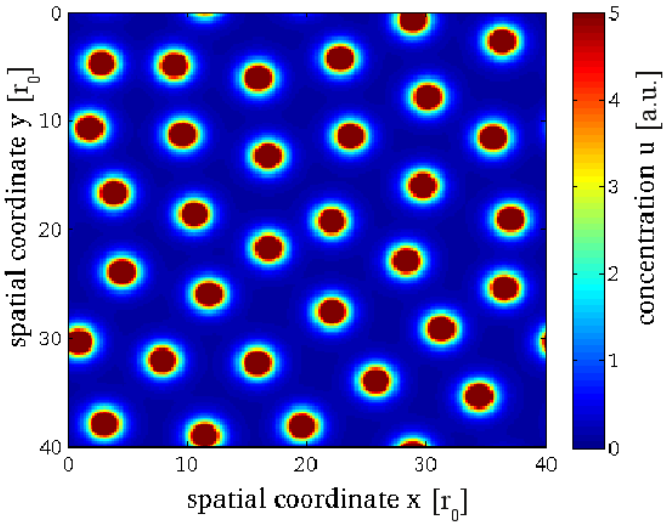

Figure 7.10: *Snapshot after* $5 \cdot 10^2\,\tau$ *time steps of a two-dimensional numerical simulation with parameter set A and diffusion coefficients* $D_1 = 1\,r_0^2/\tau$ *and* $D_2 = 8\,r_0^2/\tau$*. Stable spatial domains emerge and are arranged in a periodic fashion.*

with the following definitions:

$$\gamma_0' \equiv \gamma_0/9u_0, \quad \gamma_2' \equiv \gamma_2/9u_0, \quad \gamma_4' \equiv \gamma_4/9v_0, \quad \gamma_6' \equiv \gamma_6/9v_0, \tag{7.24}$$

Here, all γ_i' were defined in such a way that the same spatially homogeneous equilibrium states u_0, v_0 emerged and the previous results are recovered in the extended model. This becomes obvious when considering that $u_{\mathrm{cyto}} = 9u_0$ if a quantity $1\,u_0$ is localized on the membrane in equilibrium. As pointed out earlier, γ_1 and γ_5 were not essential for the pattern formation process and consequently were set to zero. Therefore, the corresponding terms were not considered in Eq. 7.22.

In a first simulation the resulting steady states were tested. The obtained steady state concentrations were $u_0 = 2.67$ and $v_0 = 2.72$. This matches well the theoretical predictions (cf. Tab 7.3). The deviation of 1% might easily be explained by the non-empty initial state of the membrane ($u(0)$, $v(0) > 0$) that slightly increased the total amount of u, v in this closed system.

As reported above, for $D_2 \geq 10\,r_0^2/\tau$ temporal oscillating patterns were observed. Here it was tested whether mass conservation stabilizes these patterns. Numerical simulations were conducted under the same conditions as before, but effects of the cytoplasm were considered. Cytoplasmic diffusion was set to $D_{\mathrm{cyto}} = 10\,r_0^2/\tau$.

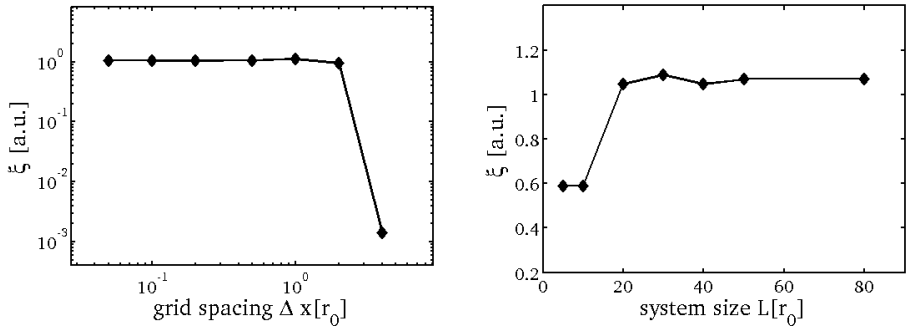

Figure 7.11: *Influence of the grid spacing/system size on pattern formation. The absolute value of the leading mode, ξ, was chosen as observable for pattern formation. Numerical simulation with parameter set A and diffusion coefficients $D_1 = 1\, r_0^2/\tau$ and $D_2 = 8\, r_0^2/\tau$ were conducted. Pattern formation is relatively robust concerning grid spacing. The employed standard grid spacing $\Delta x = 0.2 r_0$ is well in the regime of numerical stability.*

Effectively, two new parameters were introduced by considering the cytoplasm explicitely, i.e. the cytoplasmic diffusion coefficient D_{cyto} and the cytoplasmic pool sizes. The impact of these two parameters on pattern formation was studied (cf. Fig. 7.14) with the standard set of pattern parameters (parameter set A, $D_1 = 1\, r_0^2/\tau$, $D_2 = 8\, r_0^2/\tau$). In all studied cases, stable patterns formed in the extended model as well. Interestingly, a smaller cytoplasmic pool increased the strength of the pattern which is defined in this context as the ratio of the pattern's amplitude over mean concentration.

Similarly, a decrease of the cytoplasmic diffusion coefficient lead as well to slightly stronger pattern formation. When D_{cyto} adopted values comparable to D_1, D_2 the characteristic wavelength of the pattern changed, because then D_{cyto} became a limiting factor in the pattern formation process.

Both cases can be understood by the following analysis. A maximum in Arf1 results also in a maximum of ArfGAP. Since substance ArfGAP spreads faster, it possesses a broader peak as compared to Arf1. The detachment rate of ArfGAP depends on its amount that is present on the membrane. Since there are fairly high amounts of ArfGAP in all regions, there will also be a large flux of ArfGAP from 'non-peaked' regions on the membrane to the cytosol. In turn, cytosolic ArfGAP will be slightly depleted in regions with Arf1/ArfGAP concentration peaks on the membrane. Again, a depletion of cytosolic v leads to a smaller flux of v in the 'peak regions'. Since membrane-bound ArfGAP is required for the detachment of Arf1, the concentration of u in the peak region will effectively

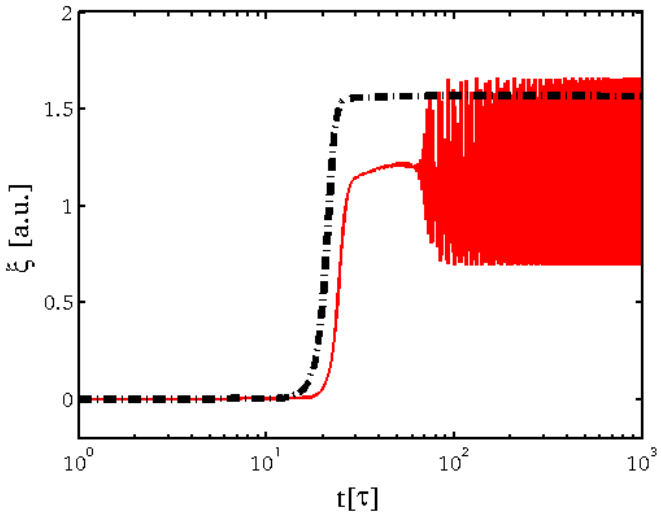

Figure 7.12: *Increased stability of the model by introducing mass conservation. Numerical simulations were set up with parameter set A and* $D_1 = 1\, r_0^2/\tau$, $D_2 = 10\, r_0^2/\tau$. *Without mass conservation, the leading mode* ξ, *a measure for pattern formation, showed temporal oscillations (red line) that were also observed in the corresponding pattern. In contrast, no temporal oscillation of the pattern was detected when mass conservation was introduced by explicitely simulating protein amounts in the cytoplasm with* $D_{cyto} = 10\, r_0^2/\tau$ *(black dashes).*

increase, giving rise to a larger amplitude of the pattern. A decrease in D_{cyto} as well as a decrease of the cytosolic pool size will enhance the described ArfGAP depletion effect, it thus enhances pattern formation. The depletion effect and the anticyclic variations between cytosolic and membrane bound concentrations are depicted in Fig. 7.13.

As expected, an increase of D_{cyto} was observed to smear out differences in the cytoplasm (data not shown). This explains how the case of an infinitely well-mixed protein pool can be recovered as a limiting case of this extended model.

In summary, it can be stated that although the incorporation of cytosolic exchange added extra parameters to the system, the previous observations were already generic in the sense that in a typical parameter regime the system showed similar structure formation. Unexpectedly, the effect of a finite protein pool leads to an increase in pattern amplitude that is equivalent to an increased Arf1 cluster formation. In addition, particle conservation leads to an increased stability of the whole reaction diffusion system, because it introduces effectively a bounding domain, i.e. a region in the model's concentration space that cannot be ex-

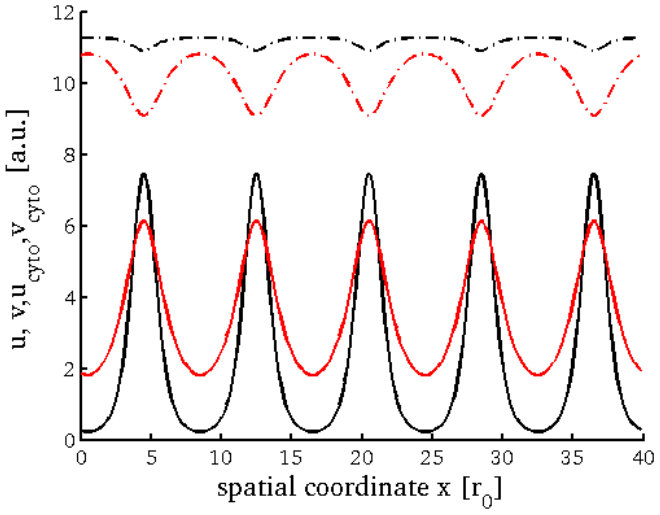

Figure 7.13: *Cytosolic depletion of Arf1/ArfGAP colocalized with increased Arf1/ArfGAP concentrations on the membrane. Numerical simulations were conducted with parameter set A,* $D_1 = 1\, r_0^2/\tau$, $D_2 = 8\, r_0^2/\tau$, $D_{cyto} = 20\, r_0^2/\tau$. *The sizes of cytosolic protein pools were set to* $5u_0$, $5v_0$ *for u (Arf1) and v (ArfGAP) respectively. The protein distributions of membrane-bound Arf1 (solid black), cytosolic Arf1 (black dashes), membrane bound ArfGAP (solid red) and cytosolic ArfGAP (red dahes), are depicted after an equilibration period of* $1000\,\tau$. *The shown depletion effect enhanced pattern formation (cf. Fig. 7.14).*

ceeded/where the system is trapped. This is especially important when dealing with subdiffusion, cf. Sec. 7.7.

7.6 Subdiffusion and Porous Media Equation

When studying anomalous diffusion in macroscopic systems, the porous media equation (PME) provides an adequate tool to describe the spreading of a particle concentration u since it features a nonlinear growth of the mean squared displacement $\propto t^\alpha$ with the anomaly index $\alpha \neq 1$ [Abe05; Vazquez]. The PME reads in d dimensions as follows,

$$\partial_t u = D\,\Delta u^\beta, \qquad \beta > 1 \tag{7.25}$$

$$\alpha = \frac{2}{d\,(\beta - 1) + 2} \tag{7.26}$$

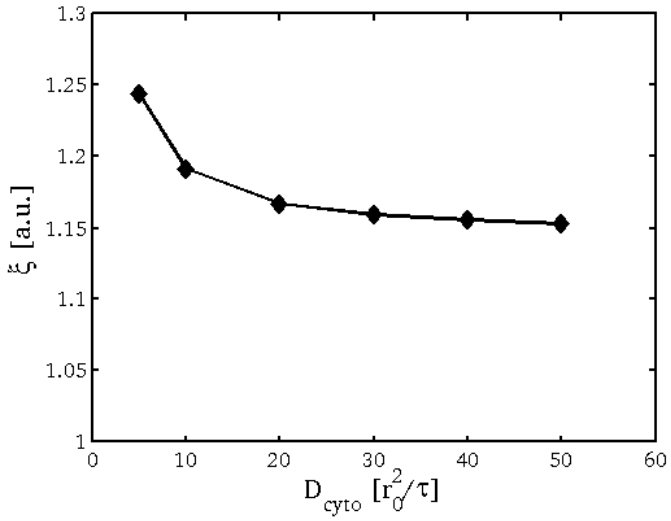

Figure 7.14: *Enhanced pattern formation due to slow cytosolic diffusion. Numerical simulations were conducted with parameter set A and $D_1 = 1\, r_0^2/\tau$, $D_2 = 8\, r_0^2/\tau$, while the cytoplasmic diffusion coefficient D_{cyto} was varied. Again, the leading mode ξ was employed as pattern formation observable. Slow cytosolic diffusion enhanced the cytoplasmic deplection effect (see text), thus it increased Arf1 clustering.*

The exponent β determines the degree of nonlinearity of this partial differential equation. Moreover, the PME's exponent β and the degree of anomalous diffusion α are directly related (Eq. 7.26). In the following, the porous media equation is utilized to simulate reaction-diffusion models with subdiffusive characteristics.

In order to test the predicted diffusional spreading, the numerical integration setup presented previously in Sec.7.3 was employed. The mean square displacement was studied for different values of β (Fig.7.15). Fitting the anomaly coefficient α to the MSD data, validates the relation $\alpha(\beta)$ (Eq. 7.26).

By comparing the concentration profiles of normal and anomalous diffusion with similar MSD, it became quite obvious that the curves are fundamentally different (cf. Fig. 7.16). An initial δ-peak evolved into a Gaussian profile due to normal diffusion. However, when simulating subdiffusion by means of the PME the propagator showed non-Gaussian properties: it rather looked like a parabola with relatively sharp boundaries.

Usually, when doing a linear stability analysis of a reaction-diffusion system, the Laplace operator can be simplified as described in chapter 4. However, the situation becomes more complicated when studying subdiffusion in such a system,

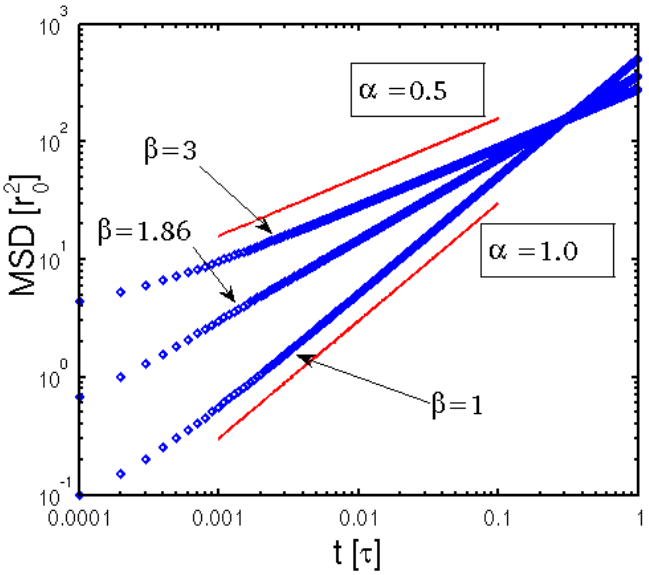

Figure 7.15: *Mean square displacement (MSD) for normal diffusion and anomalous diffusion was simulated by the porous media equation 7.26 (PME) with exponents $\beta = 1.86$ and $\beta = 3$. Anomalous diffusion characteristics with a MSD $\propto t^{\alpha}$ was well described by the PME. Moreover, the relation between the anomaly index α and the exponent of the PME was validated (Eq. 7.26).*

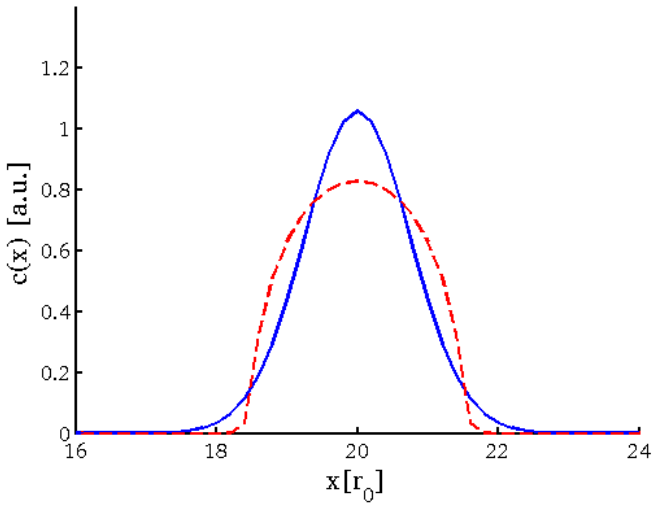

Figure 7.16: *Concentration profiles for normal and anomalous diffusion after $t \approx 0.3\tau$ with a δ-peak like initial condition. Althought the two profiles have roughly the same width, the shape of the curves is very different.*

because the PME is highly nonlinear. Close to a steady state of particle species u the diffusion term $\Delta u^\beta, \quad \beta > 1$ of the PME can be approximated in the following way:

$$\begin{aligned}\partial_{x_i}^2 \left(u_0+\epsilon\right)^\beta &= \partial_{x_i}\left(\beta\left(u_0+\epsilon\right)^{\beta-1}\partial_{x_i}\epsilon\right)\\ &= \underbrace{\beta\left(\beta-1\right)\left(u_0+\epsilon\right)^{\beta-2}\left(\partial_{x_i}\epsilon\right)^2}_{O(\epsilon^2)} + \underbrace{\beta\left(u_0+\epsilon\right)^{\beta-1}\left(\partial_{x_i}^2\epsilon\right)}_{\beta u_0^{\beta-1}\left(\partial_{x_i}^2\epsilon\right)}\end{aligned}$$

The constant $\beta u_0^{\beta-1}$ effectively increases the diffusion coefficient. Thus, it was adsorbed into a generalized diffusion coefficient D^*. In the linear stability analysis (cf. Eq. 4.38) one has to substitute D by the generalized diffusion coefficient D^*. Furthermore, solving the last expression in Eq. 4.38 for D_2^* leads to the requirement

$$D_2^* > D_1^* D_{\text{crit}} \tag{7.27}$$

$$D_2\beta_2 v_0^{\beta_2-1} > D_1\beta_1 u_0^{\beta_1-1} D_{\text{crit}} \tag{7.28}$$

where D_{crit} is a constant that depends on the model's parameters and the indices $1, 2$ refer to species u, v respectively. This suggests that the requirement of

strongly differing diffusion coefficients for pattern formation between two particle species u, v could be relaxed via subdiffusion. If the inhibitor v is subdiffusive with $\beta_2 > 1$ and $v_0 > 1$, while the actor u is normal diffusive $\beta_1 = 1$, this results in $D_2 \beta_2 v_0^{\beta_2 - 1} > D_1 D_{\mathrm{crit}}$. Hence, the diffusional barrier for the spatial pattern formation can be overcome more easily. The same effect can in principle be generated, if the activator u is subdiffusive. To this end, its steady state value has to fulfill $u_0 < 1$ so that $\beta_1 u_0^{\beta_1 - 1} < 1$.

7.7 Subdiffusion and pattern formation

Recent studies point towards the possiblity, that diffusion within biological membranes is anomalous due to their heterogeneous structure [Ratto03]. Moreover, the formation of Turing patterns requires typically strongly varying diffusion coefficients. It has been shown that subdiffusion requires less strong differences in (non-generalized) diffusion coefficients and that this may facilitate pattern formation by requiring smaller ratios D_2/D_1 [Weiss03a].
Here, the possible influence of subdiffusion on COPI domain formation was studied by employing the porous media equation (PME) 7.26. In order to ensure stability of the numerical integration the simulation's time step was decreased to $\Delta t = 10^{-5}\tau$ due to the nonlinearity of the PME. Again, the cytosol was considered explicitely as described above with a size of the cytoplasmic protein pools of $10\, u_0$, v_0, respectively and a diffusion coefficient $D_{\mathrm{cyto}} = 10\, r_0^2/\tau$.

Subdiffusion of Arf1 enhances pattern formation By inspecting equation 7.28 one can see that the critical threshold above which structure formation is possible, D_{crit}, could be effectively lowered in a system with steady state $u_0 < 1$ when choosing $\beta > 1$. Thus, numerical simulations were set up with parameter set B ($u_0 = 0.35$, $v_0 = 0.35$) and $D_1 = 1\, r_0^2/\tau$, $D_2 = 3\, r_0^2/\tau$ (cf. Fig. 7.17(a)). Although the ratio of diffusion coefficients was $D_2/D_1 < D_{\mathrm{crit}}$, $D_{\mathrm{crit}} = 6.31\, r_0^2/\tau$, stable spatial structures emerged in the simulations.
From equation 7.28 one would predict that in principle slowing down Arf1 (u) via subdiffusion could result equally to speeding up ArfGAP (v) result in pattern formation. However, when studying the effects of anomalous diffusion, one has to take into account that depending on the time scale anomalous diffusion can either lead to faster or slower spreading compared to normal diffusion (cf. Fig. 7.15). This time point is termed crossover time t_{co}. In Fig. 7.15 it can be seen that $t_{\mathrm{co}} \approx 0.3\,\tau$. Hence, subdiffusion is slowed down on a length scale of $0.55 r_0 \approx 3\Delta x$ as compared to normal diffusion (with $D = 1\, r_0^2/\tau$). Summarizing, slowing down Arf1 via subdiffusion can enhance pattern formation by decreasing the 'effective diffusion coefficient' $D_1^* \equiv D_1 \beta\, u_0^{\beta - 1}$ (cf.Eq. 7.28).

Structural differences arise from subdiffusion In the following, the effective diffusion coefficient D_1^* was employed as a metric for comparing normal and anomalous diffusion. A comparative simulation with normal diffusion $D_1 = 1\, r_0^2/\tau$, $D_2 = 8.16\, r_0^2/\tau$ was conducted (because the previous simulation setting gave rise to $D_2/D_1^* = 8.16$). Firstly, the observed wavelength (cf. Fig. 7.17(b)) was significantly shorter compared to the normal diffusive case because the minima in u were narrower. Secondly, the drop in concentration around an Arf1 maximum was much more pronounced.

The structural differences of the patterns can be understood by considering that Arf1 is significantly slowed down after the crossover time τ_{co}. That leads to a sudden drop in Arf1 concentration. The net attachment flux of the ArfGAP in peak regions has to be balanced by a net ArfGAP detachment flux in regions of low Arf1 concentrations. Since the drop in Arf1 is very abrupt that means there exists a sink of ArfGAP close to its source causing a large concentration gradient. According to Fick's first law $\vec{J} = -D\nabla C$ the concentration gradient in ArfGAP gives rise to a large ArfGAP flux on the membrane from maximum to minimum regions, hence supporting the formation of spatial patterns with smaller wavelengths. This finding suggests that anomalous diffusion is not just another possibility to facilitate pattern formation, but can give rise to different pattern structures.

Influence of the anomality index on pattern formation In the following, it was systematically investigated, how the anomaly index α influences stucture formation. As seen earlier (cf. Fig. 7.15) there exists a direct relation between the anomaly index α and the exponent β of the porous media equation $\alpha = 2/(\beta+1)$ for one dimension. Thus α was modulated by varying the exponent β. Again ξ was employed as an indicator for pattern formation. Please note that the absolute values of ξ cannot directly be compared for different sets of parameters, hence only relative changes within a specific setup are compared subsequently.

As α increased, ξ dropped at $\alpha \approx 0.54$ by roughly one order of magnitude (cf. Fig. 7.18(a)). From Eq. 7.28 one predicts a critical anomaly index $\alpha_{\mathrm{crit}} \approx 0.55$ as a threshold for pattern formation. This prediction agrees well with the observed drop in ξ in the graph. For $\alpha > 0.56$ no traces of pattern formation could be observed.

From the structure of equation 7.28 one would predict that subdiffusion of the inhibitor could as well lead to structure formation below a threshold of α. This is surprising as the formation of Turing patterns requires 'fast' diffusion of the inhibitor v (ArfGAP) and subdiffusion typically results in a slower spreading compared to normal diffusion.

It was tested under which circumstances a subdiffusive inhibitor/ArfGAP can

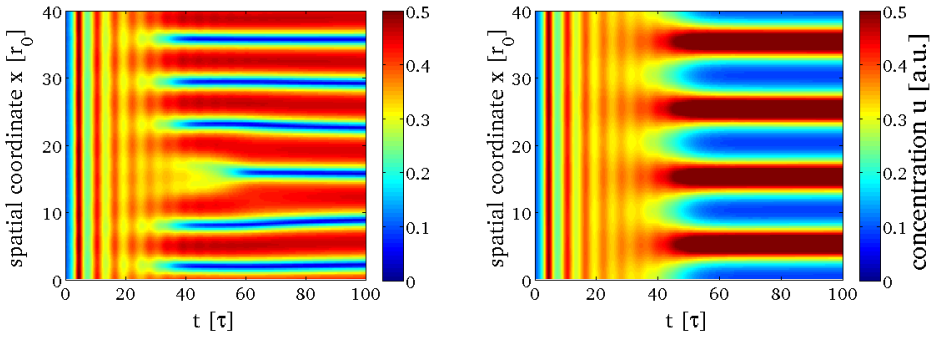

Figure 7.17: *Differences in pattern structure between anomalous and normal diffusion. a) Pattern formation with subdiffusive Arf1 (u) ($\alpha = 0.5$). Arf1 concentration on the membrane as a function of time and space. A numerical simulation was conducted with parameter set B ($u_0 = 0.35$, $v_0 = 0.35$, $D_{crit} = 6.3\, r_0^2/\tau$) and $D_1 = 1\, r_0^2/\tau$, $D_2 = 3\, r_0^2/\tau$. After a short oscillation period, the system approached its steady state. Despite the ratio of diffusion coefficients being $D_2/D_1 < D_{crit}$, stable spatial structures formed as a result of subdiffusion. b) Pattern formation with $D_1 = 1\, r_0^2/\tau$, $D_2 = 8.16\, r_0^2/\tau$. According to Eq. 7.28 the effective ratio diffusion coefficents were comparable to case a). Despite that, the structure of the pattern looked significantly different. Most prominently, the pattern's wavelength of the normal diffusive case was almost doubled compared to the subdiffusive case.*

give rise to structure formation. To this end, parameter set A was used; diffusion coefficients were set to $D_1 = 1\, r_0^2/\tau$, $D_2 = 1\, r_0^2/\tau$. Again, ξ was monitored as the anomality α, respectively β, was varied. Similarly to the observation above, patterns formed for $\alpha < \alpha_{\text{crit}} \approx 0.65$ (cf. Fig. 7.18(b)). This phenomenon has to be considered in terms of a finite crossover times: due to the nature of the PME a change in the anomaly α can increase the local spreading of ArfGAP (on a time scale smaller than the crossover time).

Summarizing, the anomaly index α affects the effective diffusion coefficient D^* according to Eq. 7.28. The value of α_{crit} found here agrees well with this predicitions. In other words, a larger anomaly index α can enhance pattern formation by, e.g., effectively slowing down the spreading of Arf1.

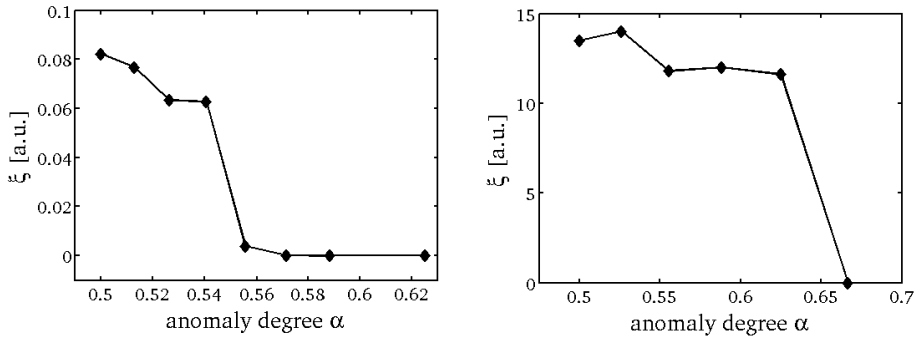

Figure 7.18: *The degree of subdiffusion α affects pattern formation. The leading mode ξ, a measure for spatial pattern formation, was monitored for numerical simulations with variations of the exponent β of the porous media equation 7.26 (that is directly related to the anomality coefficient α). a) Numerical simulations were conducted with parameter set B and $D_1 = 1\, r_0^2/\tau$, $D_2 = 3\, r_0^2/\tau$. The spreading of activator Arf1 was subdiffusive. Above a critical threshold $\alpha \approx 0.56$ no stable spatial patterns were observed. b) Numerical simulations were conducted with parameter set A and $D_1 = 1\, r_0^2/\tau$, $D_2 = 1\, r_0^2/\tau$ and subdiffusive spreading of ArfGAP. Again, a major impact of the anomaly α on pattern formation was observed: a sharp transition in ξ at $\alpha \approx 0.65$ marked the onset of pattern formation.*

7.8 Discussion

Here, a mathematical model was formulated that captures the influence of lipids, i.e. Pip2, PA and DAG, on Arf1 and ArfGAP association to the membrane. It was shown that the model possesses properties that can lead to the formation of spatial patterns. Arf1 is a core component in COPI vesicle formation. Hence, the presented structure formation process can be regarded as a possible first step of vesicle production. Other components, such as the coatomer complex, could then bind to this 'template pattern' and lead to the actual production of COPI vesicles. Supporting this view, a recent study [Manneville08] showed that recruitment of Arf1 occured mainly at specific, disordered lipid domains. Despite the insight gained from this reaction-diffusion model, it provided only one step along the understanding of intracellular vesicle formation. For future extensions of this model one would need to consider effects such as curvature-sensitive Arf1 hydrolyzation (cf. Chap. 6) or lipid phase separation in heterogeneous membranes [Schmidt10].

In the cellular cytoplasm the amount of proteins is limited. Moreover, diffusion within the cytoplasm is thought to be subdiffusive [Weiss04]. Hence, the cytosol is most likely not well mixed and inhomogeneities in the cytoplasm might play a role in the association/dissociation cycle of Arf1/ArfGAP respectively. In order to shed light on the influences of these phenomena, the set of equations was extended to capture mass conservation and diffusion within the cytoplasm. Strikingly, depletion effects within the cytosol enhanced pattern formation in the sense that the pattern's amplitude increased.
Most probably not only diffusion within the cytoplasm [Weiss04] but also diffusion within heterogeneous cellular membranes is anomalous [Ratto03; Weiss03b]. Owing to these observations, there is a growing interest in studying the effects of subdiffusion on pattern formation in reaction-diffusion systems. A recent study [Weiss03a] for instance employed a particle based approach to study subdiffusion in the well-known Schnakenberg model.
Here, the porous media equation as a non-particle based approach was employed to study the impact of subdiffusion on the derived COPI reaction scheme. In agreement with previous findings [Weiss03a], subdiffusion was observed to assist the pattern formation process. Moreover, subdiffusion was found to be capable of changing the morphology of patterns.
In order to maintain the formed structures on the membrane, 'futile' on/off cycles are required which give rise to protein fluxes to/from the membrane. Indeed, rapid turnover of ArfGAP has been detected on cellular membranes [Elsner03; Liu05]. However, one could ask whether COPI coat polymerization with a single irreversible binding step would be more efficient. Non-hydrolyzable Arf1-GTP analogues were employed in a study by Lanoix and colleagues [Lanoix99]. In this case Arf1 cannot be hydrolyzed any more, membrane-bound COPI components cannot dissociate again. Indeed, COPI vesicles could still form under these conditions, but vesicles were found to be depleted of cargo. However, vesicular transport requires the selection of the right cargo. A single irreversible binding step of coat components would lead though to a high amount of wrongly selected cargo [Weiss03c]. Hence the on/off cycles of Arf1 and ArfGAP might actually support the cargo selection process. Although the minimum machinery for COPI vesicle has been proposed to consist of Arf1-GTP and coatomer [Spang98], the efficiency of vesicle production was found to increase in the presence of acidic phospholipids. Taken together, these findings can be reconciled with the presented model: Without preexisting structures, coatomer will attach to membrane-bound Arf1. Arf1-coatomer complexes diffuse on the membrane and polymerize upon collisions. Thus vesicle budding will take considerably longer compared to the case when coatomer attaches to a well-localized binding environment/pattern. Thus, the presented model helps to explain how intracellular COPI vesicle production could efficiently be steered.

In order to test the model's validity, one could for instance employ an approach similar to Manneville et al [Manneville08] by monitoring lipid composition and COPI coat formation simultaneously. In addition, one needs to develop an *in vitro* essay to measure COPI vesicle production as a function of concentration of different lipids such as Pip2, DAG and PA and their main regulatory proteins such as phospholipadase D and the PI(4)P-5 kinase. In particular, by addition or removal of ArfGAP such a system should undergo a transition where Arf1 should suddenly become localized to specific lipid domains.

Chapter 8

Physical properties of lipid bilayers on the nanoscale

In the course of this thesis it has been shown how membrane structures or structures within membranes can emerge in biological cells. However, the intrinsic properties of membranes can influence pattern formation processes. We will look now more closely at particular lipid material properties that are important for structure formation. Dissipative particle dynamics (DPD) has proven to be a versatile simulation technique for studying membrane-related processes on the micron scale and therefore it will be employed in the following to investigate membrane material properties.

Lipid mixtures have been shown to phase-separate under the influence of external curvature [Yoon06; Parthasarathy06]. The free energy of the system can be minimized if soft/stiff lipids colocalize with regions of high/low curvature respectively. In a current study [Mercker11] it is shown that the phase separation process of soft and rigid lipids on curved substrates is largely determined by the exact dependence of the membrane stiffness on lipid composition. Here, the membrane stiffness as a function of concentration of stiff/soft lipids was studied with DPD as part of a larger study [Mercker11] and it was shown to have a profound effect on curvature-induced sorting/domain formation.

In the second part, the motion of single lipids is under consideration. In general, homogeneous lipid membranes were thought to resemble two-dimensional fluids [Singer72]. A recent study [Harland10] suggested lipid subdiffusion within homogeneous artificial membranes challenging existing data. Here, their hypothesis is tested by means of DPD. In particular, we aim at reaching experimentally accessible timescales. As a result, we report normal diffusion within the time scales of the simulation.

8.1 Dissipative Particle Dynamics

Dissipative particle dynamics (DPD) is a versatile simulation technique. It is particularly well suited to study the behaviour of lipid membranes, because systems sizes up to 100 nm and time scales in the microsecond range are accessible by this technique, while retaining a resolution on the level of single lipid molecules. Therefore, this method has been employed to study various membrane-related processes such as lipid phase separation [Laradji04; Laradji05; Kranenburg03], self-assembly of lipid vesicles [Yamamoto02] and vesicle budding [Yamamoto03]. Atoms or groups of atoms are represented by beads with mass m_i. A single bead is subject to the sum of pairwise-additive conservative, dissipative and random forces exerted by its neighbors within a cutoff distance r_0. The dissipative force takes into account that upon collision of two particles some energy is lost to interal degrees of freedom. The random force equilibrates the energy loss caused by the dissipative force and thus keeps the system from freezing. The time evolution of the beads is governed by Newtons equation of motion.
Basically, the DPD setup introduced by Schmidt et al. [Schmidt08] was employed. The cutoff r_0, together with all bead masses and the thermostat temperature were set to unity.
In order to ensure computational efficiency, short-ranged potentials were employed. A linear repulsive force was employed for any two particles i,j that were within a cutoff distance $r_{ij} = |\mathbf{r}_{ij}| = |\mathbf{r}_i - |\mathbf{r}_j \leq r_0$:

$$\mathbf{F}_{ij}^C = a_{ij}(1 - r_{ij}/r_0)\mathbf{e}_{ij} \tag{8.1}$$

Here $\mathbf{e}_{ij} = \mathbf{r}_{ij}/r_{ij}$ denotes the unit vector, whereas a_{ij} defines interaction energies between different types of particles. This force represents the excluded volume effects.
Our simulation setup consisted of three types of beads: water (W), hydrophilic lipid headgroup beads (H) and hydrophobic lipid tail beads (T). By varying a_{ij} the degree of hydrophobicity was be modified. Values for the repusion constant were chosen similar to [Laradji04]: $a_{HT} = a_{WT} = 200k_BT/r_0$ and $a_{WW} = a_{HH} = a_{TT} = a_{WH} = 25k_BT/r_0$.
In order to construct whole lipids, beads were tied together via Hookean springs with equilibrium separation distance $l_0 = 0.45r_0$ and a spring constant of $k = 100k_BT/r_0^2$:

$$U(\mathbf{r}_i, \mathbf{r}_{i+1}) = k(r_{i,i+1} - l_0)^2/2 \tag{8.2}$$

To introduce an intrinsic stiffness, a three-body bending potential between consecutive beads $i-1$, i, $i+1$ was included:

$$V_{\mathrm{b}}\left(\mathbf{r}_{i-1}, \mathbf{r}_i, \mathbf{r}_{i+1}\right) = \kappa_{A/B}\left(1 - \cos\left(\Phi\right)\right) \tag{8.3}$$

$$\cos\left(\Phi\right) = \mathbf{e}_{i,i-1} \cdot \mathbf{e}_{i,i+1} \tag{8.4}$$

In this specific setup, lipids were represented as linear chains (HT_3). Moreover, two types of lipids were considered with differing intrinsic stiffness $\kappa_A = 10$, $\kappa_B = 30$.
Since dissipative and random force balance the temperature, this set of forces is referred to as thermostat. Dissipative force $\mathbf{F}_i^D j$ and random force $\mathbf{F}_i^R j$ act on particles within the cutoff distance $r_{ij} \leq r_0$.

$$\mathbf{F}_{ij}^D = -\gamma_{ij}(1 - r_{ij}/r_0)^2(\mathbf{e}_{ij} \cdot \mathbf{v}_{ij})\,\mathbf{e}_{ij} \tag{8.5}$$

$$\mathbf{F}_{ij}^R = \sigma_{ij}(1 - r_{ij}/r_0)\xi_{ij}\mathbf{e}_{ij} \tag{8.6}$$

Here, $\mathbf{v}_{ij} = \mathbf{v}_i - \mathbf{v}_j$ denotes the relative velocity between particle i and j. In addition, ξ_{ij} defines a random variable with zero mean $\langle \xi_{ij} \rangle = 0$ and unity variance $\langle \xi_{ij}\xi_{kl} \rangle = \delta_{ik}\delta_{kl}$. Random and dissipative force obey the fluctuation dissipation theorem [Español95]. By requiring

$$\sigma_{ij}^2 = 2\gamma_{ij}k_B T \tag{8.7}$$

it could be shown that the correct NVT ensemble is simulated. A typical choice of parameters that fulfills this requirement is $\sigma_{ij} = 3$, $\gamma_{ij} = 9/2$.
A Velocity-Verlet algorithm was chosen for integrating the equations of motions, due to its increased stability compared to Euler's method. The DPD Velocity Verlet scheme comprised the following steps [Nikunen03].

1. Calculate velocities $\mathbf{v}_i \leftarrow \mathbf{v}_i + (\mathbf{F}_i^C \Delta t + \mathbf{F}_i^D \Delta t + \mathbf{F}_i^R \sqrt{\Delta t})/2m$
2. Update positions $\mathbf{x}_i \leftarrow +\mathbf{v}_i \Delta t$
3. Calculate all forces $\mathbf{F}_i^T = \sum_{i \neq j}^N (\mathbf{F}_{ij}^C + \mathbf{F}_{ij}^D + \mathbf{F}_{ij}^R)$
4. Calculate velocities
   - $\mathbf{v}_i^0 \leftarrow \mathbf{v}_i + (\mathbf{F}_i^C \Delta t + \mathbf{F}_i^R \sqrt{\Delta t})/2m$
   - $\mathbf{v}_i \leftarrow \mathbf{v}_i^0 + \mathbf{F}_i^D \Delta t/2m$
5. Update dissipative force $\mathbf{F}_i^D$
6. Calculate physical quantities of interest

The time increment of the Velocity Verlet scheme was chosen to be $\Delta t = 0.01$. The simulation box was set up with periodic boundary conditions. Membrane patches of size $25r_0 \times 25r_0$ spanning the simulation box were relaxed via a barostat [Jakobsen05a] by adjusting the box size. The relaxation procedure was applied for $2{\cdot}10^5$ time steps. After this period, the membrane was found to be in a tensionless state. For the remaining 10^6 time steps the size of the simulation box was held constant. Intrinsic DPD units can be converted to SI units. Comparison of the typical membrane thickness of $d = 4nm$ to our simulation, yields $r_0 = 1nm$. An equivalent gauging of the time step can be derived from the lipid diffusion coefficient yielding $\Delta t \equiv 80ps$ [Jakobsen05b].

8.2 Composition dependence of the membrane bending stiffness

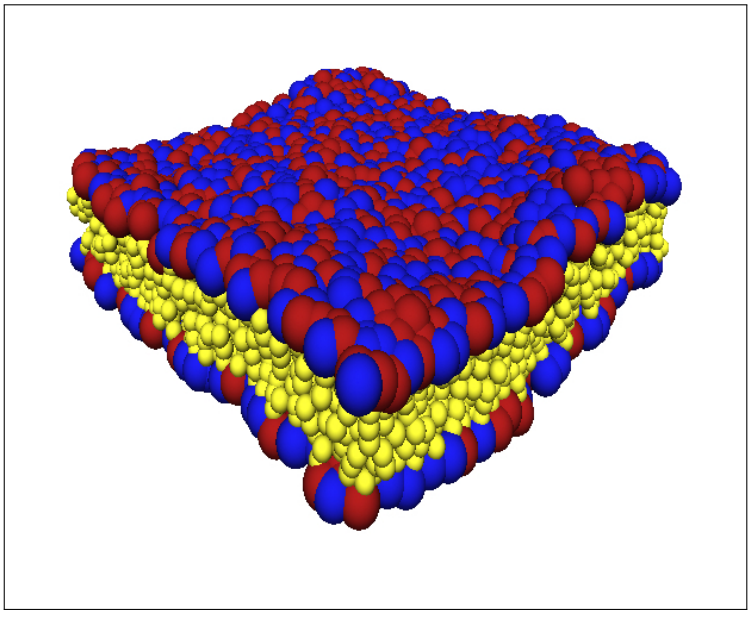

Figure 8.1: *Typical DPD simulation snapshot with* $\langle\phi\rangle = 0$, *i.e.* 50% *lipid A and lipid B respectively. The size of the patch corresponds to* $25nm \times 25nm$ *by converting intrinsic DPD units to SI units. The simulation setup produced stable fluctuating membranes in a tensionless state. Blue and red spheres indicate lipid headgroups corresponding to lipids of type A, B respectively and hydrophobic lipid chains are depicted in yellow (water not shown).*

Previous DPD studies on binary lipid mixtures focused mainly on phase separation [Kranenburg03; Laradji04; Laradji05] or the influence of lipid length differences on

membrane stiffness [Illya06; Imparato05]. Here, DPD simulations were employed to parameterize the detailed relationship between the mechanical moduli κ and the average local composition ϕ for the macroscopic continuum model. To do so, a locally well-mixed system was considered, and DPD was used to directly measure the bending stiffness from the fluctuation spectrum of the bilayer surface in Fourier space. Since the Gaussian bending rigidity κ_G cannot be directly measured [Siegel04], we restricted the analysis to the bending modulus κ. A representative snapshot is shown in Fig. 8.2.
Helfrich theory [Seifert97] predicts a relationship between wave vector $\vec{q}$, the bending modulus κ and the lateral tension η of the following form (a derivation can also be found in Sec. 2.2):

$$\langle |h_{\mathbf{q}}^2| \rangle = \frac{k_B T}{L^2 \left(\kappa q^4 + \eta q^2\right)}. \tag{8.8}$$

Due to the relaxation of membrane tension as described above, $\eta = 0$ can be assumed in Eq. 8.8. Fitting this equation to the averaged Fourier spectrum of our simulations (see Fig. 8.2) yielded the bending stiffness of a single simulation. We varied the concentration ratio between the lipid species with bending stiffnesses κ_A^{DPD} and κ_A^{DPD} stepwise by 10%.
In order to minimize the error in the measurement of the bending stiffness, a statistical approach was employed by running 10 simulations for each parameter set. For each of these simulation sets, the average bending stiffness and the corresponding standard error of the mean were determined (Fig. 8.3).
As more soft lipids were present in the membrane, the overall membrane stiffness decreased monotonically. The results show that adding few soft lipids to a majority of very stiff lipids hardly leads to any perturbation of the bending stiffness. Since the shape of the curve is symmetrical, the same holds true for a small concentration of stiff lipids that are surrounded by a soft lipids. However, exceeding a certain threshold of stiffer/softer lipids in a sea softer/stiffer lipids leads to significant changes of the overall bending stiffness.

8.3 Discussion

In the study of Mercker et al [Mercker11] it was shown that the dynamics towards the equilibrium and the equilibrium state itself depend crucially on the function $\kappa(\phi)$. Here, DPD was used to elucidate the bending stiffness concentration dependence of binary lipid mixtures $\kappa(\phi)$. Specifically, lipids of the same length and properties except a difference of the lipid's chain bending rigidity were studied. That might correspond to a situation with flexible poly-cis unsaturated membranes and stiffer saturated/monounsaturated phosphatidylcholine (PC) lipids

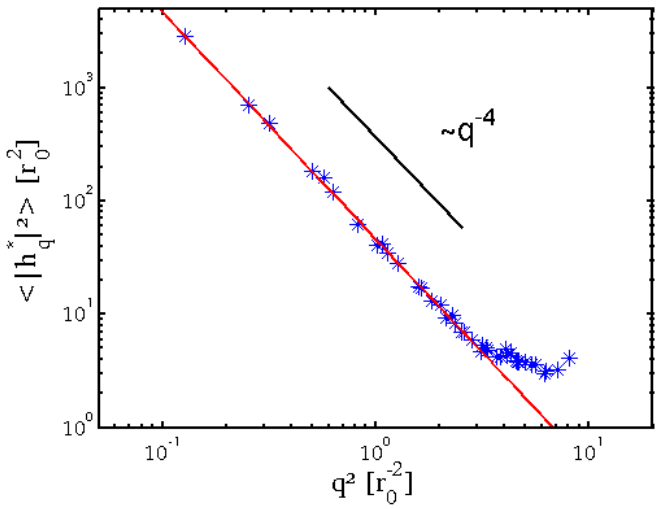

Figure 8.2: *Fluctuation spectrum of the membrane surface plotted as function of wavenumbers q (symbols). According to Eq. (8.8) the fluctuation spectrum of tensionless membranes is $\propto q^{-4}$ and a fit (red line) to that equation yielded the bending stiffness of the membrane κ. The fluctuation spectrum was well described by Eq. 8.8. However, for large q^2 the spectrum is governed by protrusions of single lipids – a regime Eq.8.8 is not applicable any more, since it is derived from continuum theory.*

[Rawicz00]. Furthermore, this case is of special interest for the finite element simultions, because the calculation of the free energy requires a microscopically well-mixed system.

For this system, it was found that the bending stiffness of a rigid membrane varies only weakly after the addition of small amounts of softer lipids. In contrast, for intermediate lipid concentrations, the bending stiffness varies strongly. Again, for high amounts of stiff lipids the effect of lipid concentration is weak which results roughly in a symmetrical $\tanh(\phi)$ curve.

Previous theoretical [Szleifer88] and simulation approaches [Illya06; Brannigan05] concentrated mainly on two different scenarios. Homogeneous lipid mixtures with a difference in hydrocarbon chainlength showed a non-monotonic asymmetric $\kappa(\phi)$ curves. Then again, nonhomogeneous lipid mixtures lead to different asymmetric $\kappa(\phi)$ shapes.

Summarizing, different lipid models result in different functions for $\kappa(\phi)$ that do not need to exclude, but rather complement each other. That means the interplay of lipids with different geometries can lead to various different composition dependencies of the bending stiffness. Moreover, it was shown here that exact

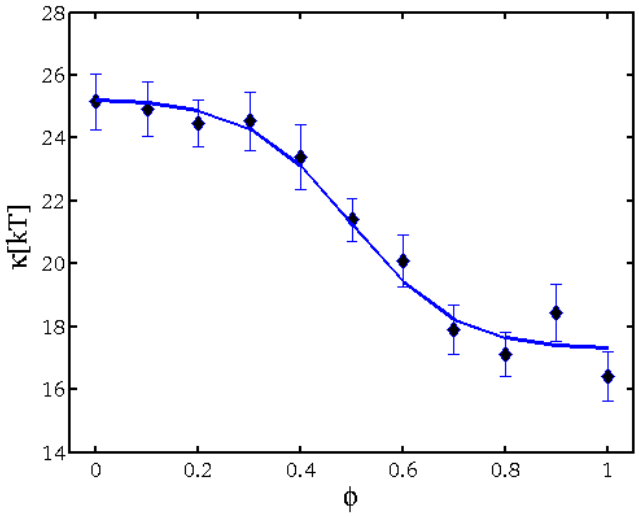

Figure 8.3: *Macroscopic membrane bending stiffness κ as a function of concentration ϕ. $\phi = -1$, $\phi = 1$ correspond to pure membranes with stiff lipid B and soft lipid A, respectively. Intrinsic DPD stiffness of lipid A and B are set to $\kappa^{DPD}_{A/B} = 10, 30 k_b T$, respectively. Each data point corresponds to the mean value of 10 simulations with the according standard error of the mean. As less stiff lipids are present, the stiffness of the whole membrane κ decreases monotonically. While κ is barely affected by small changes in lipid concentration compared to a pure membrane, intermediate concentrations affect κ dramatically. A fit of the form $a + b\tanh(-c\phi)$ with $a = 21.3$, $b = 4.0$ and $c = 2.5$ serves as a guide to the eye. Please note that the bending stiffness of the lipid chain κ^{DPD} is not equivalent to κ.*

form of this relationship is important for lipid phase separation. Taken together, this provides a tool how biological cells might utilize the bending stiffnesse's composition dependence of different lipids to fine-tune structure formation processes on their membranes.

8.4 Are lipid membranes viscous?

In a recent study Harland and colleagues [Harland10] applied particle-tracking microrheology to freestanding phospholipid bilayers - so called black lipid membranes. Their claim was that instead of being viscous, lipid bilayers provide a viscoelastic environment. In particular, they analyzed the mean squared displacement of fluorescent beads that were attached to lipids with the membrane. By following the elegant approach by Mason and Weitz [Mason95], viscoelastic ma-

terial properties were extracted from the MSD. However, they detected nonlinear MSDs implying that diffusion within homomgeneous membranes is anomalous. Applying the evaluation procedure by Mason and Weitz for anomalous diffusion [Guigas07] results in the detection of a viscoelastic material property as we will see below. Thus, anomalous diffusion and viscoelasticity are closely related.
So far, FRAP and FCS studies performed on lipid diffusion in artificial homogeneous membranes such as giant unilamellar vesicles [Korlach99; Kahya03], and supported lipid bilayers [Benda06; Jönsson08; Horton10], have reported normal lipid diffusion. Therefore, the findings by Harland et al [Harland10] seem to be at odds with previous work. However, in most systems anomalous diffusion becomes normal at certain length and time scales [Guigas07]. DPD simulations can access fairly large times scales up to the millisecond range. Thus, this method can be used to shed light on the question whether diffusion of lipids in homogeneous membranes is normal or anomalous. Before coming to the investigation of lipid diffusion, let us briefly review how anomalous diffusion is connected to viscoelasticity.

Connection between anomalous diffusion and viscoelasticity Mathematically, viscoelasticity is represented by the complex shear modulus

$$G(\omega) = G'(\omega) + iG''(\omega) \qquad . \tag{8.9}$$

Here, the real part $G'(\omega)$ represents the elastic and the imaginary part $G''(\omega)$ denotes the viscous part where ω denotes frequency. The Laplace transform $\tilde{v}(i\omega)$ of the mean square displacement $v(t)$ of an anomalously diffusing particle reads [Guigas07]

$$v(t) \propto t^{\alpha} \tag{8.10}$$

$$\tilde{v}(z) = \int_0^{\infty} e^{-zt} v(t) dt \tag{8.11}$$

$$\tilde{v}(i\omega) \propto \Gamma(\alpha+1)/(i\omega)^{\alpha+1} \tag{8.12}$$

The Mason-Weitz approach yields a relationship between the complex shear modulus $G(\omega)$ and the Laplace transform $\tilde{v}(i\omega)$ of a diffusing particle of radius R:

$$G(\omega) = \frac{k_B T}{i\pi\omega R\tilde{v}(i\omega)} \tag{8.13}$$

Combining Eqs. 8.12 and 8.13 yields for normal diffusion, i.e. $\alpha = 1$, $G(\omega) \propto i\omega$ suggests a purely viscous environment. For $\alpha \neq 1$ a factor $i^{-(2+\alpha)} \equiv i^{\gamma}$ occurs.

The Euler relation for the imaginary unit shows how this factor gives rise to a real (elastic) and an imaginary (viscous) part of $G(\omega)$:

$$i^{\gamma} = e^{i\pi\gamma/2} = \cos(\pi\gamma/2) + i\sin(\pi\gamma/2) \tag{8.14}$$

This analysis of the Mason-Weitz approach shows how anomalous diffusion gives rise to viscoelastic properties and vice versa.

Data acquisition Aiming at the experimental time scales of Harland and coworkers, DPD simulations with for $2 \cdot 10^7\,\Delta t$ were carried out with initial boxsizes of $L_x = L_y = 15\,r_0$ and $L_z = 10\,r_0$. Before starting the simulation, the membrane was equilibrated with the barostat for $10^5\Delta t$. The headgroups of 100 randomly selected lipids were tracked. Every 100th timestep ($\widehat{=}1\,\tau$) the excursion pathlength was saved. Five simulations were carried out for two different cases: floppy lipids with stiffnesses $\kappa_A^{\mathrm{DPD}} = 10 k_b T$ and more rigid lipids with $\kappa_A^{\mathrm{DPD}} = 30 k_b T$ were employed.
Two different methods were used to evaluate the lipids' MSDs. From all lipid headgroups i the ensemble average of the MSD $\langle v(t)\rangle_N$ was calculated according to

$$\langle v(t)\rangle_N = \frac{1}{N}\sum_{i=1}^{N}\left(\mathbf{x}_i(t) - \mathbf{x}_i(0)\right)^2 \tag{8.15}$$

where $N = 500$ denotes the total amount of beads taken into account.
Additionally, the time-averaged MSD $\langle v(\tau)\rangle_T$ for each trajectory was calculated separately:

$$\langle v(\tau)\rangle_T = \frac{1}{T-\tau}\sum_{j,t_j=0}^{T-\tau}\left(\mathbf{x}_i(t_j+\tau) - \mathbf{x}_i(t_j)\right)^2 \tag{8.16}$$

8.5 Lipid diffusion characteristics

Long-term simulations with $2\cdot 10^7\Delta t$ were set up in order to reveal possible deviations from normal diffusion. Even a slightly nonlinear growth of the MSD should give rise to a significant effect in measurements that comprise a time period of several decades. Moreover, by extending our simulations to the millisecond scale the lower end of the experimental time scales with typical framerates of $200/s$ [Harland10] could be reached.
The ensemble average of the lipid's mean squared displacement of four different simulations is shown in Fig. 8.4. The MSD was fitted with normal diffusion. At the lower end of the time scale ($t \approx 100\Delta t$) slight deviations from a linear

behavior were detected. This effect was only significant up to $t \approx 200\Delta t$. Most probably, on length scales smaller than r_0 lipids have not sampled their environment properly and thus move in a slightly ballistic manner due to the action of the thermostat.
On larger time scales ($10^3 - 10^7\Delta t$) the MSD was perfectly described by a linear increase. This finding suggests that homogeneous lipid bilayers constitute a viscous environment with normal instead of anomalous lipid diffusion. The diffusion coefficient was fitted by taking into account that the MSD of Brownian motion in two dimensions increases as follows $\langle \Delta x^2 \rangle = 4Dt$. That yielded $D = (3.50 + / - 0.25)\, 10^{-2} r_0^2/\tau$. This diffusion coefficient can be employed to independently verify the gauging of this setup's time step increment of $\Delta t \equiv 80ps$ as postulated by Jacobsen et al [Jakobsen05b]. Experminental data suggest a typical lipid diffusion coefficient of $D_{\exp} = 4\mu m^2/s$ [Korlach99]. Identifying this value with the diffusion coefficient found in the presented simulations yielded $\Delta t = 87.5ps$ which is in fair agreement with the value found by [Jakobsen05b].

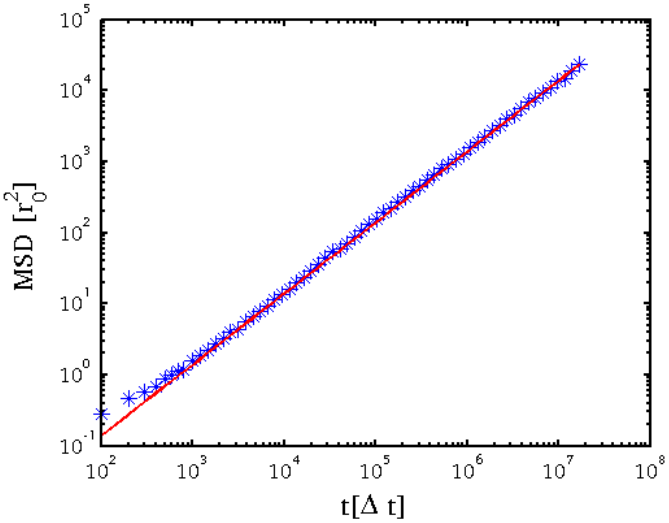

Figure 8.4: *Lipid mean squared displacement within a bilayer. The lipid stiffness was chosen to be $\kappa^{DPD} = 10k_bT$. The presented mean squared displacement was derived from an ensemble 400 trajectories from four independent simulations. Simulations ran for $T = 2 \cdot 10^7\Delta t$ accessing the millisecond range ($T \approx 1.6\, ms$). A linear fit of the MSD described the data well.*

In addition, the lipid's time-averaged MSD was monitored as independent verification. The maximum lag time was restricted to $\tau_{\text{lag}} = 2 \cdot 10^6\Delta t$ in order to obtain sufficiently good statistics. By fitting the MSD for 400 trajectories a distribution of measured diffusion coefficients was acquired (cf. Fig.8.5). The

mean and standard error of the mean were determined from this distribution $D = (3.79 +/- 0.01)\,10^{-2} r_0^2/\tau$. Unlike anomalous diffusion in the continuous time random walk, normal diffusion does not lead to a breaking of ergodicity. Hence, time and ensemble average of the diffusion coefficients are expected to be equal. Although, the measured ensemble mean does not perfectly coincide with the peak in Fig. 8.5, it is well within the distribution of diffusion coefficients hence providing an independent verification of the measured diffusion coefficient.

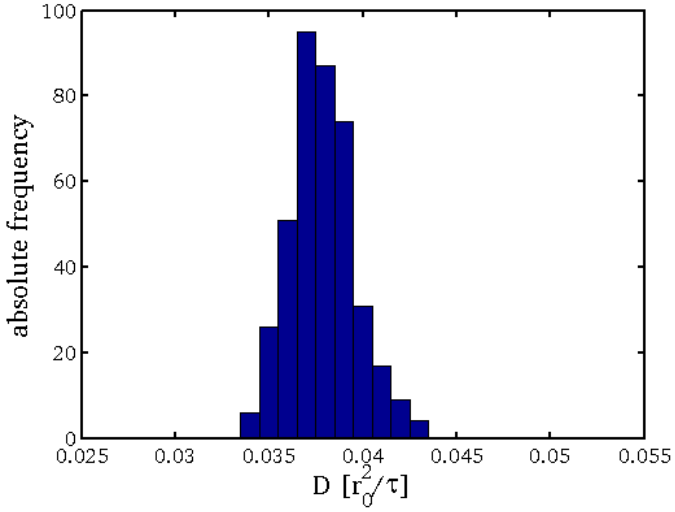

Figure 8.5: *Histogram of lipid diffusion coefficients obtained by the time-averaged MSD of 400 individual trajectories. The diffusion coefficient was determined within the two dimensional plane of the lipid membrane. The lipid stiffness was set to $\kappa^{DPD} = 10 k_b T$. The mean diffusion coefficient determined from this histogram was $D = (3.79 +/- 0.01)\,10^{-2} r_0^2/\tau$. The ensemble average of $D = (3.50 +/- 0.25)\,10^{-2} r_0^2/\tau$ is well within the peak of this distribution.*

8.6 Discussion

With a time step $\Delta t = 80ps$ our DPD setup could measure the mean squared displacement up to $t \approx 1.6ms$. The measurements by Harland et al [Harland10] suggest that diffusion becomes more and more anomalous at the lower end of their observation times ($\mathcal{O}(10ms)$). Although the two time scales do not directly overlap, the strongly anomalous diffusion should already be measurable at the upper end of the simulation time scale. In contrast to the findings by Harland et al, no signs of anomalous diffusion were detected on any of the time scales.

As can be seen in Fig. 8.4, lipids covered on average a distance of $100r_0$. That exceeds the size of our system ($L = 15r_0$). Hence, the position of lipids' are 'folded back' into our simulation box as a result of the periodic boundary conditions. One might argue now that either as a result of the small system size or due to the influence of the periodic boundaries diffusion might be altered in such a way that anomalous diffusion does not become apparent on larger length scales.
However, diffusion arises from the microscopic interactions of a lipid with its neighbors and the employed system size is large enough to feel an ensemble of surrounding lipids. Hence, it is not expected that the periodic boundaries suddenly alter the lipid diffusion.
Along these lines, one might further argue that DPD might not correctly reflect the microscopic interactions and can therefore not be compared to experimental data. Indeed, DPD can realize only Schmidt numbers of $\mathcal{O}(1)$, defined as the ratio between momentum diffusivity and mass diffusivity, due to the DPD softcore potentials.
Despite that, DPD recovers the correct hydrodynamics of the Navier-Stokes equation as shown by Hoogerbrugge and Koelman [Hoogerbrugge92]. Moreover, when taking the fluctuation-dissipation theorem into account [Español95], DPD gives rise to correct equilibrium properties of the NVT ensemble. This suggests that DPD is indeed a suitable method for studying lipid diffusion 'in silico'.
One might ask what gave rise to anomalous diffusion in the study of Harland et al [Harland10]. In the study fluorescent particles of $100nm$ size were attached via chemical linkers to lipids with specific headgroups. Therefore, an unknown amount of lipids could bind to the fluorescent bead. If we consider now that a lipid with a typical diffusion coefficient of $D = 4\mu m^2/s$ [Korlach99] covers a distance of $200nm$ within $0.01s$ (the lower end of their experimental range), this distance is on the order of the bead size. Hence, on this time scale lipids lipids will feel their confinement and thus the fluorescent bead will be subject to elastic retraction forces when moving. For times of $\mathcal{O}(s)$ lipids cover a distance roughly 20 times the bead's sizes. Effects due to the confinement will likely average out, giving rise to normal diffusion. When trying to assess the effect of particle size, they employed even larger beads of $260nm$ size. Still, elastic retraction forces should be still measurable on the subsecond scale leading to anomalous diffusion. An alternative explanation might be that due to $100nm$-sized bead properties of the surrounding bulk water are sampled as compared to the $4nm$-sized membrane. Hence, employing even larger fluorescent beads of $260nm$ is not a useful approach to exclude bead size related artifacts. Yet, another explanation might be that subdiffusion can emerge in single particle tracking as a result of measurement uncertainties/noise [Martin02].
The question about the exact nature of diffusion within lipid membranes itself

is of importance since, e.g. anomalous diffusion influences profoundly chemical reactions rates [Guigas08] and cellular structure formation processes (cf. Chap. 7 and [Weiss03a]). Together with previous experimental studies [Korlach99; Kahya03; Benda06; Jönsson08; Horton10] this analysis provides strong indication that artificial homogeneous membranes (in contrast to heterogeneous cellular membranes) are purely viscous with normal diffusive behavior suggesting that the observed effect by Harland et al [Harland10] is a result of the specific experimental setup.

Chapter 9

Conclusion

9.1 Summary

In the course of this work self-organization and structure formation processes within the cell's early secretory pathway have been elucidated. In particular, coarse grained computer simulations were employed/developed to study intertwined transport processes from the micron scale of the Golgi Apparatus down to the nanometer scale of single lipids.

For an overview, let us look at the studied phenomena in a sequence from small to larger length scales. Since the lipid diffusion affects reaction kinetics and structure formation processes, we studied lipid motion within homogeneous membranes and confirmed that membranes resemble purely viscous two-dimensional fluids with normal diffusion characteristics. Although lipid spreading in the inhomgeneneous cellular membranes is potentially subdiffusive, gaining insight in the underlying transport processes is a crucial first step in order to validate our basic membrane model before addressing more complex phenomena.

As part of a larger study, it was shown that bending stiffness can give rise to lipid sorting and domain formation. Particularly, in a mixture of softer and stiffer lipid species the free energy of the system can be reduced by adapting the concentration to the local curvature. In order to study curvature-modulated sorting of lipids the local membrane bending stiffness as a function of lipid concentration has to be known. It was found that the membrane stiffness dependency on lipid concentration exhibits a symmetric tangent-hyperbolicus like relation. Due to this specific dependency a higher sorting efficiency and a faster dynamics towards the systems equilibrium state can be achieved as compared to, e.g., a linear dependency.

In turn, lipid membranes are crucial for intracellular vesicle transport. Here, a model was presented that elucidated how COPI domains can emerge – precur-

sors of COPI vesicles. In the model, proteins of the COPI machinery localized preferentially to certain lipid species while altering the lipid milieu at the same time. Strikingly, it was shown that the restraint of a finite cytosolic protein pool could enhance pattern formation. Similarly, anomalous Arf1/ArfGAP diffusion on membranes could change pattern structure as well as enhance domain formation. Another feature of COPI vesicles in vivo is the need to shed their coats rapidly after formation to allow for subsequent fusion reactions. A curvature-sensitive coat detachment could provide means to fulfill this requirement. However, because the COPI complex bends the membrane, a curvature-mediated regulation gives rise to an intrinsic instability that could hamper vesicle formation. Here, the effects of a curvature-mediated detachment were elucidated with a simple one-dimensional chain model with parameters that are consistent with those that have been measured for the COPI machinery. Despite the intrinsic instability, a curvature-sensitive detachment mechanism seems to be equally well suited for vesicle formation as compared to dissociation with constant average rates.
Zooming out from the details of intra-Golgi transport, Golgi structure formation itself was elucidated. Thus far, no coherent picture capturing the diverse Golgi phenotypes had been drawn. Here, a coarse-grained computational model was formulated that captured experimentally observed Golgi phenotypes as well as the self-organized morphogenesis of the Golgi apparatus. Specifically, it was observed that a sufficient vesicle influx from the endoplasmic reticulum is necessary to generate ordered Golgi structures. Moreover, it was shown that changes in the underlying COPI transport and fusion machinery significantly altered the amount of Golgi cisternae, cisternae size as well as Golgi stack turnover times. In addition, modifications of intra-Golgi transport could generate the specific Golgi phenotypes in the yeast *Saccharomyces cerevisiae* and in the fruit fly *Drosophila melanogaster*.

9.2 Outlook

As we have seen here, cellular transport requires the concerted interaction of processes acting on different length scales e.g. ranging from domain formation on membranes over vesicle budding to the morphogenesis of the Golgi complex. Unfortunately, remaining questions in that field can hardly be addressed via optical light microscopy since these processes are beyond the diffraction limit nor can they be studied via electron microscopy due to the lack of temporal resolution.
In turn, computer simulations have proven to be versatile tools that are in principle capable of tackling transport-related questions. Nevertheless, it is currently not possible to capture molecular details while covering processes on the micron and minutes scale. Thus, similar to the approach presented here, different types

of simulations are required to shed light on processes spanning different length and time scales. In future work, this type of 'upscaling' will most likely become even more important. Especially, drawing quantitative connection between models on different length/time scales is of importance. In other words, observables such as reaction rates and mechanical properties of models on larger scales have to be gauged by models operating on smaller scales in oder to make quantitative predictions.
Along these lines, recent studies have addressed vesicle budding and fusion processes [Shillcock05; Reynwar07] with molecular resolution yielding insights about the dynamics of these processes. Further quantification could provide exact budding and fusion rates. Taken together with an implementation of molecular sorting processes [Weiss00; Heinrich05], this approach could give detailed insight into transport and self-organization processes on the scale of whole cellular organelles such as the endoplasmic reticulum or the Golgi apparatus.

Part III

Appendix

Parameters employed in the Golgi self-organization model

parameter	description	value
$\Delta t\,[\mu\mathrm{s}]$	time step	500
$r_0\,[\mathrm{nm}]$	VTC radius	100
$r_c\,[\mathrm{nm}]$	cutoff distance	340
$D\,[\mu\mathrm{m}^2/\mathrm{s}]$	diffusion coefficient	0.1
$k_{\mathrm{rep}}\,[\mu\mathrm{N}/\mathrm{m}]$	repulsion spring constant	4.1
$k_{\mathrm{tet}}\,[\mu\mathrm{N}/\mathrm{m}]$	tethering spring constant	2.5
$F_0\,[\mu\mathrm{N}/\mathrm{m}]$	maximum force	17
$r_{\mathrm{on}}\,[1/\mathrm{s}]$	tether formation rate	10
$r_{\mathrm{off}}\,[1/\mathrm{s}]$	tether detachment rate	$0.5/\mathrm{s}$
$r_{\mathrm{fiss}}\,[1/\mathrm{s}]$	plasma membrane secretion rate	1
$\alpha_\perp\,[J]$	perpendicular force constant (cisternae)	$2.5 \cdot 10^{-19}$
$\alpha_\parallel\,[J]$	spin alignment constant (cisternae)	$1.0 \cdot 10^{-21}$

Table 9.1: *Table of parameters employed for the self-organized Golgi morphogenesis simulations.*

Parameters employed in the budding chain model

Here, a summary of parameters for the budding chain model in terms of natural length scale r_0, time scale τ and viscosity of the surrounding fluid γ_v is provided.

parameter	description	value
$\Gamma_{\mathrm{on}}\,[1/\mathrm{s}]$	coat attachment rate	0.1
$D_{\mathrm{coat}}\,[\mu m^2/s]$	diffusion coefficient (coat)	1
$\Delta T\,[\mu\mathrm{s}]$	time step (coat dynamics)	25
$r_0\,[\mathrm{nm}]$	intrinsic length scale	2.5
$D\,[r_0^2/\tau]$	diffusion coefficient (nodes)	1
$\Delta t\,[\tau]$	time step node fluctuation	$7.5 \cdot 10^{-5}$
$k_{\mathrm{bend}}/\gamma_v\,[r_0^2/\tau]$	bending stiffness (uncoated)	30
$k_0/\gamma_v\,[1/\tau]$	spring constant (uncoated)	$1.5 \cdot 10^3$
$k_1/\gamma_v\,[1/\tau]$	spring constant (coat)	$3.0 \cdot 10^3$

Table 9.2: *Overview of employed parameters in the budding chain model.*

Bibliography

[Abe05] Abe S and Thurner S. Anomalous diffusion in view of einstein's 1905 theory of brownian motion. *Physica A*, **356**, pp. 403–407, 2005

[Alberts08] Alberts B. *Molecular Biology of the Cell*. Garland Science, New York, 5th ed., 2008

[Ambroggio10] Ambroggio E, Sorre B, Bassereau P, Goud B, Manneville JB and Antonny B. Arfgap1 generates an arf1 gradient on continuous lipid membranes displaying flat and curved regions. *Embo Journal*, **29**, pp. 292–303, 2010. doi:10.1038/emboj.2009.341

[Antonny97] Antonny B, Huber I, Paris S, Chabre M and Cassel D. Activation of adp-ribosylation factor 1 gtpase-activating protein by phosphatidylcholine-derived diacylglycerols. *Journal of Biological Chemistry*, **272**, pp. 30848–30851, 1997

[Antonny01] Antonny B, Madden D, Hamamoto S, Orci L and Schekman R. Dynamics of the copii coat with gtp and stable analogues. *Nature Cell Biology*, **3**, pp. 531–537, 2001

[Aridor02] Aridor M and Traub LM. Cargo selection in vesicular transport: the making and breaking of a coat. *Traffic*, **3**, pp. 537–546, Aug 2002

[Axelrod76] Axelrod D, Koppel DE, Schlessinger J, Elson E and Webb WW. Mobility measurement by analysis of fluorescence photobleaching recovery kinetics. *Biophys J*, **16**, pp. 1055–1069, Sep 1976. doi:10.1016/S0006-3495(76)85755-4

[Axelsson01] Axelsson MA, Karlsson NG, Steel DM, Ouwendijk J, Nilsson T and Hansson GC. Neutralization of ph in the golgi apparatus causes redistribution of glycosyltransferases and

changes in the o-glycosylation of mucins. *Glycobiology*, **11**, pp. 633–644, Aug 2001

[Banks05] Banks DS and Fradin C. Anomalous diffusion of proteins due to molecular crowding. *Biophys J*, **89**, pp. 2960–2971, Nov 2005. doi:10.1529/biophysj.104.051078

[Barr97] Barr FA, Puype M, Vandekerckhove J and Warren G. Grasp65, a protein involved in the stacking of golgi cisternae. *Cell*, **91**, pp. 253–62, 1997

[Benda06] Benda A, Fagul'ová V, Deyneka A, Enderlein J and Hof M. Fluorescence lifetime correlation spectroscopy combined with lifetime tuning: new perspectives in supported phospholipid bilayer research. *Langmuir*, **22**, pp. 9580–9585, Nov 2006. doi:10.1021/la061573d

[Bennett93] Bennett MK, García-Arrarás JE, Elferink LA, Peterson K, Fleming AM, Hazuka CD and Scheller RH. The syntaxin family of vesicular transport receptors. *Cell*, **74**, pp. 863–873, Sep 1993

[Bevis02] Bevis BJ, Hammond AT, Reinke CA and Glick BS. De novo formation of transitional er sites and golgi structures in pichia pastoris. *Nat Cell Biol*, **4**, pp. 750–756, Oct 2002. doi:10.1038/ncb852

[Bigay03] Bigay J, Gounon P, Robineau S and Antonny B. Lipid packing sensed by arfgap1 couples copi coat disassembly to membrane bilayer curvature. *Nature*, **426**, pp. 563–566, 2003

[Bigay05] Bigay J, Casella JF, Drin G, Mesmin B and Antonny B. Arfgap1 responds to membrane curvature through the folding of a lipid packing sensor motif. *EMBO*, **24**, pp. 2244–2253, 2005

[Bonfanti98] Bonfanti L, Mironov AA, Martínez-Menárguez JA, Martella O, Fusella A, Baldassarre M, Buccione R, Geuze HJ, Mironov AA and Luini A. Procollagen traverses the golgi stack without leaving the lumen of cisternae: evidence for cisternal maturation. *Cell*, **95**, pp. 993–1003, Dec 1998

[Bonifacino04] Bonifacino J and Glick B. The mechanisms of vesicle budding and fusion. *Cell*, **116**, pp. 153–166, 2004

[Bouchaud90] Bouchaud JP and Georges A. Anomalous diffusion in disordered media: Statistical mechanisms, models and physical applications. *Physics Reports*, **195**, pp. 127 – 293, 1990. ISSN 0370-1573. doi:DOI:10.1016/0370-1573(90)90099-N

[Brannigan05] Brannigan G and Brown F. Composition dependence of bilayer elasticity. *Journal of Chemical Physics*, **122**, p. 074905, 2005

[Brockmann99] Brockmann D and Geisel T. The ecology of gaze shifts. *Neurocomputing*, **2**, pp. 643–650, 1999

[Bronstein83] Bronstein I and Semendjajew K. *Taschenbuch der Mathematik*. 1983

[Brown93] Brown HA, Gutowski S, Moomaw CR, Slaughter C and Sternweis PC. Adp-ribosylation factor, a small gtp-dependent regulatory protein, stimulates phospholipase d activity. *Cell*, **75**, pp. 1137–1144, Dec 1993

[Budnik09] Budnik A and Stephens DJ. Er exit sites–localization and control of copii vesicle formation. *FEBS Lett*, **583**, pp. 3796–3803, Dec 2009. doi:10.1016/j.febslet.2009.10.038

[Chen01] Chen YA and Scheller RH. Snare-mediated membrane fusion. *Nat Rev Mol Cell Biol*, **2**, pp. 98–106, Feb 2001. doi:10.1038/35052017

[Cole96] Cole N, Sciaky N, Marotta A, Song J and Lippincott-Schwartz J. Golgi dispersal during microtubule disruption: regeneration of golgi stacks at peripheral endoplasmatic reticulum exit sites. *Molecular Biology of the Cell*, **7**, pp. 631–650, 1996

[Cosson94] Cosson P and Letourneur F. Coatomer interaction with di-lysine endoplasmic reticulum retention motifs. *Science*, **263**, pp. 1629–1631, Mar 1994

[Cosson05] Cosson P, Ravazzola M, Varlamov O, Söllner T, Liberto M, Volchuk A, Rothman J and Orci L. Dynamic transport

of snare proteins in the golgi apparatus. *PNAS*, **102**, pp. 14647–14652, 2005. doi:10.1073/pnas.0507394102

[Cukierman95] Cukierman E, Huber I, Rotman M and Cassel D. The arf1 gtpase-activating protein: zinc finger motif and golgi complex localization. *Science*, **270**, pp. 1999–2002, Dec 1995

[Drin08] Drin G, Morello V, Casella JF, Gounon P and Antonny B. Asymetric tethering of flat and curved lipid membranes by a golgin. *Science*, **320**, pp. 670–673, 2008. doi:10.1126/science.1155821

[Einstein05] Einstein A. Über die von der molekularkinetischen theorie der wärme geforderten bewegung von in ruhenden flüssigkeiten suspendierten teilchen. *Annalen der Physik*, **17**, pp. 549–560, 1905

[Elsner03] Elsner M, Hashimoto H, Simpson J, Cassel D and Nilsson T. Spatiotemporal dynamics of the copi vesicle machinery. *EMBO reports*, **4**, pp. 1000–1005, 2003. doi:10.1038/sj.embor.embor942

[Emr09] Emr S, Glick BS, Linstedt AD, Lippincott-Schwartz J, Luini A, Malhotra V, Marsh BJ, Nakano A, Pfeffer SR, Rabouille C, Rothman JE, Warren G and Wieland FT. Journeys through the golgi–taking stock in a new era. *J Cell Biol*, **187**, pp. 449–453, Nov 2009. doi:10.1083/jcb.200909011

[Engelman05] Engelman DM. Membranes are more mosaic than fluid. *Nature*, **438**, pp. 578–580, Dec 2005. doi:10.1038/nature04394

[Español95] Español P and Warren P. Statistical mechanics of dissipative particle dynamics. *EPL (Europhysics Letters)*, **30**, p. 191, 1995

[Farhan08] Farhan H, Weiss M, Tani K, Kaufman R and Hauri HP. Adaptation of endoplasmatic reticulum exit sites to acute and chronic increases in cargo load. *EMBO Journal*, **27**, pp. 2043–2054, 2008

[Foret08] Foret L and Sens P. Kinetic regulation of coated vesicles secretion. *PNAS*, **39**, pp. 14763–14768, 2008. doi:10.1073/pnas.0801173105

[Forster06] Forster R, Weiss M, Zimmermann T, Reynaud EG, Verissimo F, Stephens DJ and Pepperkok R. Secretory cargo regulates the turnover of copii subunits at single er exit sites. *Curr Biol*, **16**, pp. 173–179, 2006

[Gierer72] Gierer A and Meinhardt H. A theory of biological pattern formation. *Kybernetik*, **12**, pp. 30–39, Dec 1972

[Girod99] Girod A, Storrie B, Simpson JC, Johannes L, Goud B, Roberts LM, Lord JM, Nilsson T and Pepperkok R. Evidence for a cop-i-independent transport route from the golgi complex to the endoplasmic reticulum. *Nat Cell Biol*, **1**, pp. 423–30, 1999

[Glick97] Glick B, Elston T and Oster G. A cisternal maturation mechanism can explain the asymmetry of the golgi stacked. *FEBS letters*, **414**, pp. 177–181, 1997. doi: 10.1016/S0014-5793(97)00984-8

[Glick09] Glick BS and Nakano A. Membrane traffic within the golgi apparatus. *Annu Rev Cell Dev Biol*, **25**, pp. 113–132, 2009. doi:10.1146/annurev.cellbio.24.110707.175421

[Golding06] Golding I and Cox EC. Physical nature of bacterial cytoplasm. *Phys Rev Lett*, **96**, p. 098102, Mar 2006. doi: 10.1103/PhysRevLett.96.098102

[Goychuk09] Goychuk I. Viscoelastic subdiffusion: From anomalous to normal. *Phys Rev E*, **80**, p. 046125, Oct 2009. doi:10.1103/PhysRevE.80.046125

[Guigas07] Guigas G, Kalla C and Weiss M. Probing the nanoscale viscoelasticity of intracellular fluids in living cells. *Biophys J*, **93**, pp. 316–323, Jul 2007. doi:10.1529/biophysj.106.099267

[Guigas08] Guigas G and Weiss M. Sampling the cell with anomalous diffusion - the discovery of slowness. *Biophysical Journal*, **94**, pp. 90–94, 2008

[Gurkan06] Gurkan C, Stagg SM, Lapointe P and Balch WE. The copii cage: unifying principles of vesicle coat assembly. *Nat Rev Mol Cell Biol*, **7**, pp. 727–38, 2006

[Hammond00] Hammond A and Glick B. Dynamics of transitional endoplasmatic reticulum sites in vertebrate cells. *Molecular Biology of the Cell*, **11**, pp. 3013–3030, 2000

[Hardt79] Hardt S. Rates of diffusion controlled reactions in one, two and three dimensions. *Biophysical Chemistry*, **10**, pp. 239–243, 1979

[Harland10] Harland C, Bradley M and Parthasarathy R. Phospholipid bilayers are viscoelastic. *PNAS*, **107**, pp. 19146–19150, 2010

[He08] He Y, Burov S, Metzler R and Barkai E. Random time-scale invariant diffusion and transport coefficients. *Phys Rev Lett*, **101**, p. 058101, Aug 2008

[Heinrich05] Heinrich R and Rapoport T. Generation of nonidentical compartments in vesicular transport systems. *Journal of Cell Biology*, **168**, pp. 271–280, 2005. doi:10.1083/jcb.200409087

[Heinzer08] Heinzer S, Wörz S, Kalla C, Rohr K and Weiss M. A model for the self-organization of exit sites in the endoplasmic reticulum. *Journal of Cell Science*, **121**, pp. 55–64, 2008. doi:10.1242/jcs.013383

[Helfrich73] Helfrich W. Elastic properties of lipid bilayers: theory and possible experiments. *Z Naturforsch C*, **28**, pp. 693–703, 1973

[Hell94] Hell SW and Wichmann J. Breaking the diffraction resolution limit by stimulated emission: stimulated-emission-depletion fluorescence microscopy. *Opt Lett*, **19**, pp. 780–782, Jun 1994

[Hirschberg98] Hirschberg K, Miller C, Ellenberg J, Presley J, Siggia E, Phair R and Lippincott-Schwartz J. Kinetic analysis of secretory protein traffic and characterization of golgi to plasma membrane transport intermediates in living cells. *JCB*, **143**, pp. 1485–1503, 1998

[Ho89] Ho WC, Allan VJ, van Meer G, Berger EG and Kreis TE. Reclustering of scattered golgi elements occurs along microtubules. *Eur J Cell Biol*, **48**, pp. 250–263, Apr 1989

[Hoogerbrugge92] Hoogerbrugge PJ and Koelman JMVA. Simulating Microscopic Hydrodynamic Phenomena with Dissipative Particle Dynamics. *EPL (Europhysics Letters)*, **19**, pp. 155–160, Jun 1992. ISSN 0295-5075. doi:10.1209/0295-5075/19/3/001

[Horton10] Horton MR, Hofling F, Radler JO and Franosch T. Development of anomalous diffusion among crowding proteins. *Soft Matter*, **6**, pp. 2648–2656, 2010. doi:10.1039/B924149C

[Howard01] Howard M, Rutenberg A and de Vet S. Dynamic compartmentalization of bacteria: Accurate division in e.coli. *Physical Review Letters*, **87**, p. 278102, 2001

[Howard03] Howard M and Rutenberg AD. Pattern formation inside bacteria: Fluctuations due to the low copy number of proteins. *Phys Rev Lett*, **90**, p. 128102, 2003. doi: 10.1103/PhysRevLett.90.128102

[Huang06] Huang KC, Mukhopadhyay R and Wingreen NS. A curvature-mediated mechanism for localization of lipids to bacterial poles. *PLoS Comput Biol*, **2**, p. e151, Nov 2006. doi:10.1371/journal.pcbi.0020151

[Hufnagel04] Hufnagel L, Brockmann D and Geisel T. Forecast and control of epidemics in a globalized world. *Proc Natl Acad Sci U S A*, **101**, pp. 15124–15129, Oct 2004. doi: 10.1073/pnas.0308344101

[Hughes81] Hughes BD, Pailthorpe BA and White LR. The translational and rotational drag on a cylinder moving in a membrane. *Journal of Fluid Mechanics*, **110**, pp. 349–372, 1981. doi: 10.1017/S0022112081000785

[Hughes09] Hughes H, Budnik A, Schmidt K, Palmer KJ, Mantell J, Noakes C, Johnson A, Carter DA, Verkade P, Watson P and Stephens DJ. Organisation of human er-exit sites: requirements for the localisation of sec16 to transitional er. *J Cell Sci*, **122**, pp. 2924–2934, Aug 2009. doi: 10.1242/jcs.044032

[Illya06] Illya G, Lipowsky R and Shillcock J. Two-component membrane material properties and domain formation from dissi-

pative particle dynamics. *Journal of Chemical Physics*, **125**, p. 114710, 2006

[Imparato05] Imparato A, Shillcock J and Lipowsky R. Shape fluctuations and elastic properties of two-component bilayer membranes. *Europhysics Letters*, **69**, pp. 650–656, 2005

[Jackson90] Jackson MR, Nilsson T and Peterson PA. Identification of a consensus motif for retention of transmembrane proteins in the endoplasmic reticulum. *EMBO J*, **9**, pp. 3153–3162, Oct 1990

[Jackson09] Jackson C. Mechanisms of transport through the golgi complex. *Journal of Cell Science*, **122**, pp. 443–452, 2009

[Jakobsen05a] Jakobsen AF. Constant-pressure and constant-surface tension simulations in dissipative particle dynamics. *J Chem Phys*, **122**, p. 124901, Mar 2005. doi:10.1063/1.1867374

[Jakobsen05b] Jakobsen AF, Mouritsen OG and Weiss M. Close-up view of the modifications of fluid membranes due to phospholipase a 2. *Journal of Physics: Condensed Matter*, **17**, p. S4015, 2005

[Jensen04] Jensen MØ and Mouritsen OG. Lipids do influence protein function-the hydrophobic matching hypothesis revisited. *Biochim Biophys Acta*, **1666**, pp. 205–226, Nov 2004. doi:10.1016/j.bbamem.2004.06.009

[Jönsson08] Jönsson P, Jonsson MP, Tegenfeldt JO and Höök F. A method improving the accuracy of fluorescence recovery after photobleaching analysis. *Biophys J*, **95**, pp. 5334–5348, Dec 2008. doi:10.1529/biophysj.108.134874

[Kahya03] Kahya N, Scherfeld D, Bacia K, Poolman B and Schwille P. Probing lipid mobility of raft-exhibiting model membranes by fluorescence correlation spectroscopy. *J Biol Chem*, **278**, pp. 28109–28115, Jul 2003. doi:10.1074/jbc.M302969200

[Kellokumpu02] Kellokumpu S, Sormunen R and Kellokumpu I. Abnormal glycosylation and altered golgi structure in colorectal cancer: dependence on intra-golgi ph. *FEBS Lett*, **516**, pp. 217–224, Apr 2002

[Kirchhausen00] Kirchhausen T. Three ways to make a vesicle. *Nat Rev Mol Cell Biol*, **1**, pp. 187–98, 2000

[Koch94] Koch AJ and Meinhardt H. Biological pattern formation: from basic mechanisms to complex structures. *Rev Mod Phys*, **66**, pp. 1481–1507, Oct 1994. doi:10.1103/RevModPhys.66.1481

[Kondylis01] Kondylis V, Goulding S, Dunne J and Rabouille C. Biogenesis of golgi stacks in imaginal discs of drosophila melanogaster. *Molecular Biology of the Cell*, **12**, pp. 2308–2327, 2001

[Kondylis09] Kondylis V and Rabouille C. The golgi apparatus: lessons from drosophila. *FEBS Letters*, **583**, pp. 3827–3838, 2009

[Korlach99] Korlach J, Schwille P, Webb WW and Feigenson GW. Characterization of lipid bilayer phases by confocal microscopy and fluorescence correlation spectroscopy. *Proc Natl Acad Sci U S A*, **96**, pp. 8461–8466, Jul 1999

[Kranenburg03] Kranenburg M, Venturoli M and Smit B. Molecular simulations of mesoscopic bilayer phases. *Physical Review E*, **67**, p. 060901, 2003

[Kruse02] Kruse K. A dynamic model for determining the middle of escherichia coli. *Biophysical Journal*, **82**, pp. 618–627, 2002

[Ktistakis95] Ktistakis NT, Brown HA, Sternweis PC and Roth MG. Phospholipase d is present on golgi-enriched membranes and its activation by adp ribosylation factor is sensitive to brefeldin a. *Proc Natl Acad Sci U S A*, **92**, pp. 4952–4956, May 1995

[Lanoix99] Lanoix J, Ouwendijk J, Lin CC, Stark A, Love HD, Ostermann J and Nilsson T. Gtp hydrolysis by arf-1 mediates sorting and concentration of golgi resident enzymes into functional cop i vesicles. *EMBO J*, **18**, pp. 4935–4948, Sep 1999. doi:10.1093/emboj/18.18.4935

[Lanoix01] Lanoix J, Ouwendijk J, Stark A, Szafer E, Cassel D, Dejgaard K, Weiss M and Nilsson T. Sorting of golgi resident proteins into different subpopulations of copi vesicles: a role

for arfgap1. *Journal of Cell Biology*, **155**, pp. 1199–1212, 2001

[Laradji04] Laradji M and Kumar PS. Dynamics of domain growth in self-assembled fluid vesicles. *Phys Rev Lett*, **93**, p. 198105, Nov 2004. doi:10.1103/PhysRevLett.93.198105

[Laradji05] Laradji M and Kumar P. Domain growth, budding, and fission in phase-separating self-assembled fluid bilayers. *Journal of Chemical Physics*, **123**, p. 224902, 2005

[Laux00] Laux T, Fukami K, Thelen M, Golub T, Frey D and Caroni P. Gap43, marcks, and cap23 modulate pi(4,5)p(2) at plasmalemmal rafts, and regulate cell cortex actin dynamics through a common mechanism. *J Cell Biol*, **149**, pp. 1455–1472, Jun 2000

[Lederkremer01] Lederkremer G, Cheng Y, Petre B, Vogan E, Springer S, Schekman R, Walz T and Kirchhausen T. Structure of the sec23p/24p and sec13p/31p complexes of copii. *PNAS*, **98**, pp. 10704–10709, 2001

[Lee04] Lee M, Miller E, Goldberg J, Orci L and Schekman R. Bidirectional protein transport between the er and golgi. *Annual Review of Cell and Developmental Biology*, **20**, pp. 87–123, 2004

[Lepock83] Lepock JR, Cheng KH, Campbell SD and Kruuv J. Rotational diffusion of tempone in the cytoplasm of chinese hamster lung cells. *Biophys J*, **44**, pp. 405–412, Dec 1983. doi:10.1016/S0006-3495(83)84314-8

[Linstedt99] Linstedt AD. Stacking the cisternae. *Curr Biol*, **9**, pp. R893–R896, Dec 1999

[Liu05] Liu W, Duden R, Phair R and Lippincott-Schwartz J. Arfgap1 dynamics and its role in copi coat assembly on golgi membranes of living cells. *Journal of Cell Biology*, **168**, pp. 1053–1063, 2005

[Losev06] Losev E, Reinke C, Ellen J, Strongin D, Bevis B and Glick B. Golgi maturation visualized in living yeast. *Nature*, **441**, pp. 1002–1006, 2006. doi:10.1038/nature04717

[Lowe98] Lowe M, Nakamura N and Warren G. Golgi division and membrane traffic. *Trends Cell Biol*, **8**, pp. 40–4, 1998

[Lubelski08] Lubelski A, Sokolov IM and Klafter J. Nonergodicity mimics inhomogeneity in single particle tracking. *Phys Rev Lett*, **100**, p. 250602, Jun 2008

[Luini08] Luini A, Mironov A, Polishchuk E and Polishchuk R. Morphogenesis of post-golgi transport carriers. *Histochemistry and Cell Biology*, **129**, pp. 153–161, 2008

[Maeda08] Maeda Y, Ide T, Koike M, Uchiyama Y and Kinoshita T. Gphr is a novel anion channel critical for acidification and functions of the golgi apparatus. *Nat Cell Biol*, **10**, pp. 1135–45, 2008

[Magde72] Magde D, Elson E and Webb WW. Thermodynamic fluctuations in a reacting system—measurement by fluorescence correlation spectroscopy. *Phys Rev Lett*, **29**, pp. 705–708, Sep 1972. doi:10.1103/PhysRevLett.29.705

[Mandelbrot68] Mandelbrot B and Van Ness JW. Fractional brownian motions, fractional noises and applications. *SIAM Review*, **10**, pp. 422–437, 1968. ISSN 00361445. doi:10.2307/2027184

[Manneville08] Manneville J, Casella J, Ambroggio E, Gounon P, Bertherat J, Bassereau P, Cartaud J, Antonny B and Goud B. Copi coat assembly occurs on liquid-disordered domains and the associated membrane deformations are limited by membrane tension. *PNAS*, **105**, pp. 16946–16951, 2008

[Marsh04] Marsh B, Volkmann N, McIntosh R and Howe K. Direct continuities between cisternae at different levels of the golgi complex in glucose-stimulated mouse islet beta cells. *PNAS*, **101**, pp. 5565–5570, 2004

[Martin01] Martin T. Pi(4,5)p2 regulation of surface membrane traffic. *Current Opinion in Cell Biology*, **13**, pp. 493–499, 2001

[Martin02] Martin DS, Forstner MB and Käs JA. Apparent subdiffusion inherent to single particle tracking. *Biophys J*, **83**, pp. 2109–2117, Oct 2002. doi:10.1016/S0006-3495(02)73971-4

[Martinez-Alonso05] Martinez-Alonso E, Egea G, Ballesta J and Martinez-Menarguez J. Structure and dynamics of the golgi complex at 15 °C: low temperature induces the formation of golgi-derived tubules. *Traffic*, **6**, pp. 32–44, 2005. doi: 10.1111/j.1600-0854.2004.00242.x

[Martinez-Menárguez01] Martinez-Menárguez JA, Prekeris R, Oorschot VM, Scheller R, Slot JW, Geuze HJ and Klumperman J. Peri-golgi vesicles contain retrograde but not anterograde proteins consistent with the cisternal progression model of intra-golgi transport. *J Cell Biol*, **155**, pp. 1213–1224, Dec 2001. doi:10.1083/jcb.200108029

[Mason95] Mason TG, Bibette J and Weitz DA. Elasticity of compressed emulsions. *Phys Rev Lett*, **75**, pp. 2051–2054, Sep 1995. doi:10.1103/PhysRevLett.75.2051

[Mastro84a] Mastro AM, Babich MA, Taylor WD and Keith AD. Diffusion of a small molecule in the cytoplasm of mammalian cells. *Proc Natl Acad Sci U S A*, **81**, pp. 3414–3418, Jun 1984

[Mastro84b] Mastro AM and Keith AD. Diffusion in the aqueous compartment. *J Cell Biol*, **99**, pp. 180s–187s, Jul 1984

[Matsuoka01] Matsuoka K, Schekman R, Orci L and Heuser J. Surface structure of the copii-coated vesicle. *PNAS*, **98**, pp. 13705–13709, 2001. doi:10.1073/pnas.241522198

[Matsuura-Tokita06] Matsuura-Tokita K, Takeuchi M, Ichihara A, Mikuriya K and Nakano A. Live imaging of yeast golgi cisternal maturation. *Nature*, **441**, pp. 1007–1010, Jun 2006. doi: 10.1038/nature04737

[Meinhardt01] Meinhardt H and de Boer PA. Pattern formation in escherichia coli: a model for the pole-to-pole oscillations of min proteins and the localization of the division site. *Proc Natl Acad Sci U S A*, **98**, pp. 14202–14207, Dec 2001. doi:10.1073/pnas.251216598

[Mercker11] Mercker M, Ptashnyk M, Kuehnle J, Hartmann D, Weiss M and Jaeger W. A multiscale and multidisciplinary approach to curvature modulated sorting in biological membranes. *submitted to: Journal of Theoretical Biology*, 2011

[Metzler00] Metzler R and Klafter J. The random walk's guide to anomalous diffusion: a fractional dynamics approach. *Physics Reports*, **339**, pp. 1 – 77, 2000. ISSN 0370-1573. doi:DOI:10.1016/S0370-1573(00)00070-3

[Miao94] Miao L, Seifert U, Wortis M and Döbereiner HG. Budding transitions of fluid-bilayer vesicles: The effect of area-difference elasticity. *Phys Rev E Stat Phys Plasmas Fluids Relat Interdiscip Topics*, **49**, pp. 5389–5407, Jun 1994

[Miller03] Miller EA, Beilharz TH, Malkus PN, Lee MCS, Hamamoto S, Orci L and Schekman R. Multiple cargo binding sites on the copii subunit sec24p ensure capture of diverse membrane proteins into transport vesicles. *Cell*, **114**, pp. 497–509, Aug 2003

[Moritz92] Moritz A, Graan PND, Gispen WH and Wirtz KW. Phosphatidic acid is a specific activator of phosphatidylinositol-4-phosphate kinase. *J Biol Chem*, **267**, pp. 7207–7210, Apr 1992

[Mouritsen04] Mouritsen OG. *Life - As a Matter of Fat*. Springer, 1st ed., November 2004. ISBN 3540232486

[Murray04] Murray J. *Mathematical Biology*. Springer, 2004

[Murshid04] Murshid A and Presley JF. Er-to-golgi transport and cytoskeletal interactions in animal cells. *Cell Mol Life Sci*, **61**, pp. 133–145, Jan 2004. doi:10.1007/s00018-003-3352-9

[Nedelec02] Nedelec F. Computer simulations reveal motor properties generating stable antiparallel microtubule interactions. *Journal of Cell Biology*, **158**, pp. 1005–1015, 2002. doi:10.1083/jcb.200202051

[Nikunen03] Nikunen P, Karttunen M and Vattulainen I. How would you integrate the equations of motion in dissipative particle dynamics simulations? *Computer Physics Communications*, **153**, pp. 407 – 423, 2003. ISSN 0010-4655. doi:DOI:10.1016/S0010-4655(03)00202-9

[Nilsson89] Nilsson T, Jackson M and Peterson PA. Short cytoplasmic sequences serve as retention signals for transmembrane proteins in the endoplasmic reticulum. *Cell*, **58**, pp. 707–718, Aug 1989

[Nilsson93] Nilsson T, Pypaert M, Hoe M, Slusarewicz P, Berger E and Warren G. Overlapping distribution of two glycosyltransferases in the golgi apparatus of hela cells. *Journal of Cell Biology*, **120**, pp. 5–13, 1993

[Nédélec97] Nédélec FJ, Surrey T, Maggs AC and Leibler S. Self-organization of microtubules and motors. *Nature*, **389**, pp. 305–308, Sep 1997. doi:10.1038/38532

[Osterrieder10] Osterrieder A, Hummel E, Carvalho C and Hawes C. Golgi membrane dynamics after induction of a dominant-negative mutant sar1 gtpase in tobacco. *Journal of Experimental Botany*, **61**, pp. 405–422, 2010

[Pagonabarraga01] Pagonabarraga I and Frenkel D. Dissipative particle dynamics for interacting systems. *Journal of chemical physics*, **115**, pp. 5015–5026, 2001

[Palade75] Palade G. Intracellular aspects of the process of protein synthesis. *Science*, **189**, p. 867, Sep 1975. doi:10.1126/science.189.4206.867-b

[Palmer04] Palmer KJ and Stephens DJ. Biogenesis of er-to-golgi transport carriers: complex roles of copii in er export. *Trends Cell Biol*, **14**, pp. 57–61, Feb 2004

[Pan09] Pan W, Filobelo L, Pham NDQ, Galkin O, Uzunova VV and Vekilov PG. Viscoelasticity in homogeneous protein solutions. *Phys Rev Lett*, **102**, p. 058101, Feb 2009

[Parlati02] Parlati F, Varlamov O, Paz K, McNew JA, Hurtado D, Sollner TH and Rothman JE. Distinct snare complexes mediating membrane fusion in golgi transport based on combinatorial specificity. *Proc Natl Acad Sci USA*, **99**, pp. 5424–9, 2002

[Parthasarathy06] Parthasarathy R, han Yu C and Groves JT. Curvature-modulated phase separation in lipid bilayer membranes. *Langmuir*, **22**, pp. 5095–5099, May 2006. doi:10.1021/la060390o

[Patterson08] Patterson G, Hirschberg K, Polishchuk R, Gerlich D, Phair R and Lippincott-Schwartz J. Transport through the golgi

apparatus by rapid partitioning within a two-phase membrane system. *Cell*, **133**, pp. 1055–1067, 2008. doi: 10.1016/j.cell.2008.04.044

[Pomerening03] Pomerening JR, Sontag ED and Ferrell J J E. Building a cell cycle oscillator: hysteresis and bistability in the activation of cdc2. *Nat Cell Biol*, **5**, pp. 346–51, 2003

[Presley97] Presley J, Cole N, Schroer T, Hirschberg K, Zaal K and Lippincott-Schwartz J. Er-to golgi transport visualized in living cells. *Nature*, **389**, pp. 81–85, 1997

[Preuss92] Preuss D, Mulholland J, Franzusoff A, Segev N and Botstein D. Characterization of the saccharamoyces golgi complex through the cell cycle by immunoelectron microscopy. *Molecular Biology of the Cell*, **3**, pp. 789–803, 1992

[Puri03] Puri S and Linstedt A. Capacity of the golgi apparatus for biogenesis from the endoplasmatic reticulum. *Molecular Biology of the Cell*, **14**, pp. 5011–5018, 2003

[Rabouille95] Rabouille C, Hui N, Hunte F, Kieckbusch R, Berger E, Warren G and Nilsson T. Mapping the distribution of golgi enzymes involved in the construction of complex oligosaccharides. *Journal of Cell Science*, **108**, pp. 1617–1627, 1995

[Rabouille05] Rabouille C and Klumperman J. Opinion: The maturing role of copi vesicles in intra-golgi transport. *Nat Rev Mol Cell Biol*, **6**, pp. 812–817, Oct 2005. doi:10.1038/nrm1735

[Rafelski08] Rafelski SM and Marshall WF. Building the cell: design principles of cellular architecture. *Nat Rev Mol Cell Biol*, **9**, pp. 593–602, Aug 2008. doi:10.1038/nrm2460

[Randazzo97] Randazzo PA. Functional interaction of adp-ribosylation factor 1 with phosphatidylinositol 4,5-bisphosphate. *J Biol Chem*, **272**, pp. 7688–7692, Mar 1997

[Ratto03] Ratto TV and Longo ML. Anomalous subdiffusion in heterogeneous lipid bilayers†. *Langmuir*, **19**, pp. 1788–1793, 2003. doi:10.1021/la0261803

[Rawicz00] Rawicz W, Olbrich K, McIntosh T, Needham D and Evans E. Effect of chain lenght and unsaturation on elasticity of lipid bilayers. *Biophysical Journal*, **79**, pp. 328–339, 2000

[Reichenbach07] Reichenbach T, Mobili M and Frey E. Mobility promotes and jeopardizes biodiversity in rock–paper–scissors games. *Nature*, **228**, pp. 1046–1049, 2007. doi:10.1038/nature06095

[Reynwar07] Reynwar B, Illya G, Harmandaris V, Mueller M, Kremer K and Deserno M. Aggregation and vesiculation of membrane proteins by curvature-mediated interactions. *Nature*, **447**, pp. 461–464, 2007. doi:10.1038/nature05840

[Richter04] Richter R. *The Formation of Solid-Supported Lipid Membranes and Two-Dimensional Assembly of Proteins. A Study Combining Atomic Force Microscopy and Quartz Crystal Microbalance with Dissipation Monitoring.* Ph.D. thesis, 2004

[Roth99] Roth M, Bi K, Ktistakis N and Yu S. Phospholipase d as an effector for adp-ribosylation factor in the regulation of vesicular traffic. *Chemistry and Physics of Lipids*, **98**, pp. 141–152, 1999

[Saffman75] Saffman PG and Delbrück M. Brownian motion in biological membranes. *Proc Natl Acad Sci U S A*, **72**, pp. 3111–3113, Aug 1975

[Scales97] Scales S, Pepperkok R and Kreis T. Visualization of er-to-golgi transport in living cells reveals a sequential mode of action for copii and copi. *Cell*, **90**, pp. 1137–48, 1997

[Schmidt08] Schmidt U, Guigas G and Weiss M. Cluster formation of transmembrane proteins due to hydrophobic mismatching. *Physical Review Letters*, **101**, pp. 128104 1–4, 2008

[Schmidt10] Schmidt U and Weiss M. Hydrophobic mismatch-induced clustering as a primer for protein sorting in the secretory pathway. *Biophys Chem*, **151**, pp. 34–38, Sep 2010. doi: 10.1016/j.bpc.2010.04.009

[Schnakenberg79] Schnakenberg J. Simple chemical reaction systems with limit cycle behaviour. *J Theor Biol*, **81**, pp. 389–400, Dec 1979

[Sciaky97] Sciaky N, Presley J, Smith C, Zaal K, Cole N, Moreira J, Terasaki M, Siggia E and Lippincott-Schwartz J. Golgi tubule traffic and the effects of brefeldin a visualized in living cells. *Journal of Cell Biology*, **139**, pp. 1137–1155, 1997

[Sebastian95] Sebastian KL. Path integral representation for fractional brownian motion. *Journal of Physics A: Mathematical and General*, **28**, p. 4305, 1995

[Seemann00] Seemann J, Jokitalo E, Pypaert M and Warren G. Matrix proteins can generate the higher order architecture of the golgi apparatus. *Nature*, **407**, pp. 1022–6, 2000

[Seifert97] Seifert U. Configurations of fluid membranes and vesicles. *Advances in Physics Letters*, **46**, pp. 13–137, 1997

[Shillcock05] Shillcock J and Lipowsky R. Tension-induced fusion of bilayer membranes and vesicles. *Nature Materials*, **4**, pp. 225–228, 2005

[Shillcock08] Shillcock JC. Insight or illusion? seeing inside the cell with mesoscopic simulations. *HFSP J*, **2**, pp. 1–6, 2008

[Shorter99] Shorter J, Watson R, Giannakou M, nd G Warren MC and Barr F. Grasp55, a second mammalian grasp protein involved in the stacking of golgi cisternae in a cell-free system. *EMBO*, **18**, pp. 4949–4960, 1999

[Siegel04] Siegel DP and Kozlov MM. The gaussian curvature elastic modulus of n-monomethylated dioleoylphosphatidylethanolamine: relevance to membrane fusion and lipid phase behavior. *Biophys J*, **87**, pp. 366–374, Jul 2004. doi:10.1529/biophysj.104.040782

[Simons97] Simons K and Ikonen E. Functional rafts in cell membranes. *Nature*, **387**, pp. 569–572, Jun 1997. doi:10.1038/42408

[Singer72] Singer SJ and Nicolson GL. The fluid mosaic model of the structure of cell membranes. *Science*, **175**, pp. 720–731, Feb 1972

[Sorre09] Sorre B, Callan-Jones A, Manneville JB, Nassoy P, Joanny JF, Prost J, Goud B and Bassereau P. Curvature-driven lipid sorting needs proximity to a demixing point and is aided by proteins. *Proc Natl Acad Sci U S A*, **106**, pp. 5622–5626, Apr 2009. doi:10.1073/pnas.0811243106

[Spang98] Spang A, Matsuoka K, Hamamoto S, Schekman R and Orci L. Coatomer, arf1p, and nucleotide are required to bud coat protein complex i-coated vesicles from large synthetic liposomes. *PNAS*, **95**, pp. 11199–11204, 1998

[Spang09] Spang A. On vesicle formation and tethering in the er-golgi shuttle. *Curr Opin Cell Biol*, **21**, pp. 531–536, Aug 2009. doi:10.1016/j.ceb.2009.03.003

[Stephens00] Stephens D, Lin-Marq N, Pagano A, Pepperkok R and Paccaud JP. Copi-coated er-to-golgi transport complexes segregate from copii in close proximity to er exit sites. *Journal of Cell Science*, **113**, pp. 2177–2185, 2000

[Storrie98] Storrie B, White J, Rottger S, Stelzer EH, Suganuma T and Nilsson T. Recycling of golgi-resident glycosyltransferases through the er reveals a novel pathway and provides an explanation for nocodazole-induced golgi scattering. *J Cell Biol*, **143**, pp. 1505–21, 1998

[Szleifer88] Szleifer I, Kramer D, Ben-Shaul A, Roux D and Gelbart WM. Curvature elasticity of pure and mixed surfactant films. *Phys Rev Lett*, **60**, pp. 1966–1969, May 1988. doi:10.1103/PhysRevLett.60.1966

[Sztul09] Sztul E and Lupashin V. Role of vesicle tethering factors in the er-golgi membrane traffic. *FEBS Lett*, **583**, pp. 3770–3783, Dec 2009. doi:10.1016/j.febslet.2009.10.083

[Szymanski09] Szymanski J and Weiss M. Elucidating the origin of anomalous diffusion in crowded fluids. *Phys Rev Lett*, **103**, p. 038102, Jul 2009

[Tabata09] Tabata KV, Sato K, Ide T, Nishizaka T, Nakano A and Noji H. Visualization of cargo concentration by copii minimal machinery in a planar lipid membrane. *EMBO J*, **28**, pp. 3279–3289, Nov 2009. doi:10.1038/emboj.2009.269

[Thyberg99] Thyberg J and Moskalewski S. Role of microtubules in the organization of the golgi complex. *Experimental Cell Research*, **246**, pp. 263–279, 1999

[Tolić-Nørrelykke04] Tolić-Nørrelykke IM, Munteanu EL, Thon G, Oddershede L and Berg-Sørensen K. Anomalous diffusion in living yeast cells. *Phys Rev Lett*, **93**, p. 078102, Aug 2004. doi:10.1103/PhysRevLett.93.078102

[Trucco04] Trucco A, Polishchuk R, Martella O, Pentima A, AFusella, Giandomenico D, Pietro E, Beznoussenko G, Polishchuk E, Baldassarre M, Buccione R, Geerts W, Koster A, Burger K, Mironov A and Luini A. Secretory traffic triggers the formation of tubular continuities across golgi sub-compartments. *Nature Cell Biology*, **6**, pp. 1071–1081, 2004

[Turing52] Turing A. The chemical basis of morphogenesis. *Phil Trans R Soc B*, **237**, pp. 37–72, 1952

[vanMeer98] van Meer G. Lipids of the golgi membrane. *Trends Cell Biol*, **8**, pp. 29–33, Jan 1998

[vanMeer02] van Meer G. Cell biology. the different hues of lipid rafts. *Science*, **296**, pp. 855–857, May 2002. doi:10.1126/science.1071491

[Varlamov03] Varlamov O, Volchuk A, Rahmian V, Doege C, Paumet F, Eng W, Arango N, Parlati F, Ravazzola M, Orci L, Söllner T and Rothman J. i-snares: inhibitory snares that fine-tune the specifity of membrane fusion. *Journal of Cell Biology*, **164**, pp. 79–88, 2003. doi:10.1083/jcb.200307066

[Vazquez] Vazquez J. *The porous medium equation*

[Veatch05] Veatch SL and Keller SL. Seeing spots: Complex phase behavior in simple membranes. *Biochimica et Biophysica Acta (BBA) - Molecular Cell Research*, **1746**, pp. 172 – 185, 2005. ISSN 0167-4889. doi:DOI:10.1016/j.bbamcr.2005.06.010. Lipid Rafts: From Model Membranes to Cells

[Venturoli99] Venturoli M and Smit B. Simulating the self-assembly of model membranes. *PhysChemComm*, **10**, p. 45, 1999

[Volchuk04] Volchuk A, Ravazzola M, Perelet A, Eng W, Liberto MD, Varlamov O, Fukasawa M, Engel T, Söllner T, Rothman J and Orci L. Countercurrent distribution of two distinct snare complexes mediating transport within the golgi complex. *Molecular Biology of the Cell*, **15**, pp. 1506–1518, 2004. doi:10.1091/mbc.E03080625

[Wachsmuth00] Wachsmuth M, Waldeck W and Langowski J. Anomalous diffusion of fluorescent probes inside living cell nuclei investigated by spatially-resolved fluorescence correlation spectroscopy. *J Mol Biol*, **298**, pp. 677–689, May 2000. doi: 10.1006/jmbi.2000.3692

[Weber10] Weber SC, Spakowitz AJ and Theriot JA. Bacterial chromosomal loci move subdiffusively through a viscoelastic cytoplasm. *Phys Rev Lett*, **104**, p. 238102, Jun 2010

[Weiss00] Weiss M and Nilsson T. Protein sorting in the golgi apparatus: a consequence of maturation and triggered sorting. *FEBS*, **486**, pp. 2–9, 2000

[Weiss03a] Weiss M. Stabilizing turing patterns with subdiffusion in systems with low particle numbers. *Phys Rev E Stat Nonlin Soft Matter Phys*, **68**, p. 036213, Sep 2003

[Weiss03b] Weiss M, Hashimoto H and Nilsson T. Anomalous protein diffusion in living cells as seen by fluorescence correlation spectroscopy. *Biophys J*, **84**, pp. 4043–4052, Jun 2003. doi:10.1016/S0006-3495(03)75130-3

[Weiss03c] Weiss M and Nilsson T. A kinetic proof-reading mechanism for protein sorting. *Traffic*, **4**, pp. 65–73, 2003

[Weiss04] Weiss M, Elsner M, Kartberg F and Nilsson T. Anomalous subdiffusion is a measure for cytoplasmic crowding in living cells. *Biophys J*, **87**, pp. 3518–3524, Nov 2004. doi:10.1529/biophysj.104.044263

[Whitehouse97] Whitehouse C, Burchell J, Gschmeissner S, Brockhausen I, Lloyd K and Taylor-Papadimitriou J. A transfected sialyltransferase that is elevated in breast cancer and localizes to the medial/trans-golgi apparatus inhibits the development of core-2–based o-glycans. *Journal of Cell Biology*, **137**, pp. 1229–1241, 1997

[Xu04] Xu D and Hay J. Reconstitution of copii vesicle fusion to generate a pre-golgi intermediate compartment. *Journal of Cell Biology*, **167**, pp. 997–1003, 2004. doi:10.1083/jcb.200408135

[Yamamoto02] Yamamoto S, Maruyama Y and Hyodo SA. Dissipative particle dynamics study of spontaneous vesicle formation of amphiphilic molecules. *Journal of Chemical Physics*, **116**, pp. 5842–5849, 2002

[Yamamoto03] Yamamoto S and Hyodo SA. Budding and fission dynamics of two-component vesicles. *Journal of Chemical Physics*, **118**, pp. 7937–7943, 2003

[Yoon06] Yoon TY, Jeong C, Lee SW, Kim JH, Choi MC, Kim SJ, Kim MW and Lee SD. Topographic control of lipid-raft reconstitution in model membranes. *Nature Materials*, **5**, pp. 281–285, 2006. doi:10.1038/nmat1618

[Zaal99] Zaal K, Smith C, Polishchuk R, Altan N, Cole N, Ellenberg J, Hirschberg K, Presley J, Roberts T, Siggia E, Phair R and Lippincott-Schwartz J. Golgi membranes are absorbed into and reemerge from the er during mitosis. *Cell*, **99**, pp. 589–601, 1999

Acknowledgement

In the following, I would like to thank people who helped me on the journey to finish this thesis.
First of all, I would like to thank Professor Dr. Hausmann who took an interest in my work. I am especially grateful that he helped to improve this thesis by stimulating discussions and volunteered to act as a referee.
I owe my deepest gratitude to Professor Dr. Matthias Weiss, the leader of our work group. He was full of inspiring ideas and managed to infect me with his scientific enthusiasm. Moreover, I am especially thankful for his encouragement when hurdling this thesis' obstacles and the interest he took in my personal progress.
In addition, I would like to thank Professor Ole Mouritsen who gave me the opportunity to broaden my horizon at the University in Southern Denmark in the excellent 'Memphys Center'.
I am especially thankful to Professor Julian Shillcock who supported me during my stay in Denmark. I appreciate his insight in programming, simulations as well as the many discussions that helped to improve this thesis. Moreover, it has been an dear experience to get to know Julian on a personal level.
I am also indepted to all of my colleagues and enjoyed the great atmophere in the group. First and foremost I would like to mention my office neighbor Nina Malchus with whom I not only had many insightful discussions but also shared a million laughters. Moreover, I would like to thank Diana Morozova, Marcel Hellmann, Gernot Guigas, Maria Hanulova, Ullrich Schmidt and Kristian Boye for stimulating discussions, valuable suggestions and corrections of this manuscript. In addition, I would like to thank Abiola Pollard and Tobias Rentrop who helped on short notice proofreading the manuscript.
Im Besonderen möchte ich meiner Familie, speziell meiner Mutter Gisela und meinem Vater Walter danken, die mich jederzeit unterstützt und mich liebevoll Zeit meines Lebens begleitet haben.
Schließlich möchte ich meiner großen Liebe Karin danken, die mein Leben mit Licht und Liebe erfüllt.

List of Publications

Jens Kühnle, Julian Shillcock, Ole G. Mouritsen and Matthias Weiss
A modeling approach to the self-assembly of the Golgi apparatus.
Biophysical Journal, **98**, 2839–2847 (2010)

Moritz Mercker, Mariya Ptashnyk, Jens Kühnle, Dirk Hartmann, Matthias Weiss and Willi Jäger
A multiscale and multidisciplinary approach to curvature modulated sorting in biological membranes.
submitted to: Journal of Theoretical Biology, (2011)